

ALMA MATER STUDIORUM · UNIVERSITÀ DI BOLOGNA

Scuola di Scienze
Corso di Laurea Magistrale in Fisica del Sistema Terra

Large scale drivers and historical analogs
of the 15 September 2022 Marche
heavy precipitation event

Relatore:
Dott. Salvatore Pascale

Presentata da:
Clara Naldesi

Correlatore:
Dott. Davide Faranda

Sessione II
Anno Accademico 2022/2023

Contents

1	Introduction	3
1.1	The 15 September 2022 Marche extreme precipitation event	3
1.2	Extreme precipitation events and Anthropogenic Climate Change	4
1.3	Attribution of extreme events to ACC	13
1.3.1	Thermodynamic vs dynamic contributions	13
1.3.2	Definition of <i>factual</i> and <i>counterfactual</i> climates	15
1.3.3	Different approaches for extreme event attribution	17
1.4	Overview of this thesis work	19
2	Data and methods	22
2.1	Data	22
2.1.1	Reanalysis	22
2.1.2	Additional precipitation’s datasets	25
2.2	The analogs methodology	26
2.2.1	General idea behind the method	26
2.2.2	Flow-conditioned probability of the event	27
2.2.3	An application of the analogs methodology: dynamical vs thermo- dynamical contribution to a HPE	28
2.2.4	Other applications of the analogs method	29
2.3	Description of the algorithm used to search analogs	32
3	Analysis of the 15th September 2022 Marche flooding event	34
3.1	Precipitation and major impacts	34
3.2	Representation of the precipitation event in ERA5 and observations	38
3.3	Large scale drivers of the 15 September Marche HPE	41
3.3.1	Synoptic-scale circulation	41
3.3.2	Atmospheric water vapour fluxes	43
3.3.3	Sea surface temperatures and thermodynamic environment	49
3.4	Planetary scale drivers	52

4	Analog-based analysis of the Marche high precipitation event	57
4.1	Preliminary tests and choice of the domain	57
4.2	Analogs of the 15 th September circulation pattern	59
4.3	Circulation analogs in the factual and counterfactual climates	62
4.4	Precipitation and thermodynamic environment	64
4.4.1	Precipitation	65
4.4.2	Precipitable Water and CAPE	67
4.5	Summary and results of the analog based analysis	70
5	Conclusions and final remarks	73

Abstract

On 15th September 2022, the Marche region in central Italy was affected by a heavy precipitation event that caused extensive flooding, 13 deaths and 2 billion in damage. The event was associated with a mesoscale convective system that stationed over the Marche region from early afternoon until the late evening of 15 September.

In this thesis work, we focus on the large scale atmospheric circulation that determined the event. We identify as the key drivers a low pressure over the Iberian Peninsula and a high pressure over the Ionian Sea that forced a southwesterly humid flow which triggered and sustained the precipitation event. Very high values of precipitable water (PW) (up to 50 Kg m⁻²) and convective available potential energy (CAPE) (up to 5500 J Kg⁻¹) in the Mediterranean area ensured a thermodynamic environment favourable to very intense convection over central Italy.

We then focus on determining whether and to what extent anthropogenic climate change (ACC) played a role in the occurrence of the event. By using the analogs method for extreme events attribution, we identify past circulation states during fall (September-November) similar to that of the event in a reanalysis dataset spanning the time period 1940-2022. We evaluate changes in variables associated with flow-analogs in the more recent period (1992-2022) relative to the early period (1944-1970). Our results suggest no significant trend in the frequency of occurrence of the large scale drivers of the event. The most significant changes are instead found in the thermodynamic environment over Italy during these circulations analogs: PW increases up to 6 Kg m⁻² and CAPE up to 1500 J Kg⁻¹ in the central Mediterranean. These results highlight the impact on atmospheric thermodynamic of anthropogenic global warming in increasing the potential for stronger convective events during similar synoptic conditions.

Abstract

Il 15 settembre 2022 la regione delle Marche nell'Italia centrale è stata colpita da un evento di precipitazione estrema che ha causato lo straripamento di diversi fiumi, 13 morti e 2 miliardi di danni. L'evento era associato ad un sistema convettivo alla mesoscala che ha stazionato sulle Marche dal primo pomeriggio fino alla tarda serata del 15 settembre.

In questo lavoro di tesi, ci concentriamo sull'analisi della circolazione atmosferica alla larga scala che ha determinato l'evento. Individuiamo nella bassa pressione sulla penisola Iberica e alta pressione sul Mare Ionio gli elementi chiave nel determinare i flussi umidi da sudovest che hanno innescato e sostenuto l'evento. Valori molto alti di precipitable water (PW) (fino a 50 Kg m^{-2}) e convective available potential energy (CAPE) (fino a 5500 J Kg^{-1}) nell'area mediterranea hanno assicurato un ambiente termodinamico favorevole a temporali molto intensi sull'Italia centrale.

Ci focalizziamo poi sul determinare il ruolo del cambiamento climatico antropogenico nel verificarsi dell'evento. Applicando la tecnica degli analoghi di circolazione atmosferica per l'attribuzione degli eventi estremi, identifichiamo gli stati di circolazione autunnali (settembre-novembre) simili a quello dell'evento nel periodo 1940-2022. I cambiamenti nelle variabili associate agli analoghi di circolazione vengono valutati nel clima recente (1992-2022) rispetto a quello passato (1944-1970). I nostri risultati indicano che non vi è nessun trend significativo nella frequenza con cui la circolazione alla larga scale associata all'evento si sia verificata. I cambiamenti più significativi invece si riscontrano nell'ambiente termodinamico sull'Italia durante gli analoghi di circolazione: la PW aumenta fino a 6 Kg m^{-2} e la CAPE fino a 1500 J Kg^{-1} sul Mediterraneo centrale. Questi risultati evidenziano l'impatto sulla termodinamica atmosferica del riscaldamento globale nel favorire eventi convettivi sempre più intensi durante condizioni sinottiche simili.

Chapter 1

Introduction

In this introductory chapter, we discuss the heavy precipitation event (HPE) that affected the Marche region on 15 September 2022, within the context of ACC. First, we briefly describe the HPE and the resulting impacts. We then emphasize the relationship between extreme events and Anthropogenic Climate Change (ACC), and finally we introduce the subfield of climate science dealing with the attribution of extreme events to ACC.

1.1 The 15 September 2022 Marche extreme precipitation event

On 15 September 2022, the Marche region in central Italy experienced an extraordinary HPE that caused the death of 13 people, dozens of injuries, and extensive damage. From early afternoon until midnight, a longitudinally elongated mesoscale convective system stationed over the region leading to very intense precipitation over the southern part of the Pesaro-Urbino province, and over most of the Ancona province. Fig. 1.1 shows the precipitation recorded by the regional rain gauge network accumulated between 1500 UTC to midnight. We see that most rain gauges measured values of accumulated rainfall between 70 and 150 mm, with few measuring more than 200 mm [3]. The highest value (425 mm) was measured in the mountain village of Cantiano (location in Fig. 1.2), where the extreme rainfall caused an extensive flooding of the village (Fig. 1.3b). Several rivers (Fig. 1.2) in the area swelled to above critical threshold and resulted in extensive flooding. In particular, the coastal town of Senigallia was one of those hit the hardest (Fig. 1.3a).

The Misa River flooded the city center and surrounding countryside. The damage to residential areas, agriculture, and industrial plants is estimated to be at least 2 billion euros [1].

This major event was followed by a second very intense and localised HPE on the 16th and precipitation over the entire Marche region on the 17th. This sequence of severe weather increased the vulnerability of the region and complicated rescue operations.

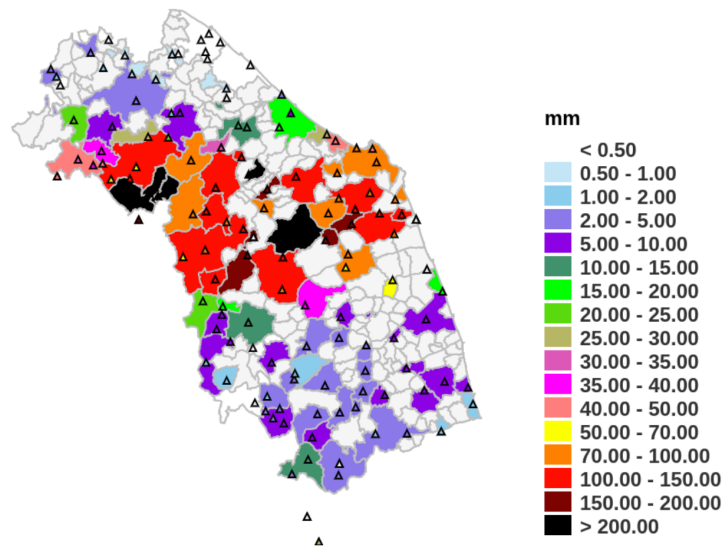


Figure 1.1: Accumulated precipitation from 1500 UTC to midnight on 15 September recorded by the regional rain gauge network. Colors refer to the maximum value in municipalities where at least one rain gauge is located. Figure from [3].

1.2 Extreme precipitation events and Anthropogenic Climate Change

The exceptional intensity of this event immediately raised the questions in the media: what is the role played by ACC in its occurrence? Would an event of this magnitude have been possible without the influence of ACC? Has ACC made it more likely to happen? These questions are challenging and do not admit straightforward answers. As described afterwards, the relationship between extreme events and ACC is one of the central aspects of the latest Intergovernmental Panel on Climate Change (IPCC) reports,



Figure 1.2: Copernicus Sentinel3 on the early morning of September 16 shows multiple sediment plumes poured into the Adriatic sea by the flood on previous day [38]. The rivers that originated them are (from north to south): Metauro, Cesano, Misa, Esino, Musone, Potenza. The location of the village of Cantiano is denoted by the red dot.



(a) Flooding in the area of Senigallia (Ancona) on September 16 [15] (b) Extreme rainfall in the village of Cantiano (Pesaro-Urbino) on September 15 [70]

Figure 1.3: Pictures of the damage produced by the HPE.

and the attribution of individual extreme weather and climate events to human-induced climate change is the subject of an entire relatively recent subfield of climate sciences. But how do we define an extreme event? According to the IPCC's definition of climate

extreme [41]:

The occurrence of a value of a weather or climate variable above (or below) a threshold value near the upper (or lower) ends of the range of observed values of the variable. By definition, the characteristics of what is called extreme weather may vary from place to place in an absolute sense. When a pattern of extreme weather persists for some time, such as a season, it may be classified as an extreme climate event, especially if it yields an average or total that is itself extreme (e.g., high temperature, drought, or heavy rainfall over a season). For simplicity, both extreme weather events and extreme climate events are referred to collectively as ‘climate extremes’.

The latest IPCC Synthesis Report (IPCC AR6 SYR) [40] states that in the decade 2011-2020 the mean global surface temperature has increased by 1.1°C relative to the 1850-1900 baseline period due to human-caused forcing (emissions of greenhouse gases (GHGs), aerosols, and land use). In particular, the relationship between extreme events and global warming is a central aspect of the report, which already specifies in the first pages ([40] section A.2):

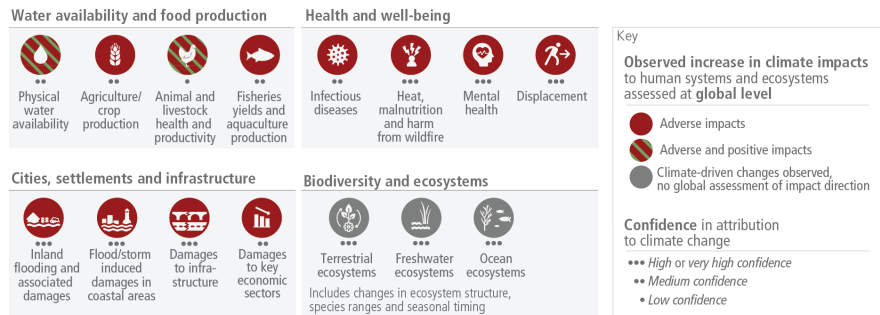
Human-caused climate change is already affecting many weather and climate extremes in every region across the globe. This has led to widespread adverse impacts and related losses and damages to nature and people (high confidence).

The idea that observed changes in extreme events (such as, for example, heatwaves, heavy precipitation, and droughts) can be attributed to ACC is becoming increasingly established: the report states that human influence has *likely* caused an increase in extreme precipitation, while it is *virtually certain* regarding the increase in heatwaves (Fig. 1.4b). Some recent hot extreme events would have been *extremely unlikely* to occur without human influence on the climate system ([75]). ACC is also considered *likely* to have increased the probability of compound extreme events ([40] section A.2.1), namely a combination of multiple drivers and/or hazards that contributes to societal and/or environmental risk [92]. In particular, the increase in compound flooding is attributed with *medium confidence* to human-caused climate change (Fig. 1.4b), while it is *likely* that human influence has increased the frequency of concurrent heatwaves and droughts ([40] section A.2.1).

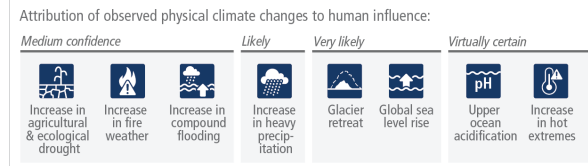
In general, an increased probability of HPEs is to be expected in a warmer atmosphere, since a warmer atmosphere can contain more water vapour. Specifically, as

Adverse impacts from human-caused climate change will continue to intensify

a) Observed widespread and substantial impacts and related losses and damages attributed to climate change



b) Impacts are driven by changes in multiple physical climate conditions, which are increasingly attributed to human influence



c) The extent to which current and future generations will experience a hotter and different world depends on choices now and in the near-term

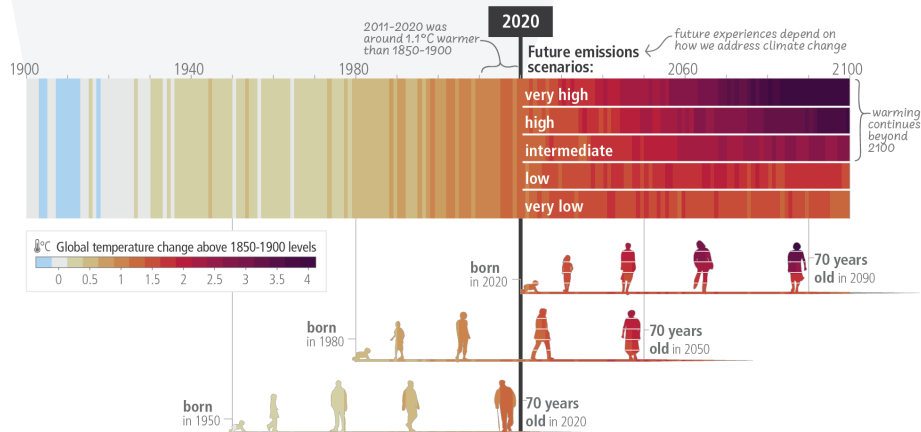


Figure 1.4: (a) Observed widespread impacts due to climate change and related losses and damages on human systems and natural ecosystems. (b) Physical climate changes connected impacts and their confidence level in the attribution to human influence. (c) Observed (1900–2020) and projected (2021–2100) changes in global surface temperature (relative to 1850–1900), which are linked to changes in climate conditions and impacts. Figure from IPCC AR6 Synthesis Report [40].

the temperature increases, the amount of water vapor in saturated air increases. The Clausius-Clapeyron equation relates the fractional change of saturation vapor pressure, and therefore the fractional change of the specific humidity at saturation, to the fractional change of temperature [31]:

$$\frac{\Delta q^*}{q^*} = \frac{\Delta e_s}{e_s} = \left(\frac{L}{R_v T} \right) \frac{\Delta T}{T} \quad (1.1)$$

where q^* is the specific humidity at saturation, e_s is the saturation vapor pressure above a liquid surface, L is the latent heat of vaporization, R_v is the gas constant for water vapor ($461 \text{ J K}^{-1} \text{ kg}^{-1}$) and T is the temperature. In the typical conditions of the lower troposphere, we have $T \sim 260 \text{ K}$ and $L/R_v T \approx 20$. Hence, a 1% change in temperature, which is about 3°K , is associated with about a 20% change in saturation specific humidity. In other words, the saturation specific humidity increases by about 7% for each 1°K increase in temperature. The solution of equation 1.1 at standard pressure is plotted in Fig. 1.5 and it clearly shows the exponential increase of saturation specific humidity with temperature.

An increase in HPE had already been indicated in the IPCC Sixth Assessment Report (AR6) [42], in which it is stated (section A.3):

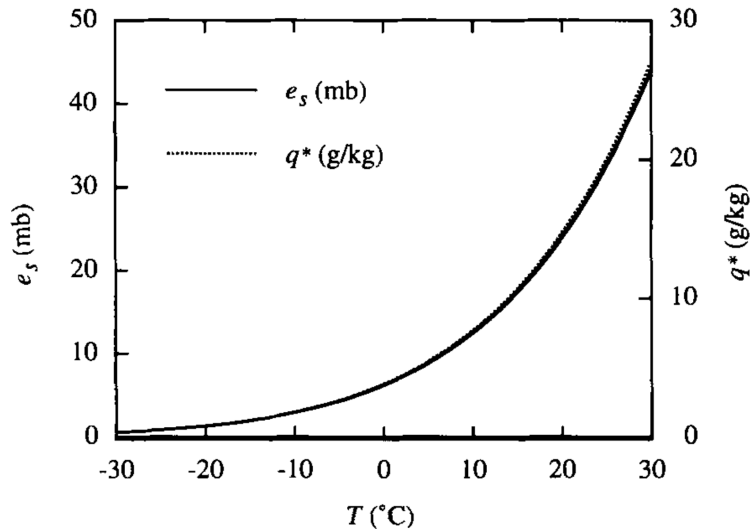


Figure 1.5: Saturation vapor pressure e_s and saturation specific humidity q^* as a function of temperature at standard pressure. Figure from [31].

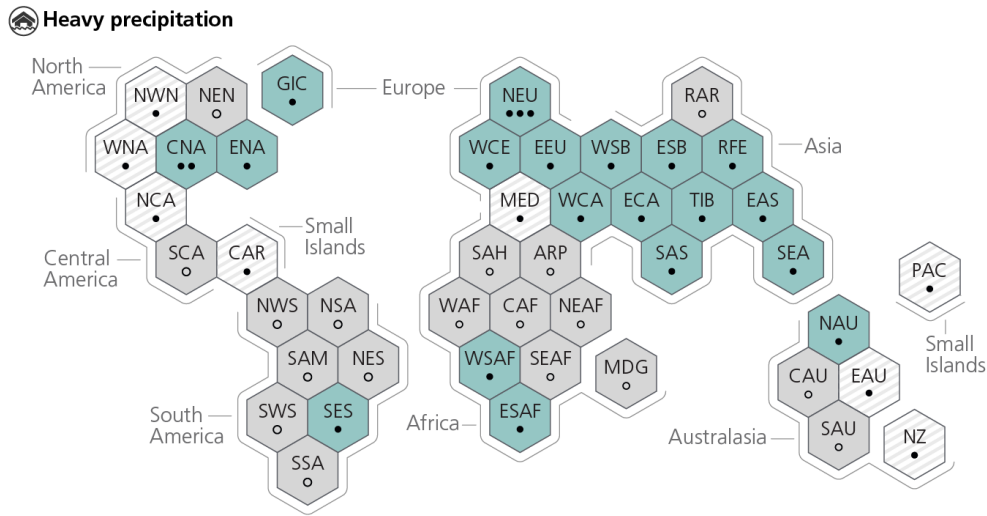


Figure 1.6: Synthesis of assessment of observed change in heavy precipitation and confidence in human contribution to the observed changes in the world's region.

Inhabited regions are displayed as hexagons with identical size in their approximate geographical location. The list of the regions to which the acronyms correspond can be found here. The colours on the hexagons represent the outcomes of the assessment on observed changes: turquoise stands for increase with at least medium confidence in the observed change, striped hexagons are used where there is low agreement in the type of change for the region as a whole, and grey hexagons are used when there is limited data and/or literature that prevents an assessment of the region as a whole. The confidence level for the human influence on these observed changes is based on event attribution literature, and it is indicated by the number of dots: three dots stand for *high* confidence, two for *medium*, one solid dot for *low due to limited agreement* and one empty dot for *low due to limited evidence*. Figure from the IPCC AR6 report [42].

the frequency and intensity of heavy precipitation events have increased since the 1950s over most land area for which observational data are sufficient for trend analysis (high confidence), and human-induced climate change is likely the main driver. Fig. 1.6 summarises regional observed changes in HPEs. Inhabited areas of the world are divided in 45 regions and in 19 of these an increase in HPEs is observed. In most of the remaining regions (18) data and literature are insufficient to establish a change, and only in 8 regions there is low agreement on the type of change. HPEs are already having serious societal consequences (Fig. 1.4a): they produce damage both inland and in coastal areas, they have a destructive impact on infrastructures and on economic sectors, for instance industry and agriculture. All extreme events pose a danger to nature and peo-

With every increment of global warming, regional changes in mean climate and extremes become more widespread and pronounced

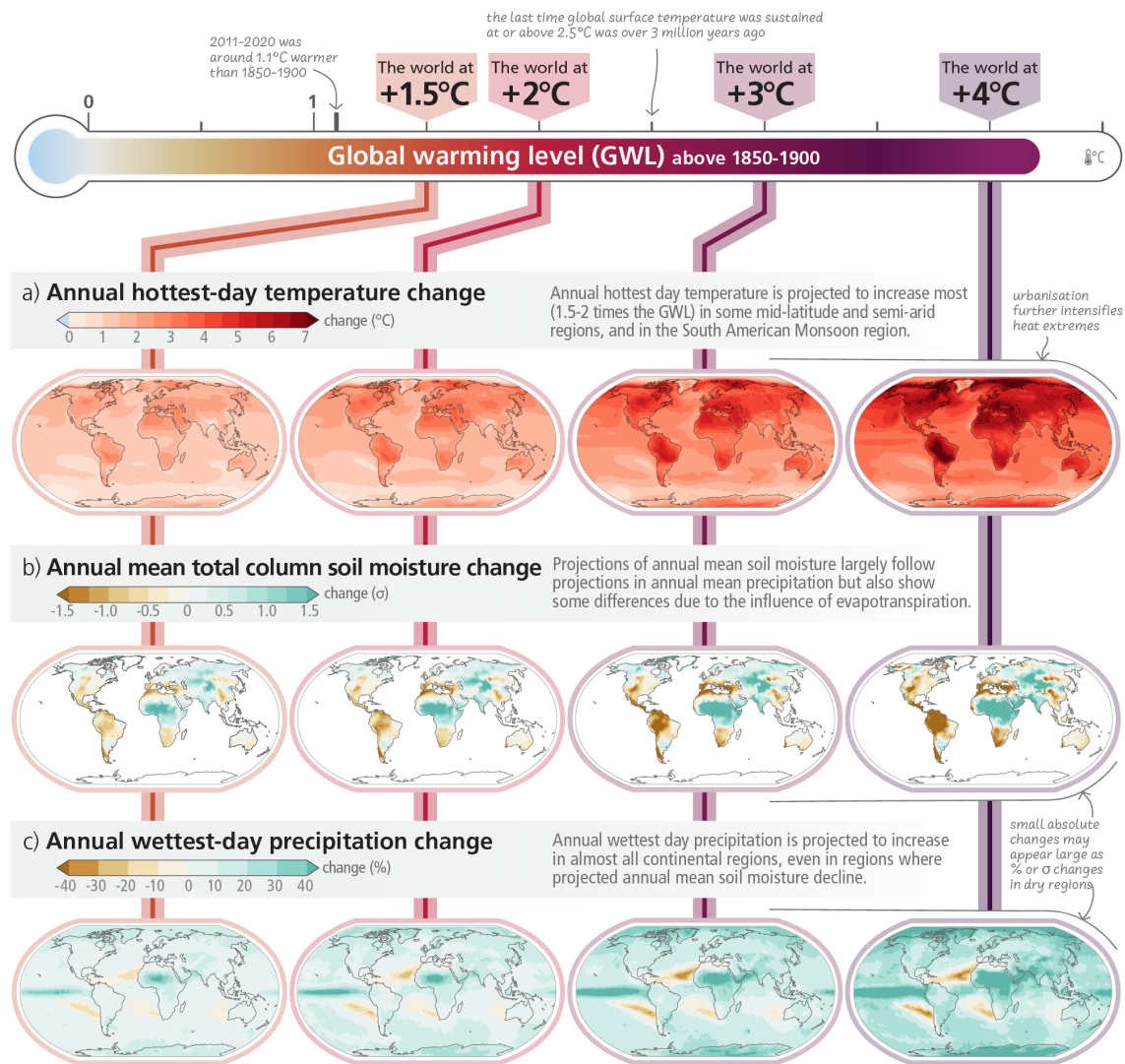


Figure 1.7: Projected changes of annual maximum daily maximum temperature (a), annual mean total column soil moisture (b) and annual maximum 1-day precipitation (c) at global warming levels of 1.5°C, 2°C, 3°C, and 4°C relative to 1850–1900. It is worth noting that heat extremes are exacerbated in urbanized regions and that **wettest-day precipitation is projected to increase over all continental areas**, even in regions where soil moisture is expected to decrease. Figure from IPCC AR6 Synthesis Report [40].

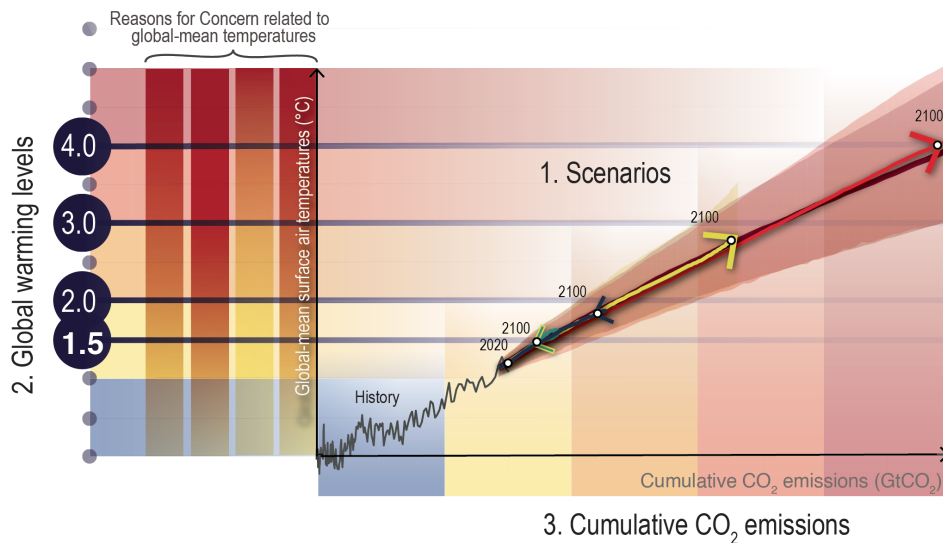


Figure 1.8: Relationship between (1) the five scenarios used in the IPCC AR6; (2) global mean warming levels relative to pre-industrial levels; (3) cumulative CO₂ emissions. White circles represent 2100 end-points for every scenario. Figure from IPCC AR6 ([8] Fig. 1.24).

ple in many ways (Fig. 1.4a): food and water security is endangered and less developed communities are disproportionately threatened. Human mortality due to extreme heat events, floods and storms has increased, especially in highly vulnerable regions where it was 15 times higher compared to regions with very low vulnerability. Impacts associated with extreme events result in even irreversible damages to biodiversity and are forcing displacement of affected communities all over the world. In urban areas hot extremes have intensified, leading to critical issues in water and energy management, and endangering the health of the most vulnerable people. In the coming decades, every additional increment of global warming will cause larger changes in extreme events (Fig. 1.7). For example, it is expected from climate projections with *high confidence* that further warming will make compound heatwaves and droughts more frequent, and that very wet and very dry weather will be further intensified ([40] par. B.1.3). Other projected regional changes include intensification of tropical cyclones and/or extratropical storms (*medium confidence*), and increases in aridity and fire weather ([40] par.B.1.4).

To explore future climate developments, we rely on future emission scenarios. An emission scenario (called *Shared Socioeconomic Pathways* in the latest IPCC report, [40])

is a description of how the future world may develop based on several socio-economic drivers, such as population growth, technological and societal development, and, most importantly, the way to produce energy. Thus, assuming a specific future political and socio-economic pathway, anthropogenic forcing (i.e., emissions of carbon dioxide, other GHG gases, aerosols and land use) can be consistently estimated for the future years. Since these political and societal choices are largely unpredictable (for example, no one would have predicted the rise of China as a world economic superpower in the Seventies), the IPCC AR6 uses not just one scenario but several different scenarios ([8] par. 1.6.1), defined by different levels anthropogenic radiative forcing, going from the most optimistic scenarios based on a sustainable future development (SSP1) to the most pessimistic scenarios based on fossil-fuel development (SSP5). Fig. 1.8 shows the relationship between five representative emissions scenarios used in the IPCC report, global warming and cumulative carbon emission. We see that they explore a wide range of plausible futures from potentially below 1.5°C best-estimate warming to over 4°C warming by 2100.

It is worth noting that the IPCC AR6 (Executive Summary of Chapter 11, [75]) states that even relatively small incremental temperature increases (+0.5°C) cause statistically significant changes in extremes on the global scale and for large regions (high confidence). This also applies to the intensification of heavy precipitation (high confidence). As a consequence, the frequency and magnitude of pluvial flooding (due to exceeding drainage capacity) are projected to increase (high-confidence). In particular, in the scenario of a global warming level of 4°C with respect to pre-industrial level, very rare HPEs would become more frequent and more intense at a global scale ([75]). The intensification will follow, globally speaking, the Clausius-Clapeyron relation discussed before (increase of 7% in the amount of water vapor in saturated air per 1°C of global warming), although regional departures are possible due to water availability and changes of the atmospheric dynamics . The increase in the frequency will be non-linear and will be higher for rarer events. As an example, the frequencies of 10-years and 50-years events will *likely* double and triple, respectively. Projected changes in HPEs show important regional differences that depend on the regional warming level, changes in atmospheric circulation and storm dynamics (par. 11.4.5 of ref. [75]).

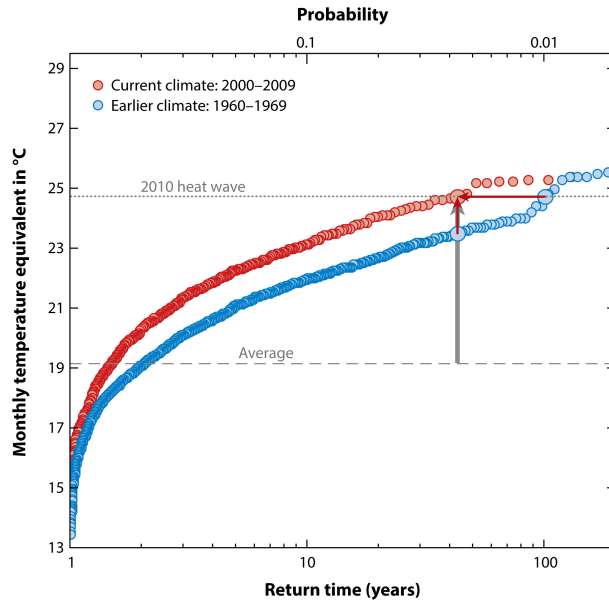
1.3 Attribution of extreme events to ACC

Due to the significant societal impacts of weather and climatic extreme events, there is great interest, both scientifically and from the general public, in understanding the role of ACC in single extreme events. The science of extreme event attribution deals exactly with this scientific question: the ultimate objective for the science of event attribution is to estimate how much ACC has affected the magnitude or probability of occurrence of an individual event.

Within the last 20 years, the attribution of extreme weather events to ACC has gone from being considered impossible to becoming a blooming and very active field of climate sciences. Comprehensive and detailed reviews on this topic is provided, for example, by the *Attribution of Extreme Weather Events in the context of Climate Change* report [60] or by Otto (2017) [64]. The first attribution study was performed by Stott *et al.* [81] on the European heatwave of the summer 2003, that caused the death of more than twenty-thousand people [55]. The authors estimate that it is *very likely* (confidence level $>90\%$) that human activities have at least doubled the probability of occurrence of a heatwave of the same magnitude. Other seminal studies were those focusing on the 2010 Russian summer heatwave, which dramatically increased the mortality rate in the country [56]. In fact, for this event, two apparently contradictory results were found by two distinct attribution studies: one study found that the change in the intensity due to ACC was small with respect to natural variability [18], while the second study analyzed human influence of the frequency of an event of that magnitude and found that ACC had increased it of five times with respect to pre-industrial times [69]. These two works focused on complementary aspects, the intensity and the frequency of the event (Fig. 1.9), and have raised awareness of the importance of clearly defining events and framing the attribution question [62].

1.3.1 Thermodynamic vs dynamic contributions

In general, ACC has an impact on both the atmospheric thermodynamics, i.e., on the thermal structure of the atmosphere and associated moisture distribution, and the dynamics, i.e., on the prevailing winds and general circulation of the atmosphere [33, 74]. Since both are expected to change in response to ACC, climatic extremes will be shaped



 Otto FEL, 2017.
Annu. Rev. Environ. Resour. 42:627-46

Figure 1.9: Return time of extremely high monthly mean temperatures in Western Russia in the current climate (red) and an earlier climate (blue). The monthly average temperatures are represented by a dashed line, while the magnitude of the 2010 heat wave is depicted by a dotted line. The gray arrow illustrates the deviation from the average magnitude, and the red vertical arrow represents the impact of ACC on this deviation. The red horizontal arrow signifies the increased frequency of heat waves resembling the one in 2010, attributed to human-induced climate change. Figure from Otto [64].

by both a thermodynamic and dynamic contribution. Regarding precipitation extremes, which is the focus of this thesis work, a general increase in the probability of having extreme rainfall in a warmer atmosphere is expected from the thermodynamic contribution (see discussion on the Clausius-Clapeyron equation in Section 1.2). However, while the thermodynamic contribution is robust and well understood, several other physical factors - like dynamical and microphysical contributions - govern the response of precipitation extremes, for which we still do not have a sound theoretical understanding. Furthermore, climate models, that provide a fundamental tool for the characterization of projected changes in precipitation extremes, are not expected to be reliable for precipitation extremes because of their biases in the representation of convective precipitation [61].

Thermodynamic vs dynamic factors play a key role also in setting up a specific, single

extreme precipitation event. In fact, every extreme precipitation event is the result of the non-trivial interaction between the atmospheric dynamics and thermodynamic contributions. For instance, both the large-scale flow conditions and the atmospheric capacity to hold water are crucial factors in the occurrence of a HPE. In the context of attribution, it is often useful to assess the influence of ACC on the two driving processes separately, although the level of confidence that we have in the two contributing drivers varies significantly: while the ACC thermodynamic signal is robust in observations and climate models and well understood theoretically, ACC impacts on the atmospheric circulations are less clearly understood and more difficult to be simulated by climate models, which often show contrasting responses [76], [83]. This is also reflected in the impacts on extreme events: the influence of ACC on the thermodynamic component was shown to have altered the frequency and intensity of several extreme events, while it is more challenging to assess how shifts in circulation due to ACC impact extreme events [87]. Projected changes in regional atmospheric circulation determine the local character of ACC impacts on extreme events (IPCC AR6 report ref. [42]). A better understanding of the dynamic component is therefore crucial for extreme events attribution.

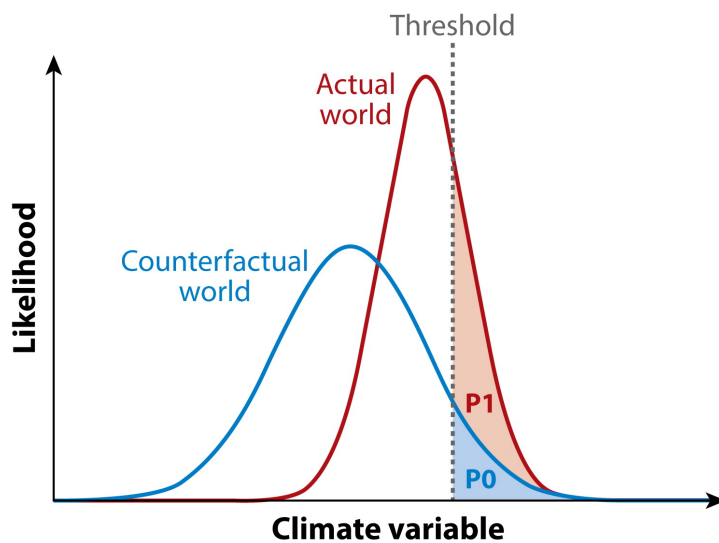
1.3.2 Definition of *factual* and *counterfactual* climates

In attribution science, there are a range of different methodologies and conceptual approaches that can lead to very different assessments and can generate confusion in the public. For this reason, it is critical to clearly frame and communicate:

1. The **definition of the event**. There is no *a priori* scientifically correct or incorrect definition of the event. The choice of the definition is determined by a combination of factors changing on a case-by-case basis: the impacts of the event, the availability of reliable meteorological data, who is asking the attribution question... It is important to keep in mind that the definition of the event determines itself the outcome of the attribution analysis and so its choice must be made carefully.
2. The **attribution question**. The usual question asked by the public and the media after the occurrence of an extreme event is: *Was that event caused by climate change?* This is an ill-posed question though, since ACC does not cause any single event in a deterministic sense, but it can rather make some of them more likely

to occur or more intense when they do. Therefore, the attribution question needs to be rephrased more carefully (e.g., chapter 2 of ref. [60]). Examples of possible rephrasing of this question are: *has a specific extreme event become more or less likely because of ACC? To what extent has ACC impacted its magnitude? Would it have been possible without human influence?* It is important to notice that distinct framing of the attribution question lead to the choice of different methodologies. Two approaches applied to the same extreme event can bring seemingly contradictory results precisely because different approaches answer different questions. For example, it is different to focus on the role of ACC on the frequency or intensity of an event. The first event that highlighted the importance of this difference was the 2010 heatwave in Russia, as we discussed earlier.

3. The definition of the **counterfactual climate**. In attribution science it is necessary to analyze extreme weather events as they would have been in a climate without ACC, the so-called *counterfactual climate*, and compare them with those which have occurred in the present climate, i.e., the so-called *factual climate*. As no observations or experience of counterfactual climates are available, the counterfactual climate must be either simulated through climate models or approximated by the climate of historical periods in which the anthropogenic forcing can be considered small ([64]). This last is definitely the case when dealing with observations: a historical period in which anthropogenic forcing is considered to be small is taken to be representative of the counterfactual climate, even though this is not strictly true. The timing of this historical period has necessarily to be the result of a compromise between the need to minimize anthropogenic influence and the availability of observational data. In model-based approaches, the counterfactual climate is usually simulated removing the anthropogenic forcing. Hauser *et al.* (2017) [32] summarizes the three ways to define the counterfactual climate more commonly found in the literature: (a) model simulations driven by natural forcing only, that is by observed solar and volcanic boundary conditions, and pre-industrial (i.e., around year 1850) levels of GHGs and aerosols; (b) model simulations run with pre-industrial levels of GHGs and aerosols, but excluding historical natural forcing variations; (c) model simulation forced with historical boundary conditions (anthropogenic GHGs and aerosols) for years during which this forcing is relatively



AR Otto FEL. 2017.
Annu. Rev. Environ. Resour. 42:627–46

Figure 1.10: In the risk-based approach, the probability distribution of a generic climatic variable (e.g., daily precipitation) is simulated in the factual (red line) and counterfactual (blue line) climates. The extreme event is defined through a threshold and the associated probability of occurrence (red and blue shading) is assessed and compared in the two cases. Figure from Otto [64].

small (for example, late 19th or early 20th century). This is an approach generally adopted whenever (a) and (b) are not available. It is important to notice that the choice of methodology to simulate the counterfactual, as well as the model used and the boundary conditions imposed, critically impact the outcome of the attribution study, and a multi-model and multi-method analysis would be crucial for a solid attribution [32].

1.3.3 Different approaches for extreme event attribution

Event attribution studies use a variety of different methods and approaches. These approaches highlight different characteristics of the event and are somewhat complementary. Here we briefly discuss them:

- **The risk-based approach.** In the risk-based approach, the aim is to quantify the change in the probability of occurrence of an extreme event due to ACC. The event

is defined through a threshold. There is no a priori definition of such threshold, and different definition are possible ([75]). As an example, we can use two different definitions for the threshold that defines hot days: (a) a relative threshold, identified with the 90th or higher percentile of maximum daily temperature over a reference period; or (b) an absolute threshold, e.g., 35°C, because temperatures above this threshold are usually associated with health problems. As we can see in Fig. 1.10, the extreme event frequency in the factual (P_1) and counterfactual (P_0) climates are compared and it is assessed if their difference is statistically significant. A common way to compare P_1 and P_0 is through the risk ratio (RR), defined as:

$$RR = \frac{P_1}{P_0} \quad (1.2)$$

which quantifies how many times the event has become more or less likely in the factual climate. If $RR > 1$, the event is more probable in the factual world and the increase in probability is attributed to ACC.

It is important to stress that this method is generally applied to both observations and model simulations. When observation are used, P_0 and P_1 are obtained by fitting a probability distribution (e.g., Gaussian or Generalized Value Distribution, see ref. [63]) to observation data. In practice, however, historical observations are often available time periods (e.g., few decades) which are too short to accurately fit the tails of distributions or extreme value distributions, thus not enabling a reliable statistical evaluation of whether there has been a significant change in event frequency or intensity. To overcome this limitations, climate model simulations are used to define the factual and counterfactual climate. This approach has been employed to several extreme events, including heat waves [81, 67], heavy precipitation events [84] and droughts [63, 65, 66]. Given the model data, probability distributions are either fitted to data or empirically reconstructed, especially when a large number of points are available [85].

- **The Boulder approach.** This methodology was developed by scientists at the National Oceanic and Atmospheric Administration (NOAA) in Boulder, Colorado (see ref. [64] for a review on applications). The Boulder approach aims to assess the predictability of a single extreme event from large-scale circulation patterns.

The focus is not on the simulation of the event statistics and so the question “what is the likelihood of the event and how will it change” is not answered. Rather, this methodology seeks to disentangle different causal factors related to large-scale circulation leading to the event (Fig. 1.11), like SSTs, atmospheric forcing and internal atmospheric variability.

- **The circulation analogs approach.** The methodology was developed by scientists at the Laboratoire des Sciences du Climat et de l’Environnement in France (e.g., refs. [6, 89]). The focus of this approach is the dynamics associated with the extreme event. The event is defined by its circulation state and similar atmospheric circulations, namely the analogs, are searched in reanalysis data or model simulations [64]. Since this the methodology which will be applied in the present study, we will not go into the details of the methods as this will be the subject of Section 2.2. Let us just say that this technique allows us to assess if the circulation that characterized an extreme event has become more frequent in recent times, or if its seasonality has changed.

Furthermore, the analogs methodology enables us to take into account the dynamic process leading to the extreme event, which is not possible in analyses based on extreme value theory. On the other hand, it is worth noting that within the analogs approach the likelihood of the extreme event is not estimated and it is not the focus of the technique, as it is in the risk-based methodology. A combination of these two methodologies helps to quantify the thermodynamic and dynamic effects (Section 1.3.1) in the overall change in the likelihood of an event [87]. Disentangling these two effects is one of the main challenges of attribution science and this demonstrate that there is great value in analyzing the same event using different methodologies.

1.4 Overview of this thesis work

The present thesis work has two key objectives. First, to analyze the evolution of the HPE that affected the Marche region on 15 September 2022, identifying the synoptic drivers and the key meteorological processes that initiated and maintained it. Second,

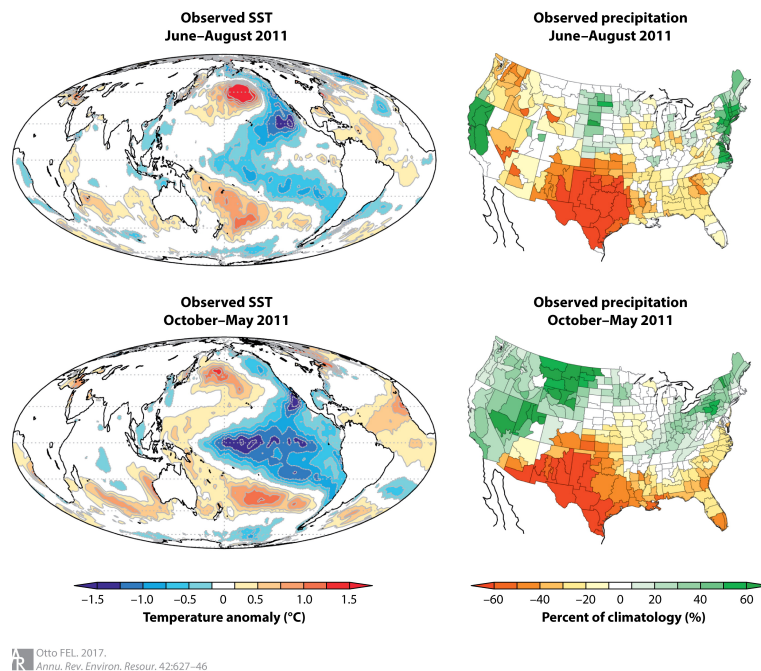


Figure 1.11: The boulder approach emphasises the role played by large-scale circulation patterns in the occurrence of the extreme event. This figure shows the case of the Texas heat wave of the summer of 2011. SST and precipitation anomalies are evaluated during the event (top) and in previous months (bottom) in order to assess their influence on extreme summertime heat. Figure from Otto [64].

to identify the impact of ACC on similar large scale conditions and thus on HPE over Central Italy. To achieve that, the method of circulation analogs is applied to reanalyses to analyze similar atmospheric circulation states to that of the event in a present and mid-twenty century climates. As an important caveat to this study, it is important emphasizing that the focus here are HPEs and circulation analogs associated with HPEs over the northern part of Central Italy rather than the specific event happened in the Marche region, since the spatial resolution of the reanalyses and its intrinsic limitations in simulating convective precipitation do not allow us to realistically capture the details of the event. Overall, this study is an important first step toward an attribution study of the event under consideration, as it investigates the relationship between large scale drivers and HPEs.

The thesis is organized as follows: Chapter 2 provides a description of the dataset and of the circulation analog method for extreme event attribution; in Chapter 3, the

dynamics of the Marche HPE is presented and a detailed study of the large-scale drivers is carried out; Chapter 4 is dedicated to an examination of circulation analogues and associated meteorological variables of interest in the factual and counterfactual climates; conclusions and an overview of the main findings of the study are given in Chapter 5.

Chapter 2

Data and methods

In this chapter, we describe the observations and reanalyses data used to study the Marche HPE. Then, a detailed overview of the analogs methodology is presented. In the following (Chapter 4), we will use this approach to compare similar circulation conditions as those that led to the Marche HPE and identify the effect of ACC on those. Finally, we provide a description of the software employed to implement the analogs search to our case study.

2.1 Data

2.1.1 Reanalysis

In the present study we use the ERA5 reanalysis database. Retrospective analyses (or reanalyses) merge observations unevenly distributed in space and time and models, with the background model forecast to provide global four-dimensional and uniform gridded atmospheric and climatic data associated with many dynamical and physical processes [47] at very high time resolution (e.g., hourly). ERA5 is the latest European Centre for Medium-Range Weather Forecasts (ECMWF) atmospheric reanalysis of the global climate and it is produced by the Copernicus Climate Change Service (C3S) at ECMWF [21]. ERA5 is the fifth generation of atmospheric reanalysis produced by ECMWF, and it presents significant improvements if compared to previous versions of the ECMWF reanalyses [35]. One important improvement of ERA5 is its enhanced temporal and spatial resolutions (hourly output, 31km horizontal resolution, 137 vertical levels from

Variable	Units	Description
Total precipitation	m	The total amount of liquid and frozen water that precipitates on the Earth's surface. The accumulation period is 1 hour.
Mean sea level pressure	Pa	Atmospheric pressure at the Earth's surface, adjusted to the height of mean sea level.
Vertical integral of eastward water vapour flux (IWVF _x)	kg m ⁻¹ s ⁻¹	Horizontal rate of flow of water vapour mass in the eastward direction: $IWVF_x = \int_0^{TOA} qu \rho dz$ where q is the specific humidity, u the zonal wind, ρ the air density and TOA the Top of the Atmosphere.
Vertical integral of northward water vapour flux (IWVF _y)	kg m ⁻¹ s ⁻¹	Horizontal rate of flow of water vapour mass in the northward direction: $IWVF_y = \int_0^{TOA} qv \rho dz$ where q is the specific humidity, v the meridional wind, ρ the air density and TOA the Top of the Atmosphere..
10m u-component of wind	m s ⁻¹	Eastward (zonal) component of the 10m wind.
10m v-component of wind	m s ⁻¹	Northward (meridional) component of the 10m wind.
Sea surface temperature (SST)	K	Temperature of sea water at the surface.
Total column water, also called precipitable water (PW)	kg m ⁻²	Vertical mass integral of water vapour, liquid water, cloud ice, rain and snow in an air column from the Earth's surface to the TOA.
Convective available potential energy (CAPE)	J kg ⁻¹	Potential energy given by the total excess buoyancy: $CAPE = \int_{LFC}^{EL} \frac{F}{\rho'} dz$ where F is the upward buoyancy force per unit volume on the rising air parcel due to the temperature difference between the parcel and the surrounding environment, ρ' is the air parcel density, LFC is the level of free convection and EL the equilibrium level [53]. CAPE defines the theoretical maximum velocity that a positively buoyant air parcel could acquire through adiabatic ascent.

Table 2.1: ERA5 2D surface variables used in the thesis work [13].

Variable	Units	Levels [hPa]	Description
Geopotential	$\text{m}^2 \text{s}^{-2}$	500, 300	Gravitational potential per unit mass relative to sea level at a specific location: $\Phi(z) = \int_0^z g dz'$
Geopotential height	m	500, 300	Geopotential divided by gravitational acceleration at the Earth's surface g_0 : $Z = \frac{\Phi(z)}{g_0}$
Divergence	s^{-1}	950	Horizontal divergence of velocity: $\nabla \cdot \mathbf{V} = \frac{\partial u}{\partial x} + \frac{\partial v}{\partial y}$
Specific humidity	kg kg^{-1}	1000-300	Mass of water vapour m_v in a unit mass of air (dry air m_d plus water vapour m_v): $q = \frac{m_v}{m_v + m_d}$
U-component of wind	m s^{-1}	1000-300	Eastward component of the wind (u).
V-component of wind	m s^{-1}	1000-300	Northward component of the wind (v).
Moisture flux	m s^{-1}	1000-300	Rate of transfer of water vapour, obtained combining specific humidity and u and v components of wind: $\text{WVF}_x = qu$, $\text{WVF}_y = qv$

Table 2.2: ERA5 3D variables on pressure levels used in the thesis work [12].

the surface of the Earth up to a height of 80km). ERA5 provides an expanded range of atmospheric and climatic variable and benefits from 10 years of model development since the prior reanalysis ERA-Interim. From March 2023, the period cover was expanded from 1940 to the present [34], thus providing more than eighty years of data. The ERA5 reanalysis products are accessible to the general public and can be freely downloaded via the Climate Data Store [20]. Data are provided on a regular latitude-longitude grid with a 0.25° resolution on 37 pressure levels, in NetCDF files. Besides the hourly means, data are available at the daily and monthly scale too.

Tab. 2.1 and Tab. 2.2 provide a summary of the ERA5 variables we use in this thesis work, divided between 2D surface parameters and 3D height-dependent variables. Specifically, we use total precipitation accumulated over 24 hours on the day of the event to characterize its intensity. The use of the precipitation field from reanalyses comes with a big caveat, though. In fact precipitation is not directly assimilated into ERA5 (as in all other reanalyses products), but is generated by the atmospheric model of the ECMWF’s Integrated Forecast System. Even if reanalyses precipitation data have undergone through a considerable improvement in the latest developments, relevant biases and errors still remain[4]. As such, precipitation as well as other variables relating to the hydrological cycle should be used with caution. We use hourly mean sea level pressure (SLP) and 500 hPa geopotential height (Z500) maps to study the evolution of the atmospheric circulation associated with the event. We exploit the availability of variables like the vertically integrated water vapour flux (IWVF), the moisture flux as a function of height, the precipitable water (PW) and the convective available potential energy (CAPE) to analyze the evolution of atmospheric water vapour fluxes and the thermodynamic atmospheric background before and during the Marche HPE. Surface divergence and 10m wind fields are used to explore the initiation and maintenance of the mesoscale convective system. We examine daily mean sea surface temperature (SST) to assess to what extent higher-than-normal SSTs in the western Mediterranean Sea favoured the HPE. Finally, we use 300 hPa geopotential height (Z300) and the zonal and meridional wind components at 300 hPa to identify the drivers of the HPE at the planetary scale.

2.1.2 Additional precipitation’s datasets

Because of the limitations of reanalyses in representing the precipitation field realistically, we employ two additional precipitation datasets to characterize the Marche HPE, that is either direct *in situ* measurements or estimates retrieved from satellite observations. Specifically, we have:

1. The regional rain gauge network of the Marche region. As the dataset is not publicly available, we use the maps elaborated by the Civil Protection Department of the Marche region and published in the event report [3].

2. The IMERG product managed by NASA [39], that estimates precipitation combining information from the GPM satellite constellation and provides observational data at high spatial and temporal resolution (10 km/0.1° and 30 minutes).

Three data versions exist: Early, Late and Final run. The Final run is the one recommended for research because it includes also rain gauge data, but unfortunately it was not available for September 2022 at the moment of this work and so the Late run (available at [59]) is used for this research.

2.2 The analogs methodology

2.2.1 General idea behind the method

The analogs methodology is an attribution approach focused on atmospheric circulation designed by scientists at the Laboratoire des Sciences du Climat et de l’Environnement [90, 89, 6, 86, 45]. With this approach, we search for historical atmospheric circulation patterns very “similar” to the synoptic situation of a given extreme event. We call these atmospheric states circulation analogs or simply “analogs”. The analogs methodology allows us to evaluate the probability of occurrence of an extreme event *conditioned* to a specific circulation state, i.e., the flow-conditioned probability. The analog methodology also allows us to determine how meteorologically similar events have changed (for example, due to the thermodynamic effects of climate change) and whether the frequency of such circulation states has changed through time. In general, this approach provides insights on the dynamical factors leading to an event. As discussed in chapter 1.3, we have a lower degree of understanding about how ACC is altering the dynamical drivers of extreme events as compared to the thermodynamical ones [61].

The analogs methodology has been applied to investigate the ACC influence on the dynamics of several extreme events. The methodology was designed and first applied by Yiou *et al.* (2007) [90]. The authors applied it to the case of the exceptionally warm 2006/2007 fall and winter and found that although the circulation state was favorable to the occurrence of the event, it was not the main driver. The temperatures that characterized the event were significantly bigger than those associated with flow analogs. The authors identify therefore the thermodynamic component as the main factor explaining warming. The methodology was later used by Vautard and Yiou (2009) [86] to explore

the relationship between atmospheric circulation and recent changes in the European surface climate. They found that over the past six decades, changes in atmospheric circulation have been the primary factors influencing surface weather trends in winter. In summer, however, temperature had a significant impact on the water cycle, and dynamics became a secondary factor.

2.2.2 Flow-conditioned probability of the event

A more detailed description of the method is now provided. Let y be the meteorological variable characterizing the event. As an example, y can be near-surface temperature in the case of a heatwave or precipitation in the case of a HPE. The extreme event then occurs when y *overcomes a threshold* y_0 . The atmospheric flow F_e associated with the event can be represented by any dynamical variable which is significant for the definition of the synoptic circulation leading to the event. For example, F may be defined in terms of SLP or Z500 patterns over the domain associated with the event. The probability to have an extreme event conditioned to the specific circulation F_e is assessed selecting a set of K circulation states F_k ($k = 1, 2, \dots, K$) similar to F_e , the so-called analogs. An objective way to select the K most similar analogs to F_e , extensively used in scientific literature, is to look for circulation states F_k that minimize the Euclidean distance d_E from $F_e(x)$:

$$d_E(t) = \sum_{x \in \text{domain}} |F(x, t) - F_e(x, t_e)| \quad (2.1)$$

where $F_e(x, t_e)$ is the event circulation state occurred at time t_e , and x the space variable (e.g., longitude, latitude) belonging to the chosen spatial domain. After calculating $d_E(t)$ for all time t of the dataset, we obtain a time series of distances $d_E(t)$ from which we select the first K smallest circulation states.

We can then express the flow-conditioned probability as

$$P(y > y_0 | F) = \frac{K_a}{K} \quad (2.2)$$

where K is the number of the closest analogs to F , and K_a is the number of analogs for which the threshold y_0 is exceeded [87]. It is worth noting that there is no a priori right choice of the search domain and the identifying variable of F . These choices, however,

define the features searched for in the analogs selection and therefore critically affect the set of analogs identified.

2.2.3 An application of the analogs methodology: dynamical vs thermodynamical contribution to a HPE

Vautard *et al.* (2016) [87] develop a methodology based on flow-conditioned probabilities that allows for a separate attribution of ACC dynamic and thermodynamic impacts on extreme events. To do so, they simulate two ensembles of N_f factual and N_c counterfactual flows and compare the flow-conditioned probability in the two worlds. The probability of exceedance in the two worlds is defined as the average of the individual flow-conditioned probability associated with flows in the two ensembles:

$$P_f(y > y_0) = \frac{1}{N_f} \sum_{n=1}^{N_f} P_f(y > y_0 | F_{f,n}) \quad (2.3)$$

$$P_c(y > y_0) = \frac{1}{N_c} \sum_{n=1}^{N_c} P_c(y > y_0 | F_{c,n}) \quad (2.4)$$

where $F_{f,n}$ and $F_{c,n}$ are the individual circulation analogs composing the two sets.

To estimate dynamical changes, we subtract from equation 2.3 the exceedance probability obtained using counterfactual flows and looking for their analogs in the factual world:

$$P_{dyn}(y > x_0) = \frac{1}{N_f} \sum_{n=1}^{N_f} P_f(y > y_0 | F_{f,n}) - \frac{1}{N_c} \sum_{n=1}^{N_c} P_f(y > y_0 | F_{c,n}) \quad (2.5)$$

The thermodynamical contribution is isolated subtracting from equation 2.3 the exceedance probability obtained using factual flows and looking for their analogs in the counterfactual climate:

$$P_{therm}(y > y_0) = \frac{1}{N_f} \sum_{n=1}^{N_f} P_f(y > y_0 | F_{f,n}) - \frac{1}{N_f} \sum_{n=1}^{N_f} P_c(y > y_0 | F_{f,n}) \quad (2.6)$$

Vautard *et al.* apply this methodology to the extreme January 2014 precipitation event in Southern UK. The event caused flooding and storm surges in southern England and Wales, and £451 million in damage [73]. They define the circulation state F as January

monthly mean SLP maps over NE Atlantic and Europe and assess percentage dynamical and thermodynamical contribution through equations 2.5 and 2.6:

$$100 \cdot \frac{P_{dyn}(y > y_0)}{P_f(y > y_0) - P_c(y > y_0)} \quad (2.7)$$

$$100 \cdot \frac{P_{therm}(y > y_0)}{P_f(y > y_0) - P_c(y > y_0)} \quad (2.8)$$

Fig. 2.1 shows the overall change in the probability of extreme precipitation in the factual world with respect to the counterfactual as a function of the precipitation amount threshold x_0 , highlighting the two percentage contributions. The four panels of Fig. 2.1 show the sensitivity of the results to the number of analogs and the definition of distance used to detect the analogs. We see that methodological changes have little impact on the average results. In all cases in Fig. 2.1, shifts in large-scale flows account for 20% - 50% of the overall probability change, and the dynamic contribution decreases as the threshold increases. As specified by the authors, this approach can also be applied to observations or reanalysis data, searching for factual and counterfactual analogs in recent and past time intervals. In this case, it is important to verify if the difference between factual and counterfactual can be explained by long-term natural variability.

2.2.4 Other applications of the analogs method

The analogs methodology has been used to investigate different types of extreme events. In the following we will briefly review a few outstanding examples. Cattiaux *et al.* (2010) [6] apply it to the cold temperatures recorded in Europe during winter 2009-2010. The winter of 2009-2010 was associated with a persistent negative phase of the North-Atlantic Oscillation, causing extreme cold temperature anomalies over northwestern Europe. Although the associated dynamics was one of the most favorable to cold weather since the 1820s, the authors show that the event was not extreme with respect to the past sixty years. Moreover, temperatures associated with past flow-analogs were significantly lower than those of winter 2010 (Fig. 2.2). We can consider the event as an example of a cold extreme mitigated by climate-warming (see the linear trend in Fig. 2.2(d)). Vautard *et al.* (2016) [87] exploit the analogs methodology to show that the extreme precipitation totals observed in January 2014 in Southern UK can be attributed for one

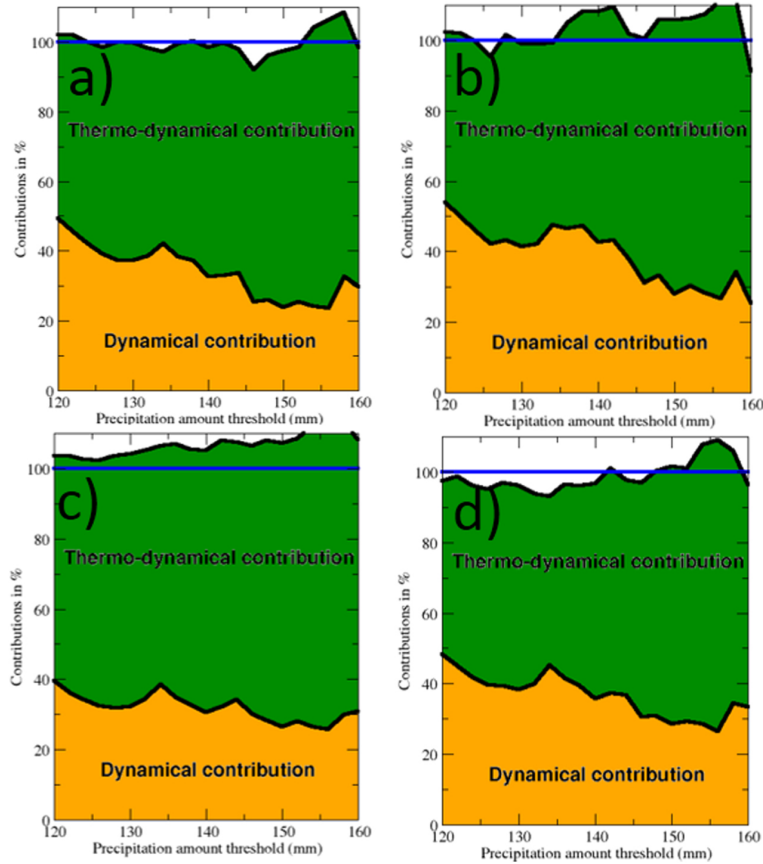


Figure 2.1: Attribution of the thermodynamic and dynamic components for the extreme precipitation January 2014 in Southern UK. The difference between factual and counterfactual overall probability of extreme precipitation is represented as a function of the precipitation threshold used to define the extreme event. Dynamic and thermodynamic components are expressed as a percentage of the total probability change. The number of best analogs used to compute flow-conditioned probabilities is: 50 in (a) and (d); 10 in (b); 500 in (c). The Euclidean distance is used in (a), (b), and (c) to identify the best analogs. In (d) the distance is weighted by the square of the pointwise correlation between the monthly precipitation and the SLP. Figure from Vautard *et al.* (2016) [87].

third to changes in weather circulation patterns and two third to thermodynamic changes (see also Section 2.2.3). Yiou *et al.* (2017) [89] focus again on the record precipitation event of January 2014 in Southern UK and develop a statistical methodology to quantify the dynamical and thermodynamical contribution. They compare two possibilities for the creation of the factual and counterfactual climates: using model simulations, and recent and old periods from reanalysis-data. Jézéquel *et al.* (2018) [45] focus on ACC

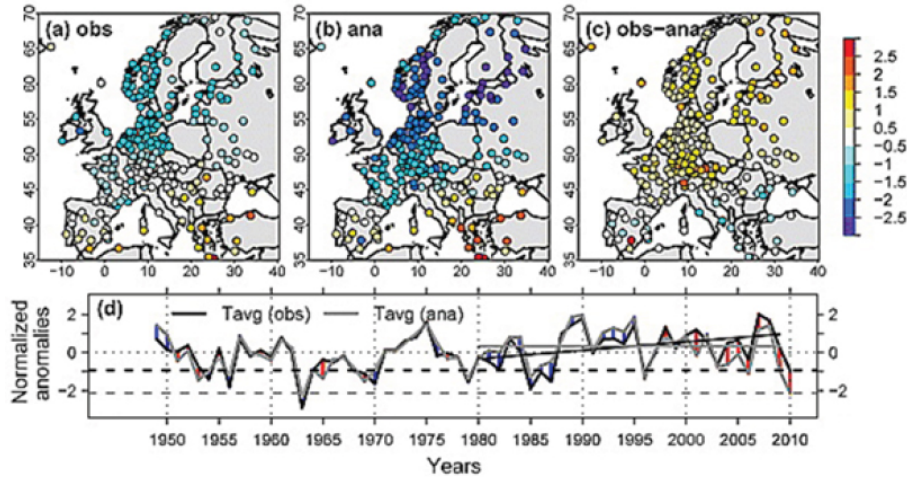


Figure 2.2: Analogs methodology applied to the unusually cold 2009-2010 winter in Europe. (a) Observed winter European temperatures; (b) average temperature of past winters flow-analogs; (c) difference between (a) and (b); (d) average temperature anomaly of winter 2009-2010 (black dashed line) compared with the one of flow-analogs (gray dashed line). Red (blue) segments represent positive (negative) observed-analogue differences. 1980-2009 linear trends for observed (black line) and analogs (gray line) temperatures are added. In all panels, anomalies are computed with respect to the 1961-1990 climatology and are normalized relative to the 1949-2010 anomalies distribution. Figure from Cattiaux *et al.* (2010) [6].

dynamic contribution to two heatwaves in Europe: the 2003 heatwave in Western Europe [55] and the 2010 heatwave in Russia [56]. For both heatwaves, the influence of ACC on the thermodynamics of the event had already been identified (see [81], [10] and [71]), while the emphasis on the dynamical contribution had been relatively low. The authors identify the two heatwaves with the circulation state of the hottest day and detect changes in the occurrence of analog circulation patterns. They find a positive trend for 2003 and no significant trend for 2010. Faranda *et al.* (2022) [25] analyze a set of extreme events that occurred in 2021 over Europe and North America and show that changes in the atmospheric circulation in the present climate significantly modified many of the extreme events under consideration. This is an example of an attribution study based on reanalysis data, in which factual and counterfactual climates are represented by recent and past climate conditions. Moreover, the authors show that the circulation pattern of Medicane Apollo [57] was extremely rare with respect to its analogs, making it a black swan event. Faranda *et al.* (2023) [26] apply the analogs methodology to the

2022 Euro-Mediterranean drought ([23], [24]). By using the century-long NOAA-CIRES-DOE Twentieth Century Reanalysis, version 3 [11] with start in 1836, they verify that the persistent anticyclonic anomaly over Western Europe characterizing the event has not become more frequent over the last two centuries. On the other hand, they find that ACC had a role in making such anomalies stronger and warmer in recent times, capturing the thermodynamic impact of ACC on the drought.

2.3 Description of the algorithm used to search analogs

In this section we describe the algorithm and the software used to search the atmospheric circulations analogs of the synoptic pattern observed over the western Mediterranean during 15 September 2022 Marche HPE (see Chapter 4). To identify the circulation analogs, we adapted to our purposes a MATLAB software devised by Faranda *et al.* (2022) [25]. This code is designed to select from a set of 2D fields those that minimize the Euclidean distance from a target field. Specifically, the following input is provided to the MATLAB function:

1. **The target field.** It is an atmospheric field highly representative of the atmospheric circulation state associated with the extreme event. For instance, it may be the SLP or Z500 on the day of the event and over the domain associated with it.
2. **The dataset.** This specifies in which dataset the analog search is done. It may be either a reanalysis or a global climate model simulation, which provides a time sequence of spatial fields as the target (i.e., daily SLP or daily Z500) over the same spatial domain.
3. **The number of analogs.** Fields in the dataset are ranked based on their Euclidean distance from the target field. We thus need to specify how many of the closest ones we take. This is done by setting a quantile as a percentage of the total number of fields in the dataset.

The MATLAB software estimates the Euclidean distance from the target field for all the time instances. For example, if we are dealing with daily SLP over a certain time period, the code runs through all days and calculates the distance of each daily SLP from the

target. Then, the desired number of best analogs are identified by selecting only those corresponding to a give percentile of the distance distribution. For example, we may choose the 1-th percentile - i.e., the 1% of the total closest to the target field. This is an arbitrary choice and results may depend on it. In general a compromise must be sought between the quality of the analogs - which would lead us to chose a very low percentile, e.g., 0.1% - and the number of analogs selects. After run, the MATLAB software returns, amongst other things, the time labels to identify when the circulations analogs which are found have occurred.

We now summarise the choices made in the present study for the inputs of the code (see also Section 4.1). The event is defined through the Z500 anomaly map at 0000 UTC on 15 September 2022. As far as the spatial domain is concerned, the longitude-latitude rectangle with boundaries 25°W - 24°E and 27° - 48°N is chosen as it contains the key atmospheric circulation pattern which drove the 2022 Marche HPE. As input dataset, we provide the ERA5 Z500 anomalies at 0000 UTC on each September-November day from 1 September 1940 to 14 September 2022. Therefore, our dataset consists of a time sequence of 7476 Z500 anomaly fields. We choose to extract the smallest 1% of Euclidean distances in the dataset, corresponding to 75 best analogs. We use the time labels output by the software to identify the analogs and examine their characteristics in factual and counterfactual climates.

Chapter 3

Analysis of the 15th September 2022 Marche flooding event

In this chapter, we analyze the precipitation associated with the event and we examine the ERA5 capability to capture it comparing it with observational datasets. We then describe synoptic-scale dynamical and thermodynamical drivers that characterized the initiation and maintenance of the HPE. Finally, we describe the relationship between the atmospheric circulation on the day of the event and the large scale flow evolution in the previous days.

3.1 Precipitation and major impacts

On 15 and 16 September 2022, central Italy and in particular the Marche region were hit by two consecutive HPEs. The first HPE was by far the most intense, and it occurred from the early afternoon of September 15 until midnight, with the heaviest rainfall occurring between 1600 UTC and 2200 UTC. Fig. 3.1 shows the evolution of the first HPE, providing four snapshots of the top of deep convective clouds on 15 September. We can identify the formation of a V-shaped mesoscale convective system (MCS) over Tuscany on the morning of the 15th because of the cloud-top V-shaped feature in Fig. 3.1a. In the early afternoon, the MCS moved eastward to the Adriatic side of the Apennines (Fig. 3.1b) and caused precipitation mostly in mountain areas. Late in the afternoon (Fig. 3.1c) the system evolved in a regeneration MCS, namely a system in which new

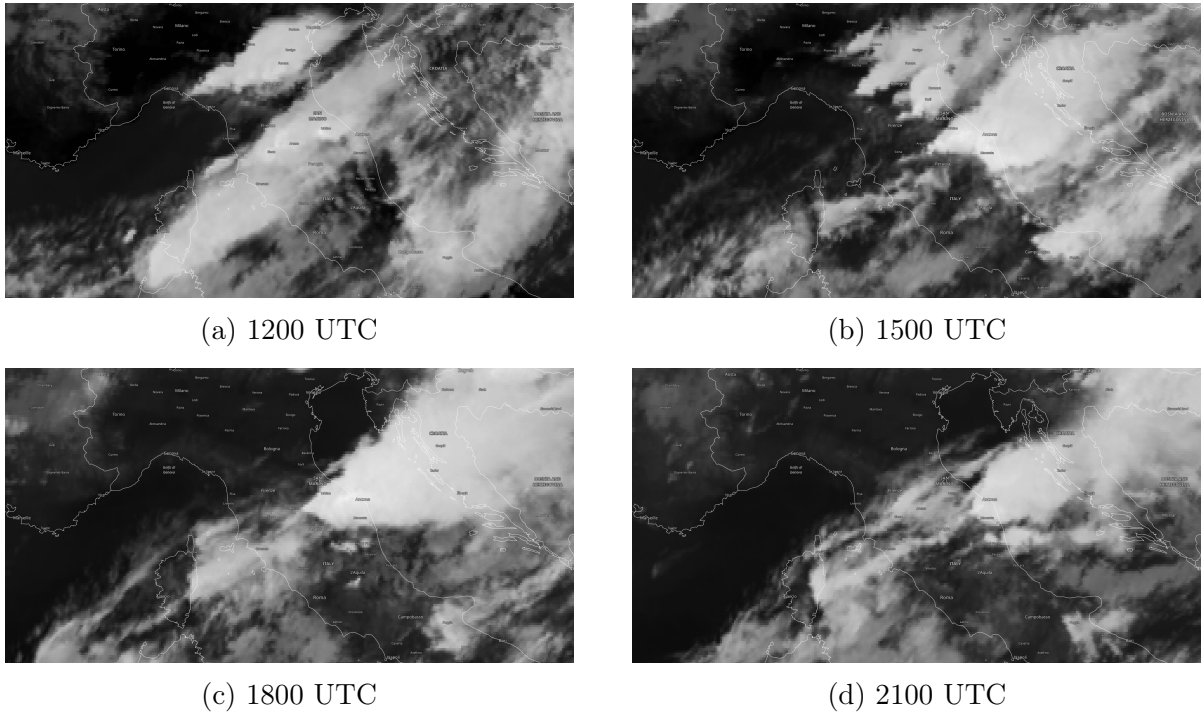
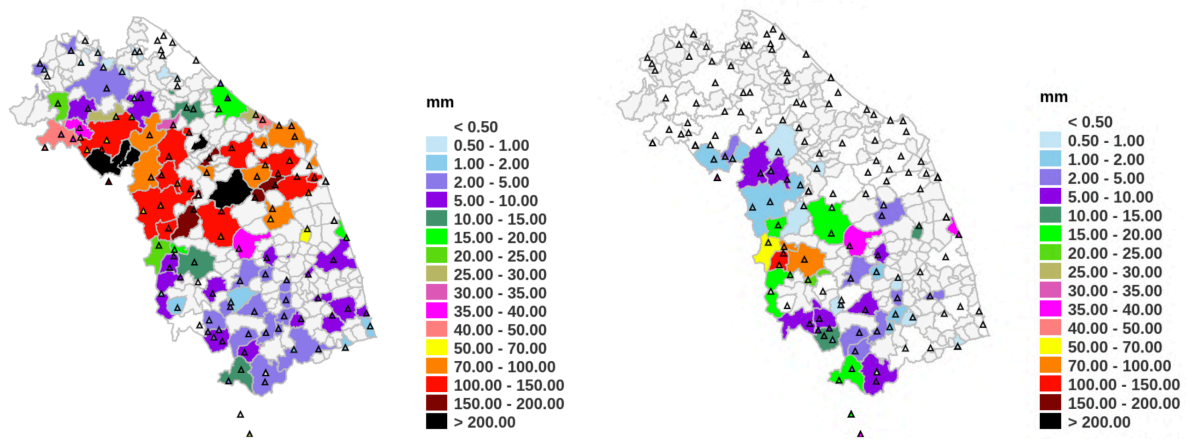


Figure 3.1: Meteosat SEVIRI satellite images of central Italy on September 15. The 10.8 micrometer channel highlights the evolution of high convective clouds. The development of the V-shaped MCS can be identified by the V-shaped feature displayed by the cloud-top. Figure from [22].

convective cells continually regenerate because of persistent low-level moisture convergence at approximately the same rate at which the older ones are advected away [7]. Such system stationed over the Marche region until late in the evening (Fig. 3.1d). During the night, the MCS drifted toward the Adriatic coast and terminated the convective activity.

V-shaped MCSs have been associated with severe weather events ([52], [5]). This type of system occurs when a strong updraft enters the lower stratosphere, causing an overshooting thunderstorm top. The overshooting top acts as a barrier against strong upper-level winds, and diverts the flow around it [27]. The presence of the cloud-top V-shaped feature is thus associated with strong tropospheric shear and intense updrafts, both crucial elements for severe thunderstorms [5]. McCann (1983) [52] explored the relationship between V-shaped MCSs and severe weather and found that most of these systems were associated with severe storms, though many severe storms are not V-shaped



(a) Precipitation accumulated from 1500 UTC (b) Precipitation accumulated throughout September 16.

Figure 3.2: Accumulated precipitation recorded by the regional rain gauge network. Colors refer to the maximum value in municipalities where at least one rain gauge is located. Figures from [3].

MCSs.

The 15 September HPE particularly affected the northern part of the Marche region in the provinces of Ancona and Pesaro-Urbino.

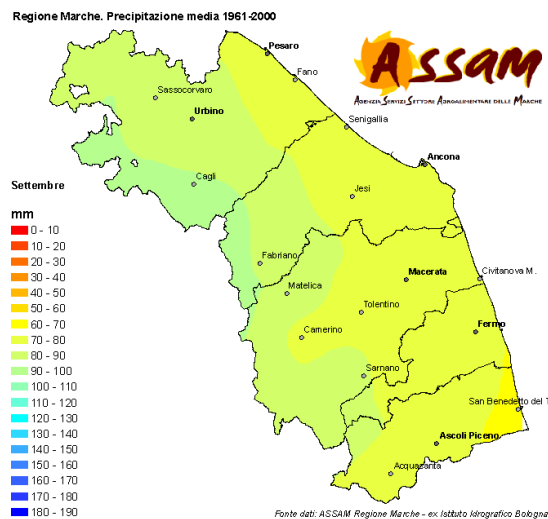


Figure 3.3: Average accumulated precipitation for the month of September over the period 1961-2000 in the Marche region. Figure from [2].

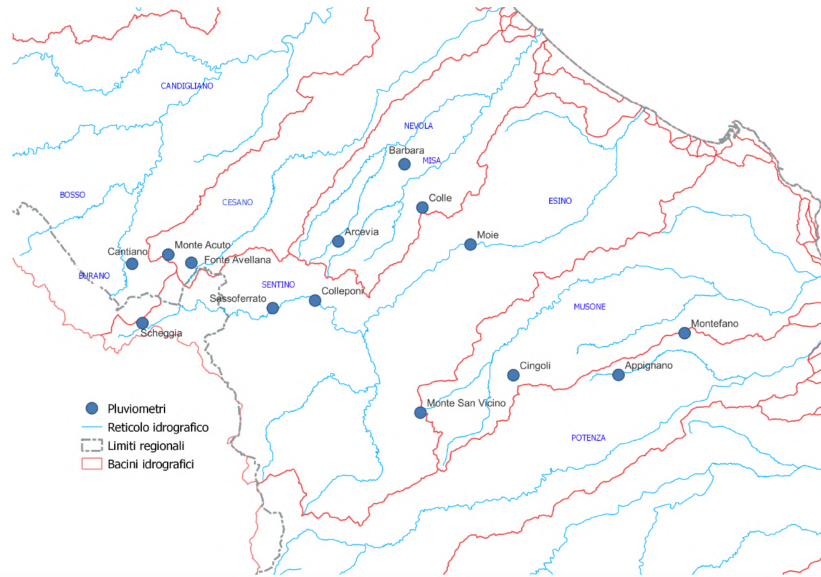


Figure 3.4: Area most affected by the September 15 HPE, located in the provinces of Pesaro-Urbino and Ancona. Blue dots represent rain gauges that made the most significant precipitation measurements. Major rivers are shown in light blue. Figure from [3].

Fig. 3.2a shows the accumulated precipitation from 1500 UTC to midnight recorded by the regional rain gauge network. We see that several stations recorded more than 70 mm, while rain gauges at Cantiano (Fig. 1.3b), Monte Acuto and Fonte Avellana (province of Pesaro-Urbino, locations in Fig. 3.4) measured more than 375 mm. These values are impressive when compared with the average accumulated precipitation for the entire month of September (Fig. 3.3), which ranges between 60 and 100 mm. The exceptional intensity of the HPE is confirmed by the return period of the recorded precipitation, estimated in the report by the Italian Civil Protection Department [3]: for both the rain gauges of Cantiano and Monte Acuto the return period is higher than 1000 years. This implies a probability of occurrence of 0.1% in any one year and characterizes a very rare and really extreme event.

3.2 Representation of the precipitation event in ERA5 and observations

As ERA5 is our primary dataset to examine the large scale drivers of the Marche HPE, we now assess its ability to capture the HPE. Since precipitation is not directly assimilated into ERA5 (as in all other reanalyses products), but it is generated by the atmospheric model of the ECMWF’s Integrated Forecast System, relevant errors still may exist in the precipitation field [4]. Consequently, we expect significant differences in the ERA5 representation of the Marche flooding event compared to observational datasets. To assess them, we take the IMERG observational dataset (see Section 2.1) as a reference for the description of the HPE.

Fig. 3.5a shows precipitation accumulated during September 15 as represented by IMERG. The intense precipitation that affected the Marche region is clearly visible: a large area with values greater than 70 mm can be identified in the provinces of Pesaro-Urbino and Ancona, with peaks of 150 mm. Values measured by the rain gauge network (Fig. 3.2a) are in substantial agreement when averaged over the same area since most instruments detect 70 to 150 mm. We see local differences between the two datasets, like the extreme measurements reported by a few rain gauges mentioned earlier that are not captured by IMERG. This is because we use the IMERG Late run that does not correct satellite data with rain gauges, as the Final run including rain gauges is not available for September 2022. However, we consider the IMERG dataset as the best description of the event, since the rain gauge network allows us to have detailed local information but unevenly spaced.

Figure 3.6a illustrates the precipitation that occurred on September 15, as represented by ERA5. The reanalysis does identify an intense precipitation event over central Italy, with local maxima between Marche and Tuscany, but does not localize it precisely. Furthermore, it underestimates its intensity: the maximum value is around 60 mm, which, while remarkable and highly indicative of an intense precipitation event, still underestimates the real event (see Fig. 3.2a and Fig. 3.5a). Finally, ERA5 does not capture the precipitation cluster off the Tuscan coast evident in Fig. 3.5a. There are several reasons why ERA5 fails to capture the details of the event. First, the spatial resolution (31 km, see Section 2.1.1) of ERA5 is too coarse to properly represent the interaction of the at-

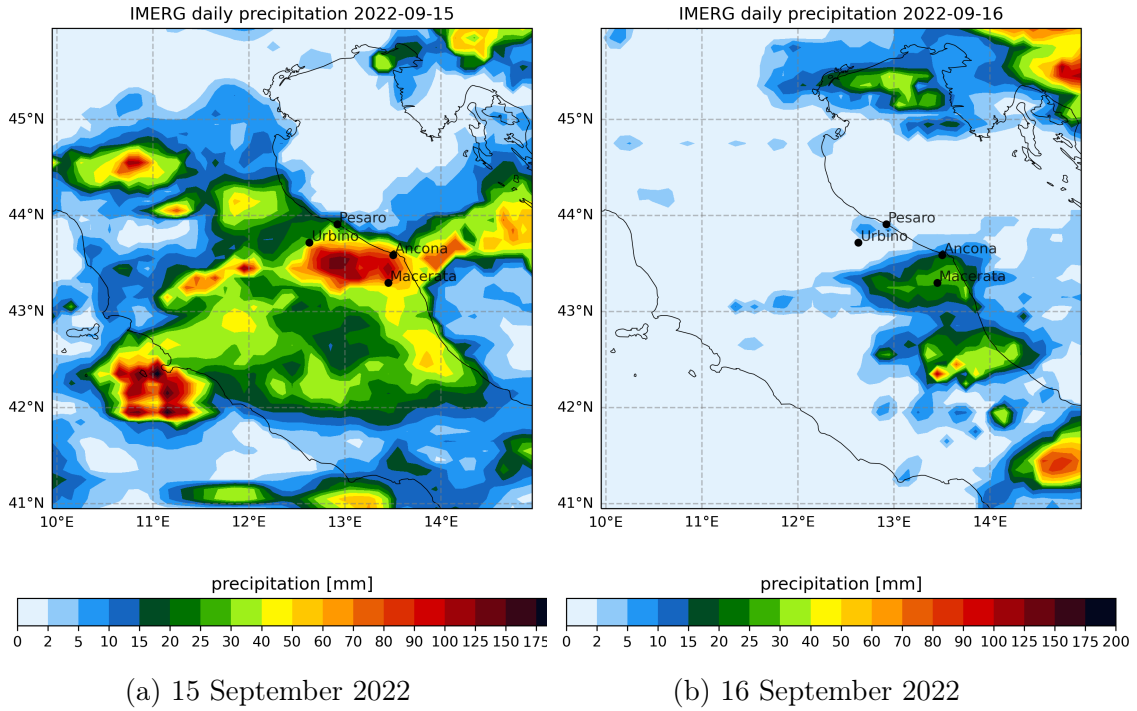


Figure 3.5: IMERG observational precipitation data over central Italy. The accumulation period is 24 hours. Black dots indicate the cities most affected by the HPE.

mospheric flow with orography. Specifically, Central Italy is characterized by a complex orography, with elevation growing from sea level to over 2000 m in less than 150 km and then falling again moving from west to east [58]. The orography of Central Italy is therefore underestimated and smoothed in ERA5. The general underestimation of maximum precipitation in HPEs was indicated by Lavers *et al.* (2022) [49]. They find that ERA5 cannot capture the highest observed precipitation totals but that it can generally model their locations and patterns. Second, reanalyses - as large-scale models and global climate models - use parameterized convection schemes to simulate deep convection, which constitutes a major source of errors and inaccuracies [68]. Recently, regional reanalyses at higher spatial resolution such as, for example, UERRA (11 km)[14] or SPHERA (2.2 km, convection-permitting) [28] have been developed to improve the representation of severe precipitation. It would have made sense to use them for this study, but unfortunately, they are not updated up to September 2022 (UERRA terminates in December 2019, and SPHERA in December 2020).

The second HPE took place on the early afternoon of September 16 and hit the

by the HPEs of 15 and 16 September have also been affected by the critical issues related with strong winds: falling branches and trees on roadways, involving in some cases cars, coastal erosion and shoreline damage due to wave reinforcement.

In summary, the most intense and destructive event was the V-shaped MCS on September 15th and this will be the one analyzed in the rest of this thesis work. Nevertheless, the HPE on the 16th and severe weather on the 17th are also significant because they affected an area already made vulnerable by the previous day's event and has complicated rescue efforts.

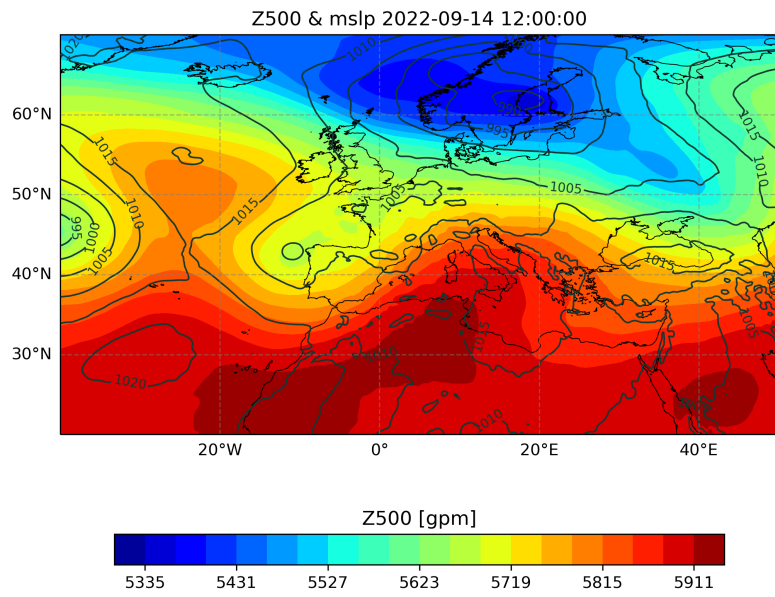
3.3 Large scale drivers of the 15 September Marche HPE

In this section, we discuss the large scale atmospheric circulation that led to the Marche flooding event, with particular emphasis on the water vapor transport by the atmospheric circulation over Central Italy.

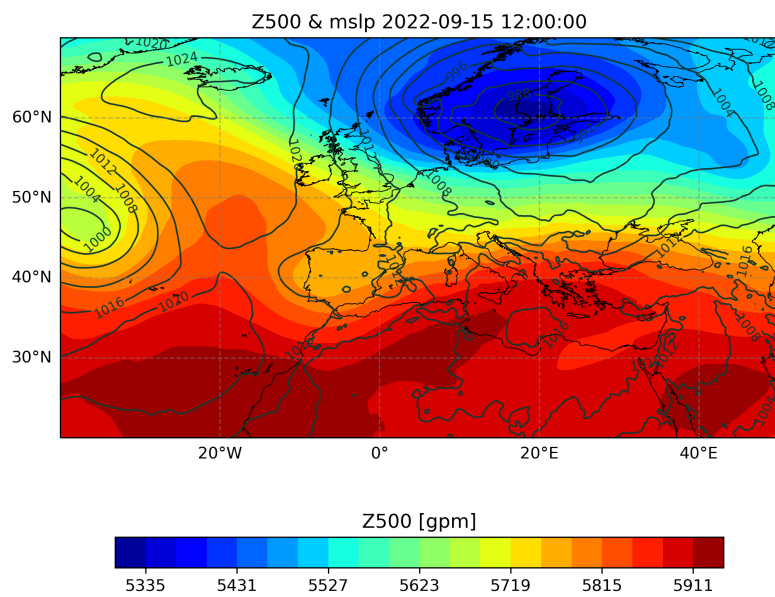
3.3.1 Synoptic-scale circulation

Fig. 3.7 shows the 500 hPa geopotential height and sea level pressure on 14 and 15 September. We note that, at 1200 UTC on September 14 (Fig. 3.7a), an middle-level trough is located over the northwestern corner of the Iberian Peninsula, while a high pressure ridge found over northwestern Africa and extending over southern Italy. At the surface, the mean sea level pressure exhibits a low center over Iberia corresponding to the upper-level trough. Such cyclonic circulation thus exhibit a vertical barotropic structure.

The trough-ridge dipole moves eastward on the following day (Fig. 3.7b), when a shallow surface anticyclonic circulation develops over the Ionian Sea between Calabria and Cyrenaica slightly shifted eastward with respect to the upper-level ridge. This configuration leads to the development of a predominant mid-tropospheric southwesterly and low-level southerly flow ahead of the trough that affected central Italy throughout September 15.



(a) 1200 UTC of September 14



(b) 1200 UTC of September 15

Figure 3.7: 500-hPa geopotential height (color shading) and mean sea level pressure (contours) on 14 and 15 September 2022.

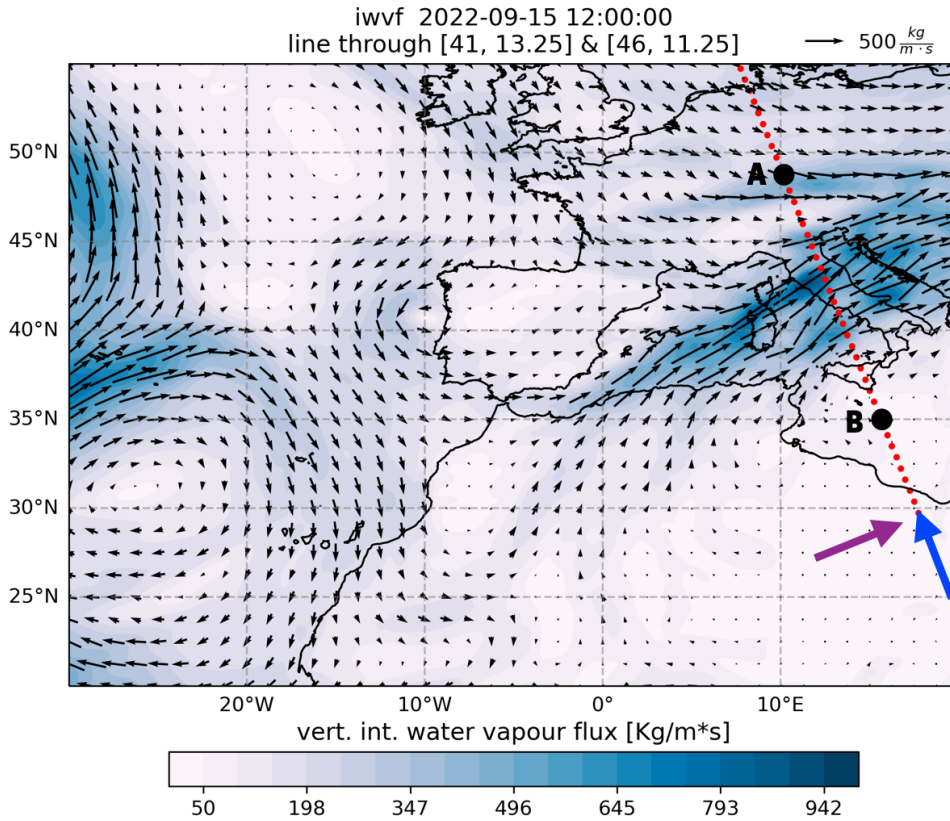


Figure 3.8: Vertically integrated water vapour fluxes (vectors, units: $\text{kg m}^{-1} \text{s}^{-1}$; color shading represents the magnitude of the fluxes) and 500 hPa geopotential height expressed (in meters, contours) on September 15th, 1200 UTC. The red-dotted line shows where the vertical section is taken. The black dots A (48° N) and B (35° N) represent the latitudinal range analyzed. The purple and blue arrows indicate the positive sign adopted for the normal and tangent flow, respectively.

3.3.2 Atmospheric water vapour fluxes

Fig. 3.8 shows the vertically integrated water vapour flux at 1200 UTC on September 15th. From a visual inspection, we can see that the southwesterly flow associated with the middle-level trough over Iberia has a high moisture content. The water vapour flux is approximately parallel to the Z500 contours. Since the upper-atmosphere contains very little water vapour because of the low temperatures, this implies that a large fraction of the vertically integrated moisture flux comes from the middle-tropospheric water vapour transport. This southwesterly moisture flux persists over central Italy throughout the day

and has a critical role in providing moisture to the MCS which develops over Central Italy. The role of the upper-level trough in the precipitation event observed over the Marche regions seems to be typical of HPE over the Mediterranean basin. Jansa *et al.* (2001) [44] analyzed HPEs and found that 90% of HPEs in western Mediterranean occur with a cyclonic centre in the vicinity connected with an upper-level trough, usually located in a way that favours the creation and intensification of a moist flow feeding the event. Davolio *et al.* (2022) [17] examine the HPE that affected northern Italy on 2-3 October 2020 and find that it was associated with a upper-level trough over the western Mediterranean basin which was associated with an intense atmospheric river ¹.

To better characterize the transport of water vapour towards Central Italy, we analyze the vertical cross section of moisture flux over the Marche region. This approach has proven to be very useful in the analyses of HPEs as it demonstrates the role of atmospheric water vapour transport in triggering HPEs. For example, Davolio *et al.* (2020) [16] - in their study on the Vaia storm that affected Italy on 27–30 October 2018 - analyzed the water vapour transported by an atmospheric river originating in the tropical Atlantic across several vertical cross sections and found that the atmospheric river contribution was a key factor for heavy precipitation associated with the Vaia storm. Similarly, Davolio *et al.* (2022) [17] used several vertical cross sections to identify the different components of water vapor fluxes associated with the HPE that affected northern Italy on 2-3 October 2020. Here, to analyze the vertical structure of the moist flow feeding the Marche HPE, we select a vertical section passing over the Marche region and oriented perpendicularly to the vertically integrated moisture flux (Fig. 3.8). We then evaluate the dependence of the moisture flux on height for both the normal and the parallel component of the flux (purple and blue arrows in Fig. 3.8).

The evolution of the normal moisture flux for the afternoon of September 15 is shown in Fig. 3.9. We identify an intense southwesterly moisture flux localized over the Marche region (lat.44°-42°) extending from the surface to the middle troposphere up to 600 hPa (approximately 4000 m a.s.l.). Values of the moisture flux over Central Italy remained very high during the afternoon and until late in the evening of the 15th, feeding the mesoscale convective system. Fig. 3.10 shows the evolution of the tangent moisture flux and points out a new feature that was not evident from the analysis of the vertically inte-

¹An atmospheric river is a long and narrow structure of water vapor typically originating over the tropical sea and reaching midlatitude lands [91]

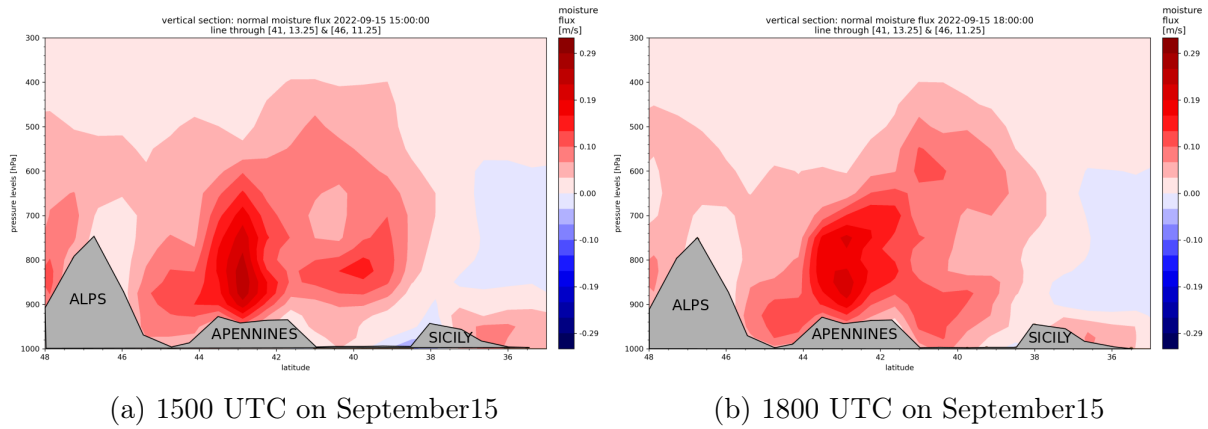


Figure 3.9: Moisture flux component normal to the vertical section shown in Fig. 3.8. Latitudinal range: 48° - 35° N, as shown by points A and B in Fig. 3.8. Positive values correspond to a southwesterly flux. The Marche region is located at 44° - 42° N.

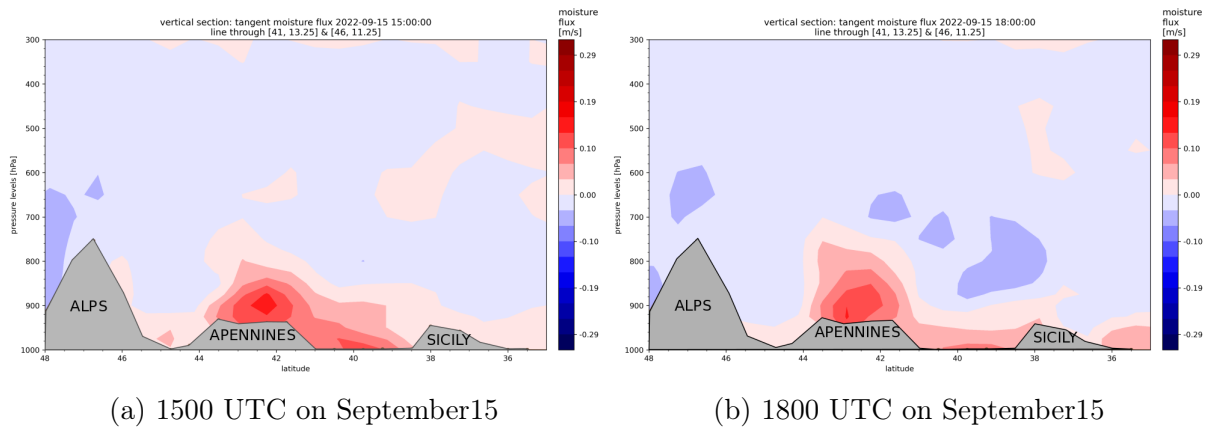


Figure 3.10: Moisture flux component tangent to the vertical section shown in Fig. 3.8. Latitudinal range: 48° - 35° N, as shown by points A and B in Fig. 3.8. Positive values correspond to a southeasterly flux. The Marche region is located at 44° - 42° N.

grated water vapour flux: a southerly component of the moisture flux confined in lower troposphere and persistent over Central Italy. From the examination of the moisture flux over the lower troposphere (Fig. 3.11), we can see that this southerly component is related with the anticyclonic circulation around the surface high pressure centre located in the Ionian Sea (Fig. 3.7b). As the southerly moisture flux impinges on the Apennines it is forced to rise and joins the southwesterly flux, providing additional water vapor and hence further strengthening the low-level moisture flux.

Surface wind field is shown in Fig. 3.12. In addition to the southerly and southwesterly components (visible in the region from the Strait of Sicily to the Tyrrhenian sea and in western Mediterranean, respectively), a region with northwesterly mistral winds can be identified in the Gulf of Lion. Mistral surface wind brings drier (Fig. 3.8) continental air over the Mediterranean sea. The convergence of these three different low-level air masses was important for the initiation of convection, particularly in the region between Sardinia, Corsica, and the Italian peninsula, where the orography forced the flow to rise uphill. Here a region of pronounced low-level convergence was found in the hours before the HPE (Fig. 3.12, color shading) and this constituted a trigger for convection, as can be seen in the development of high convective clouds in Fig. 3.1a. This low-level flow configuration characterized by strong convergence over the Tyrrhenian Sea is often associated with HPEs [58]. Lee *et al.* (2016) [50] identified the western Mediterranean as a privileged region for the initiation of convection. In fact, this region is very unique in terms of orography because of the presence of coastal mountainous region (e.g. Alps, Apennines, Pyrenees) and of mountainous islands (e.g. Corsica, Sardinia, Sicily), that can act as forcing on the low-level flow. The Mediterranean, that represents a source of moisture and heat, and such coastal slopes are key factors in triggering the convergence and the uplift of moist and unstable air masses, resulting in convection over Italy [58]. In fact, northern-central Italy is one of the region in Europe with the highest percentages of extreme precipitation days over the total number of wet days, according to Isotta et al. (2014) [43]. These kind of events have a relevant socioeconomic impact and kill or injure people almost every year [72].

To sum up, we identify three wind components acting in the western Mediterranean which are key to the development of the HPE:

1. An intense southwesterly moist flux from surface to the middle-atmosphere and associated with the trough centered over the Iberian Peninsula. Such flux was localized and persistent over the Marche region throughout September 15.
2. A near-surface southerly moisture flux associated with the surface high pressure centered over the Ionian Sea, also stationary over Marche on the day of the HPE.
3. Drier northwesterly mistral winds that enter the Mediterranean from the Gulf of Lion, which forced strong low-level convergence.

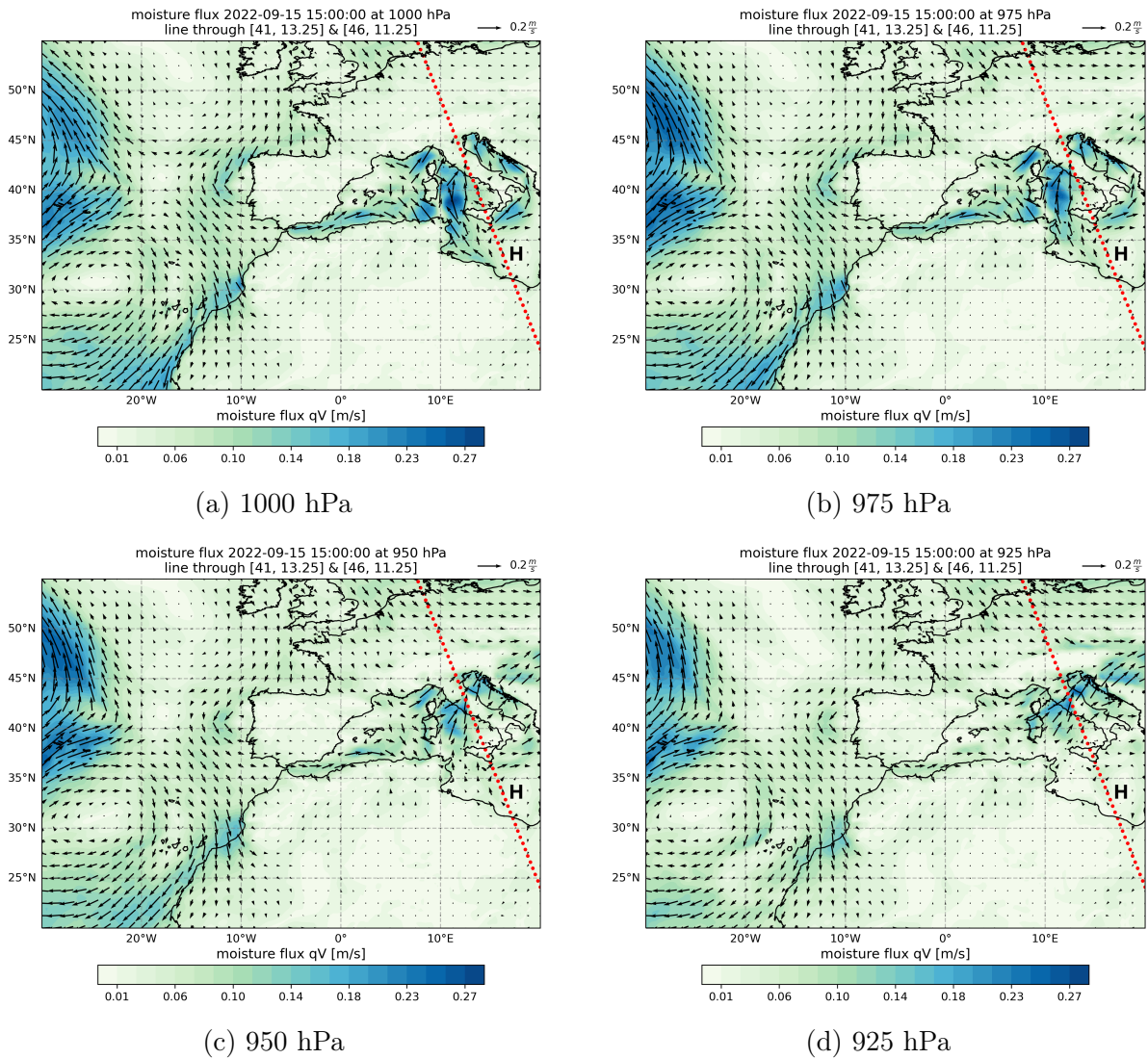


Figure 3.11: Moisture flux (1500 UTC) at (a) 1000 hPa, (b) 975 hPa, (c) 950 hPa, and (d) 925 hPa. The centre of the surface high pressure on the Ionian Sea is evident at 1000 hPa and it is highlighted by an "H".

The interaction between the three components resulted in an area of pronounced convergence on the coast of Tuscany, triggering the formation of high convective clouds.

This dynamic configuration is similar to the one described by Lee *et al.* (2016) [50] in their analysis of two consecutive HPEs that affected southern Italy in October 2012, both associated with multi-cell V-shaped regeneration MCSs. The authors identified three distinct regions with different surface wind components: a region with predomi-

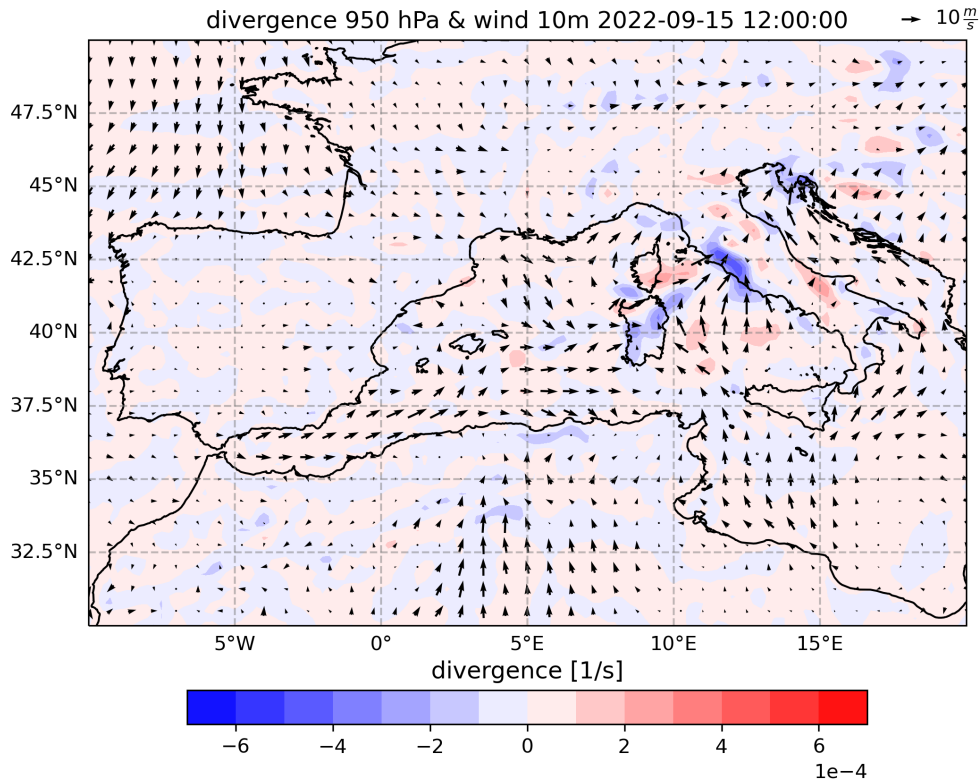


Figure 3.12: Horizontal wind divergence at 950 hPa (shading) and 10m winds (vectors) at 1200 UTC on September 15.

nantly mistral winds extending from the Gulf of Lion, a region with westerly to southwesterly winds located between the north coast of Algeria and the Tyrrhenian sea, and a region with southeasterly winds coming from the Strait of Sicily. The low-level convergence of these surface winds was found to be a crucial factor for both the initiation and maintenance of convection. Other important factors were identified in the high moisture content and high convective available potential energy (CAPE), that are examined in the following for the case of the Marche HPE.

The atmospheric circulation and water vapour fluxes of our case study is also comparable to the one described by Miglietta and Davolio (2022) [58]. They study the mechanism responsible for HPEs in Central Italy and identify the eastward moving upper-level trough over the western Mediterranean, low-level convergence over the Tyrrhenian Sea and high low-level moisture content, three elements that we observe also in our case study, as a typical configuration conducive to severe convection.

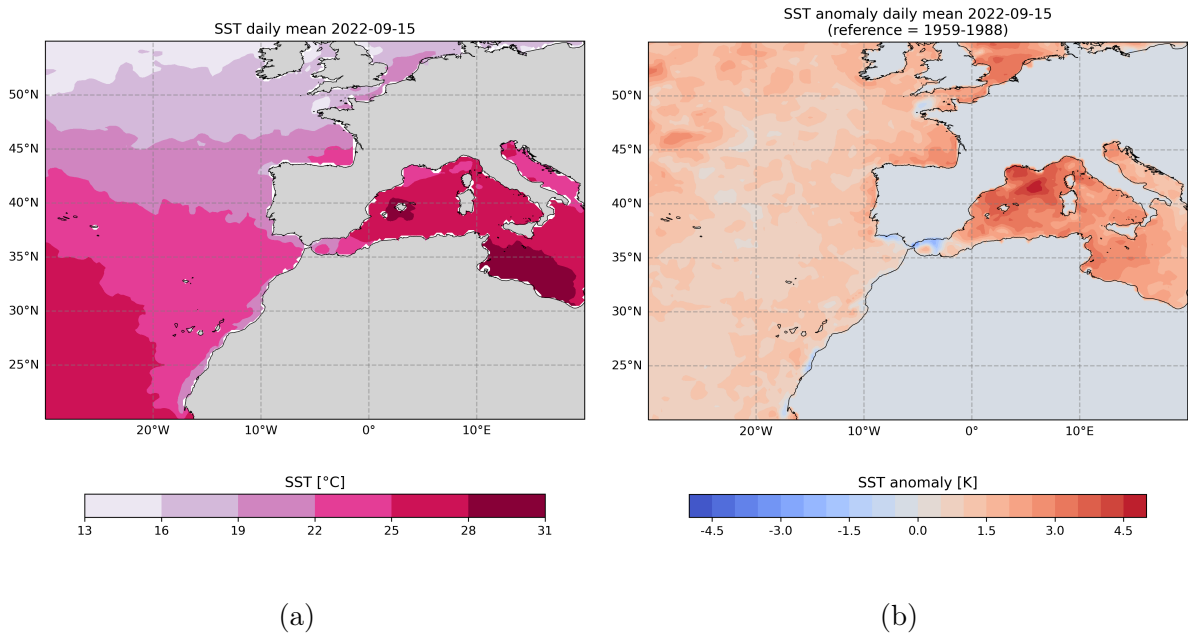


Figure 3.13: (a) mean SST and (b) mean SST anomaly for September 15. The anomaly is computed with respect to the average September temperatures over the thirty-year period 1959-1988.

3.3.3 Sea surface temperatures and thermodynamic environment

We finally examine the state of the sea surface and the thermodynamic environment in which the Marche HPE developed. We thus analyze sea surface temperature (SST), precipitable water (PW) and convective available potential energy (CAPE) on 14 and 15 September 2022.

First, we examine SST to check if higher temperatures in that period had a role in exacerbating the precipitation event. High SST are found in the whole western Mediterranean basin, generally above 25°C), associated with large SST anomaly up to 4.5°C between Spain and Sardinia (Fig. 3.13).

We then examine the CAPE to assess to what extent the environment was favourable to the development of convection, and we analyze PW to check the efficiency of convection in generating precipitation. At 0000 UTC and 1200 UTC on September 14 (the day before the HPE), PW exhibited an elongated high-value feature over northern Morocco and western Mediterranean (Fig. 3.14a and 3.14b), suggesting that part of the PW available in the Mediterranean came from the Atlantic Ocean. Again, the particular location of

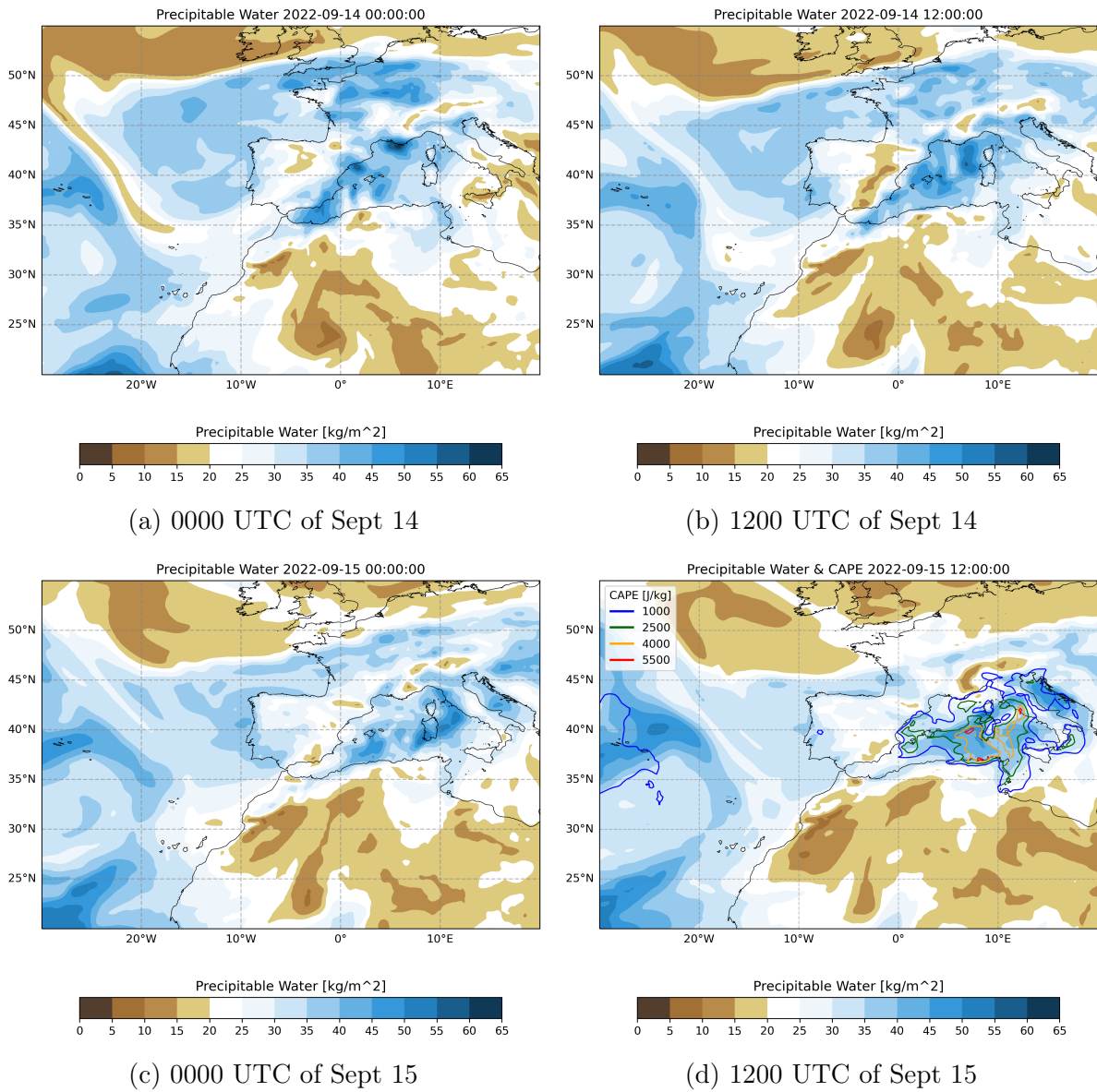


Figure 3.14: Evolution of PW before the event. Shades of blue indicate areas with high PW content ($>25 \text{ Kg m}^{-2}$). (d) contours: CAPE few hours before the event.

western Mediterranean makes several moisture sources (Atlantic ocean, tropical Africa) available to convection feeding [50]. This contribution originating remotely is added to the local evaporation from the sea, resulting in very large values of PW: in the western Mediterranean PW is generally larger than 25 Kg m^{-2} , reaching peaks up to 50 Kg m^{-2} or even larger. For comparison, note that in the HPEs analyzed by Lee *et al.* (2016)

[50] the maximum value of PW was around 35 Kg m^{-2} . PW values associated with the Marche HPE are well above the seasonal average, as can be seen from the anomaly computed for 0000 UTC on September 14 (same as Fig. 3.14a) shown in Fig. 3.15: a band with large positive anomalies stretching from northern Morocco to northern Italy is clearly delineated. By following the evolution of the PW, we can see that on September 15 (Fig. 3.14c and 3.14d) the plume coming from the Atlantic channeled its PW contribution in the area between the Balearic islands and the Italian peninsula, where PW reaches its peak (up to 55 Kg m^{-2}).

CAPE at 1200 UTC on September 15 (few hours before the HPE) is displayed in Fig. 3.14d (contours). We can see that CAPE was higher than 1000 J Kg^{-1} in this whole region, reaching the extreme value of 5500 J Kg^{-1} over the Tyrrhenian Sea. Consider that CAPE values that exceed 1000 J Kg^{-1} are associated to thunderstorm environments and only in rare cases they are bigger than 5000 J Kg^{-1} [13]. The comparison with the HPEs described by Lee *et al.* (2016) [50] is remarkable: in that case CAPE reached the maximum value of 2000 J Kg^{-1} . CAPE and PW values remain high also during the event, maintaining an environment favourable to convection.

The thermodynamic conditions appear then to be very favorable to sustain the continuous formation of convection, as we find high values of SST, PW and CAPE over the western Mediterranean right before the start of the event. This thermodynamic environment and the continuous southwesterly flow make central Italy and the Marche region a prime area for the development of an HPE.

Western Mediterranean is outlined as the crucial area for the trigger of the HPE on September 15, as it is the region where all of the key features were found. This region has been suggested to be a preferential area for convective systems genesis, especially the areas of Balearic Islands and Ionic and Tyrrhenian seas, where these systems develop mainly in September and October [54]. Grazzini *et al.* (2020) [29] provide a dynamical classification of HPEs in northern-central Italy and identify three dynamical classes. The third category is of particular interest to us because it describes HPE driven by non-equilibrium convection, like the Marche flooding event. The events are generated in an unstable environment associated with high CAPE values and abundant PW. The triggering of these events is determined by a complex interaction between flow and orography. Events belonging to this class typically occur between mid-May and late October, with the greatest frequency from mid-August to mid-September. Moreover, the authors

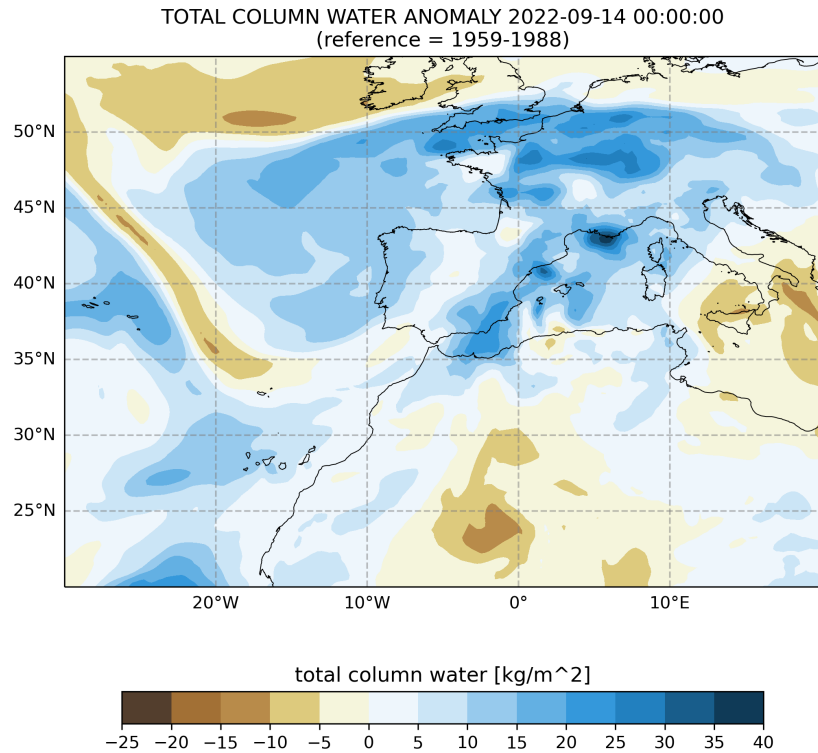


Figure 3.15: PW anomaly at 0000 UTC on 14 September 2022. The anomaly is computed with respect to the average September temperatures over the thirty-year period 1959-1988.

emphasise the difficulty in predicting this type of event that depends on the detail of the CAPE pattern.

3.4 Planetary scale drivers

As mentioned earlier, the two main contributions to the moist flow that fed the convective system are the southwesterly flow connected with the low pressure over Iberia and the superficial southerly flow associated with the high pressure over the Ionian Sea. The pair H-L and its specific shape and orientation were thus crucial in determining the favorable conditions under which the HPE developed. It is therefore natural to ask ourselves whether such H-L pair and their time evolution was caused by a remote signal like, for example, a synoptic Rossby wave [36]. Grazzini *et al.* (2021) [30] analyze the connection

between HPEs over northern-central Italy and Rossby wave packets (RWPs) propagation. They show that the occurrence of HPEs does not depend only on local conditions, but also on the large-scale flow evolution in the days before the events. Specifically, RWPs have an influence on the dynamical forcing and convergence of water vapour, that are key element for the occurrence of extreme precipitation.

To detect the presence of a RWP in our case study, we look at the evolution of the 500 hPa geopotential height at a planetary scale in the northern hemisphere the days before the event, shown in Fig. 3.16. We see that this pair was part of a larger structure characterized by alternating troughs and ridges. This is particularly evident on the 12th and 13th of September 2022 (top panels in Fig. 3.16). As the energy associated with the RWP reaches the Mediterranean Sea on the 15th, the high pressure there becomes more zonally elongated (bottom right panel in Fig. 3.16), driving the southwesterly moisture flux into Central Italy. The Z500 pattern shown in Fig. 3.16 clearly suggests the presence of a RWP propagating over the Atlantic ocean in the days before the event and eventually reaching Europe. The presence of a RWP is also highlighted by the behaviour of the horizontal wind at 300 hPa (Fig. 3.17a), which features large meridional meanders in certain regions, while in others is more zonally oriented. The same behaviour

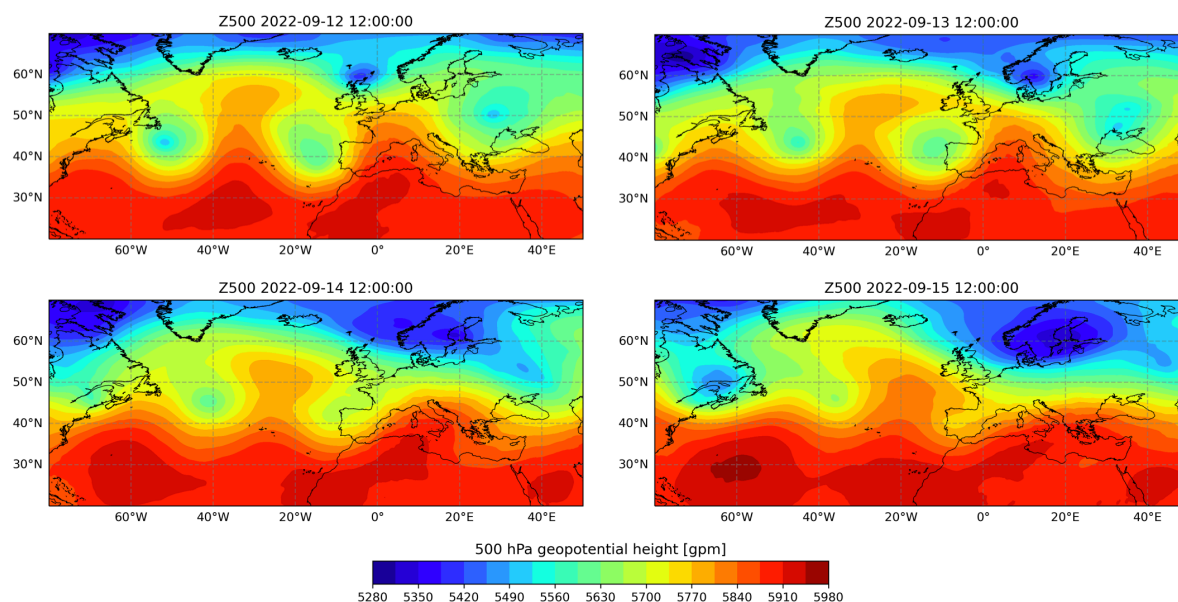


Figure 3.16: Evolution of 500-hPa geopotential height in the days before the event (12, 13 and 14 September) and in the day of the HPE.

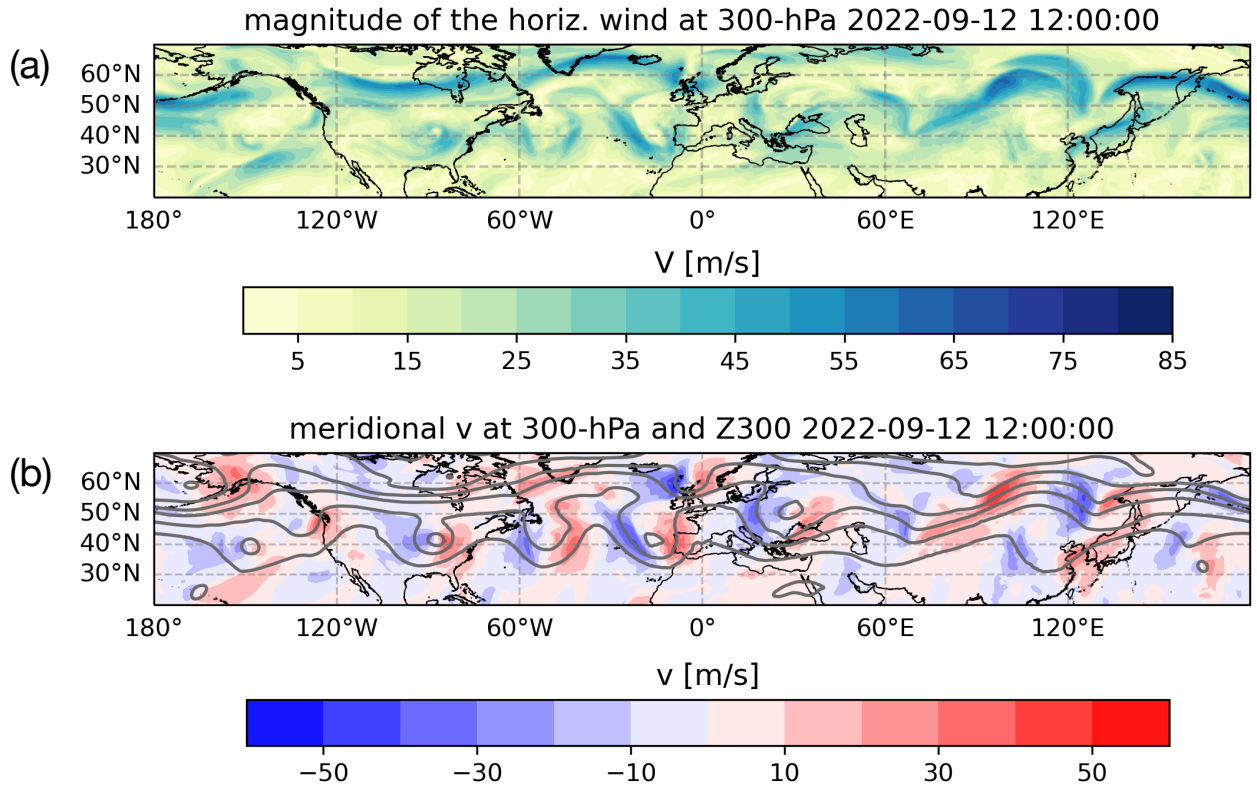


Figure 3.17: (a) Magnitude of the horizontal wind at 300 hPa; (b) Meridional wind v at 300 hPa (color shading) and isolines of 300-hPa geopotential height Z (grey contours), both at 1200 UTC on 12 September 2022 at (same time of Fig. 3.16 top left.)

is highlighted by the meridional wind v shown in Fig. 3.17b (shading) along with the 300 hPa geopotential height (contours). The large scale flow is approximately along lines of constant geopotential height as the large scale winds in the free atmosphere are close to being geostrophic. In the area between eastern North America and Europe, geopotential height contours feature a strong undulation and thus also v exhibits deviations from the zonal directions, alternating positive and negative values. This allows us to identify where the RWP is in the days before the HPE.

To simplify the localization of the RWP, we produce an Hovmöller diagram [37] for v at 500 hPa (Fig. 3.18) to diagnose the presence of a RWP and to follow its evolution more easily. The RWP detected in the Hovmöller diagram lasted from 9 to 15 September and

originated over eastern North America. The pair low (L) - high (H), with L over Iberia and H over southern Italy, was then associated with the RWP transit. In particular, the trough that determined the low pressure centre over Iberia can be recognized in the pair of patches indicated by the turquoise oval in Fig. 3.18. The energy associated with the RWP reaches the Mediterranean Sea on the 15th causing a modification of the L-H pair

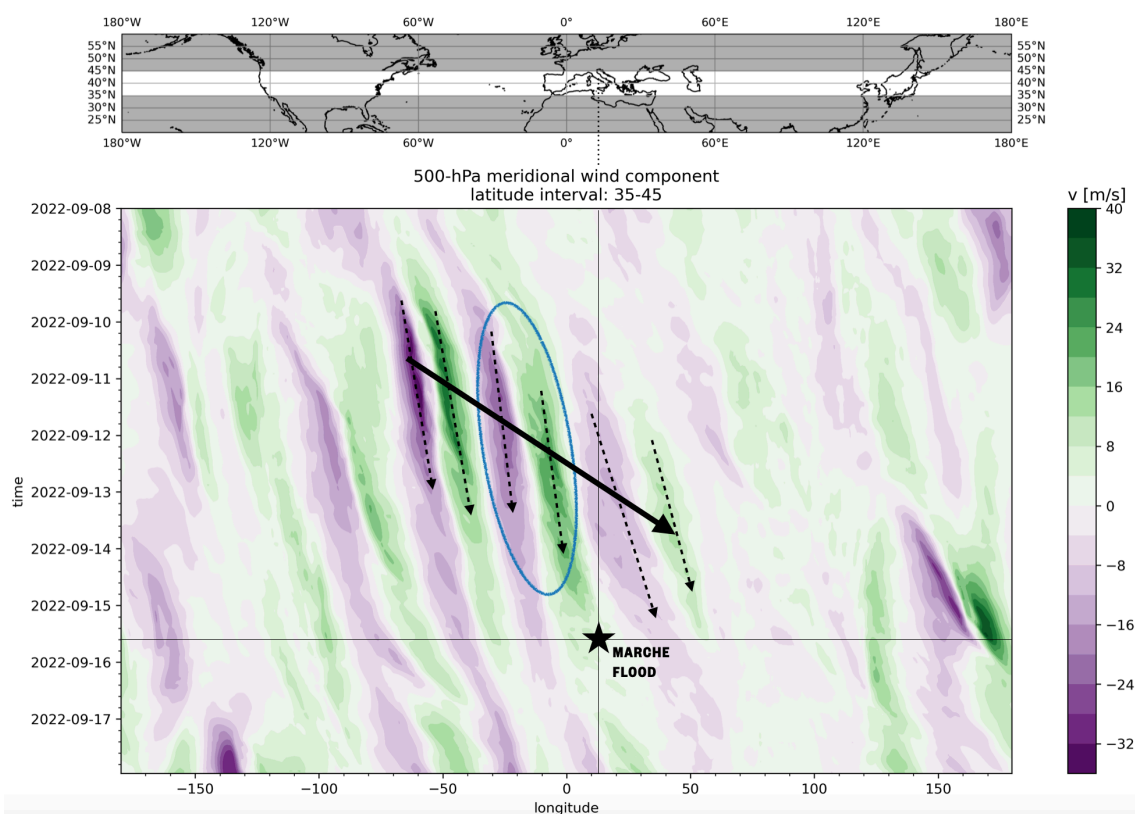


Figure 3.18: Hovmöller diagram [37] of the meridional wind v at 500 hPa: the latitudinal average of v between 35°N and 45°N (highlighted in the map) is plotted as a function of longitude and time. Pairs of green and purple patches represent individual troughs and ridges. The envelope in which these patches are organized represents the RWP. Slopes of the dashed arrows indicate the velocity at which individual minima and maxima propagate (phase velocities), while the solid arrow indicates the propagation velocity of the RWP (group velocity). The thin lines cross at the point corresponding to the HPE, represented by the star. The pair of green and purple spots enclosed by the turquoise oval indicates the evolution of the upper-level trough over Iberia (Fig. 3.7 and 3.16). The latitude range over which the average was performed was defined based on the latitude range of the undulations of $Z500$ (Fig. 3.16).

and leading to a more zonally elongated shape (bottom right panel in Fig. 3.16), which in turn drives the southwesterly moisture flux into Central Italy. The RWP was thus crucial to the occurrence of the HPE, as it led to a spatial configuration of geopotential height field consistent with the observed moisture flux.

As shown in previous studies ([50], [17] and [29]), the presence of a meridionally elongated upper-level trough is a favourable condition for the occurrence of extreme weather events. The fact that sometimes such trough is part of an RWP in its decay stage is very relevant because it suggests that RWPs can be precursors of extreme events and therefore can help in the prediction of the event days before it happens. However, not all extreme weather events occur in the context of an RWP, and this connection is not systematic. The existence of specific conditions that make an RWP a precursor to extreme weather is still an open question and more research is needed to investigate such relationship [88]. The RWP detected in the our case study was however certainly essential in determining the large-scale conditions in which the Marche flood occurred.

Chapter 4

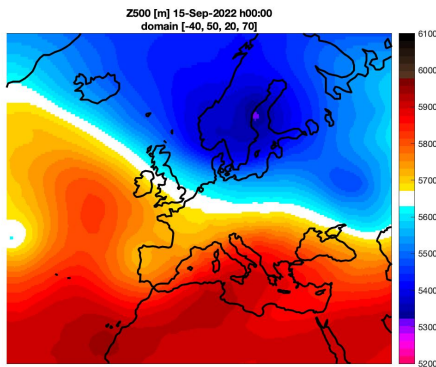
Analog-based analysis of the Marche high precipitation event

In this chapter we apply the analogs methodology for extreme events attribution to the 15th September 2022 Marche flooding event. We use the methodology to find past flow-analogs of the large scale atmospheric circulation that led to the HPE and hence to examine if and how these configurations have substantially changed because of anthropogenic global warming. This piece of analysis was carried out while visiting Dr. Davide Faranda at the Laboratoire des Sciences du Climat et de l'Environnement in Paris, France.

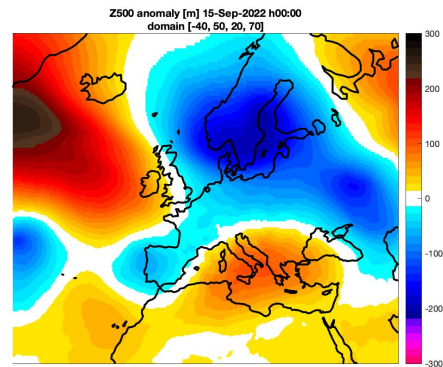
4.1 Preliminary tests and choice of the domain

We begin identifying the variable representing the atmospheric circulation state associated with the event. We choose Z500 (Fig. 4.1a) because the moist southwesterly flow that had a critical role in feeding the MCS with moisture was largely directed as Z500. We decide to remove the seasonal cycle (subtracting the average of Z500 for 15 September of each year from 1940 to 2022) to compare months with different circulations. We then define the event with the Z500 seasonal anomaly at 0000 UTC on 15 September 2022 (Fig. 4.1b).

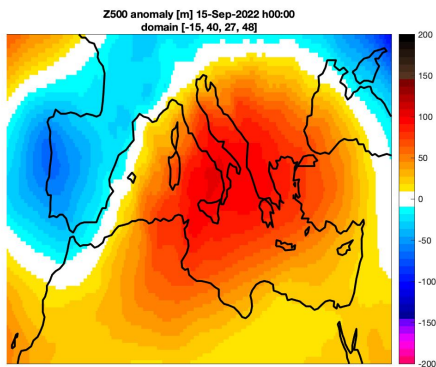
We then choose the size of the domain on which the analogues search is performed. The analog methodology is sensitive to the domain extent, as shown, for example, in



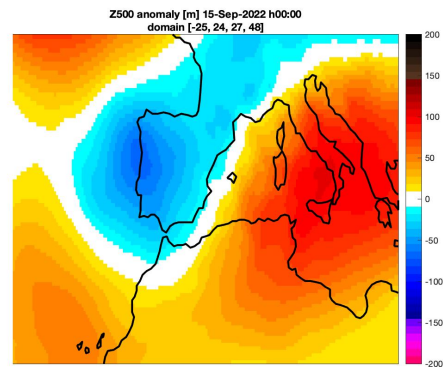
(a) variable: Z500 at 0000 UTC on 2022-09-15, domain: $[-40^{\circ}\text{W}- 50^{\circ}\text{E}$ and $20^{\circ}-70^{\circ}\text{N}$].



(b) variable: Z500 anomaly at 0000 UTC on 2022-09-15, domain: $[-40^{\circ}\text{W}- 50^{\circ}\text{E}$ and $20^{\circ}-70^{\circ}\text{N}$].



(c) variable: Z500 anomaly at 0000 UTC on 2022-09-15, domain: $[-15^{\circ}\text{W}- 40^{\circ}\text{E}$ and $27^{\circ}-48^{\circ}\text{N}$].



(d) variable: Z500 anomaly at 0000 UTC on 2022-09-15, domain: $[-25^{\circ}\text{W}- 24^{\circ}\text{E}$ and $27^{\circ}-48^{\circ}\text{N}$].

Figure 4.1: Choice of the event definition and of the geographical domain of research. The search for analogues was performed in these four cases and 4.1d was chosen as the best definition: the use of Z500 anomalies allows to compare different months' circulation, and the negative anomaly over Iberia that caused the southwesterly flow is the main feature within the domain.

Jézéquel *et al.* (2018) [46]. In this study the authors evaluate the influence of several parameters (e.g. the variable defining the event, the size of the domain, the number of analogs) on the computation of analogs applied to European heatwaves and find that small domain centered on the Z500 anomaly associated with the event improve the analog search.

To test the sensitivity to the domain extent in our case study, we define three different domains:

1. a large domain including Europe, the eastern Atlantic and North Africa, with boundaries: $-40^{\circ}\text{W} - 50^{\circ}\text{E}$, $20^{\circ}\text{N} - 70^{\circ}\text{N}$ (Fig. 4.1b).
2. a domain that includes the entire Mediterranean area, with boundaries: $-15^{\circ}\text{W} - 40^{\circ}\text{E}$, $27^{\circ}\text{N} - 48^{\circ}\text{N}$ (Fig. 4.1c)
3. a domain centered over western Mediterranean and including the eastern Atlantic, with boundaries: $-25^{\circ}\text{W} - 24^{\circ}\text{E}$, $27^{\circ}\text{N} - 48^{\circ}\text{N}$ (Fig. 4.1d)

We initially performed the search for the best analogs on the first domain. This choice was not ideal since the Z500 anomaly dipole over Scandinavia and the North Atlantic (Fig. 4.1b), which is the dominant feature within this domain but is not so relevant for the weather over Italy, was the circulation that was searched for. From a visual inspection, we see that the analogs did not present the H-L pair over the Mediterranean Sea. As such pair is the crucial factor in determining the humid flows that fed the event, we decided to search for analogs on the second domain centered over the Mediterranean area (Fig. 4.1c). This choice improved the analogs selection, which presented a Z500 anomaly pattern similar to that of the event in the Mediterranean area. However, we inspected precipitation fields associated with this second set of analogs, and few of them presented heavy precipitation in Central Italy. As a third choice, we shifted the domain westward and trimmed the latitudes to the east of Italy (Fig. 4.1d) to better represent the upper-level trough in western Mediterranean, which was the key driver of the southwesterly moist flux that triggered the event. After carefully considering the three cases, we adopted the latter domain for the analogs search, since the circulation states we found feature the best reproduction of the Z500 pattern and associated precipitation.

4.2 Analogs of the 15th September circulation pattern

After defining the event and domain, we perform the analogs detection using Z500 at 0000 UTC on each autumn day (September, October and November) from the ERA5 reanalysis database from 1 September 1940 to 14 September 2022 (the day before the event). The choice of performing the analyses on autumn days only is motivated by the

<u>1944-09-09</u>	<u>1944-09-10</u>	<u>1944-09-11</u>	<u>1944-09-12</u>	<u>1944-09-13</u>	<u>1945-09-02</u>
1945-09-03	1946-09-09	1946-10-20	1947-10-09	<u>1949-09-30</u>	<u>1949-10-01</u>
<u>1949-10-02</u>	<u>1951-10-30</u>	1952-09-01	1952-09-15	1953-09-18	<u>1954-09-07</u>
1954-09-08	<u>1956-10-16</u>	1958-10-11	1958-10-12	<u>1959-09-27</u>	1959-09-28
<u>1961-09-08</u>	<u>1962-09-08</u>	<u>1964-10-01</u>	<u>1964-10-02</u>	1970-09-08	<u>1970-09-16</u>
<u>1972-11-18</u>	1975-09-07	<u>1975-09-08</u>	<u>1975-09-09</u>	1979-09-19	<u>1979-09-20</u>
<u>1982-09-21</u>	1982-09-22	1982-09-30	1987-09-01	1987-09-02	<u>1990-10-01</u>
1990-10-02	1990-10-04	<u>1991-09-12</u>			
1992-09-09	1993-10-18	<u>1997-09-14</u>	<u>1997-09-15</u>	1999-09-07	1999-09-26
2002-10-31	2005-10-20	<u>2005-10-23</u>	<u>2007-09-17</u>	<u>2007-09-18</u>	2010-09-17
<u>2010-09-18</u>	2011-09-05	2012-09-09	2013-10-14	2014-09-22	2015-09-06
<u>2015-09-07</u>	2017-09-01	<u>2018-09-09</u>	2019-09-19	<u>2020-09-20</u>	<u>2020-09-21</u>
<u>2020-09-22</u>	<u>2021-09-02</u>	<u>2021-09-03</u>	2021-09-18	2022-09-08	2022-09-09

Table 4.1: 75 best analogs corresponding to the smallest 1% of Euclidean distances in the dataset. Analogs in the counterfactual world are coloured in light blue, while those in the factual world are shaded in orange. The dates underlined fall within the first 37 best analogues, namely the smallest 0.5% of Euclidean distances.

peculiarity of this period, typically characterized by very warm SST in the Mediterranean which are not found in other seasons. In order to have a fairer comparison between different months, we removed the seasonal cycle signal by subtracting the average of Z500 for each day of the year. Within this dataset, we extract the best 75 analogs, corresponding to the smallest 1% of Euclidean distance from the map defining the event (Tab. 4.1).

In Fig. 4.2a the monthly distribution of the analogs is shown. We see that the vast majority of analogs occur in September (56 out of 75), with only one in November. This

	time period	# analogs	# analogs in September	# analogs in October	# analogs in November
counter-factual	1944-1970	30	20	10	0
factual	1992-2022	30	25	5	0
total			45	15	0

Table 4.2: Counterfactual and factual climates: period covered, number of analogs, number of analogs per month.

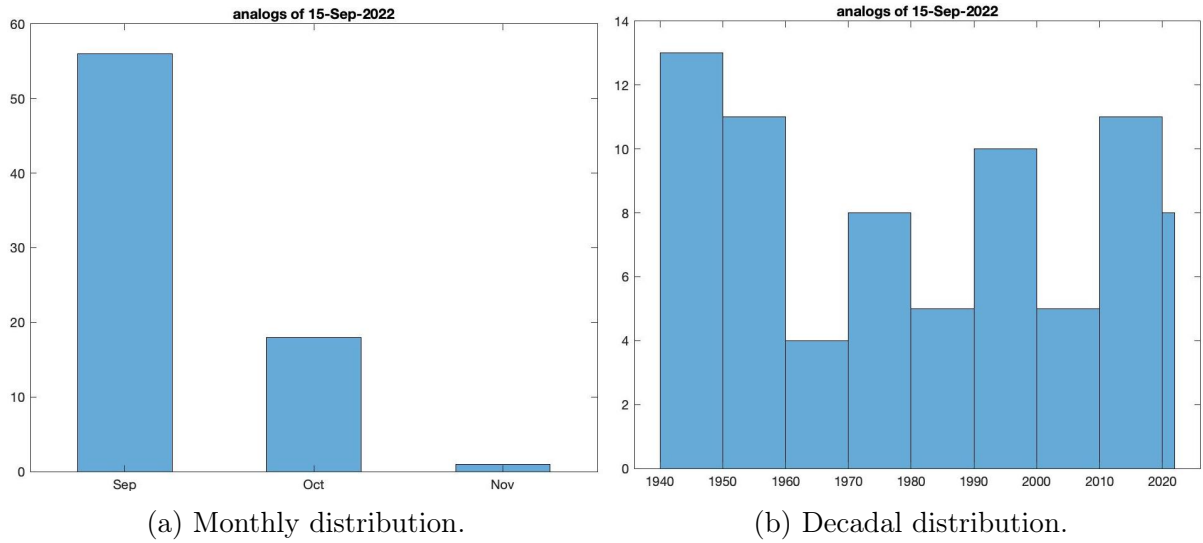


Figure 4.2: Time distributions of the 75 best analogs.

means that the synoptic conditions that led to the event are typical of late summer/early fall. In future work we will expand the analog analyses to all months to make a more precise assessment of this point.

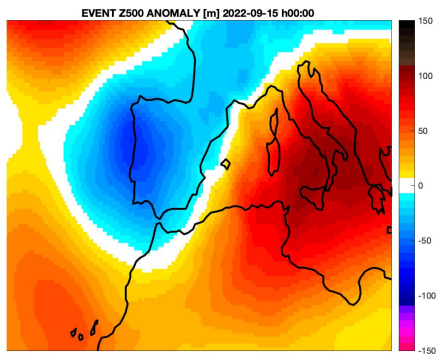
A relevant question we aim to answer now is: has the type of atmospheric circulation leading to the Marche HPE become more frequent recently? To answer this question, we show the distribution of circulation analogs per decade in Fig. 4.2b, where we see that circulation patterns like that which led to the 15th September Marche flooding are found in all decades since 1940. We further note no increase in its frequency over time. To objectively test that, we estimate the trend through a linear fit performed on the number of analogs per decade (excluding last bin in Fig. 4.2b). We found a trend of (-0.035 ± 0.055) decade⁻¹, that is, the trend is statistically insignificant and hence it is consistent with zero. This further confirms the lack of trend over time evident from the visual inspection of Fig. 4.2b. This is a first important result of the research, as it demonstrates that ACC has not yet made these kind of circulation more or less likely, although we cannot exclude that in the next decades at higher levels of global warming [42].

4.3 Circulation analogs in the factual and counterfactual climates

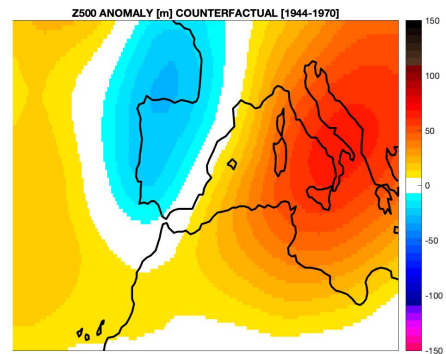
For the analysis on the Marche HPE, we define the counterfactual climate as that occurred in 1944-1970, while the factual as that occurred in 1992-2022. This choice is motivated by the fact that of the overall 75 analogs found in the search, the earliest 30 are within the counterfactual climate, and the most recent 30 are within the factual one. We, therefore, assume that the historical period 1944-1970 is less affected by ACC and that the period 1992-2022 is representative of current climate conditions. Tab. 4.1 shows the analogs in the factual (counterfactual) world highlighted in light blue (orange).

The composite of the Z500 anomaly of analogs from both periods is shown in Fig. 4.3, along with the difference between the factual (Fig. 4.3c) and the counterfactual (Fig. 4.3b) maps. The positive Z500 anomaly centered over Italy has expanded southwards in the factual world, while the negative anomaly over Iberia is shallower than in the counterfactual, as also shown in Fig. 4.3d. As these fields represent the Z500 seasonal anomaly, it is not immediately clear how the Z500 patterns have changed over time. To assess this evolution, we take the Z500 averages for September and October separately and we sum them, giving September the weight of 0.75 since 75% of analogs occur in that month (Tab. 4.2), and October the weight of 0.25. We then add such weighted average to the factual and counterfactual Z500 anomalies (Fig. 4.4). We can see that the meridional gradient is strengthened over Italy in the factual world, as confirmed by the factual-counterfactual differences map (Fig. 4.3d).

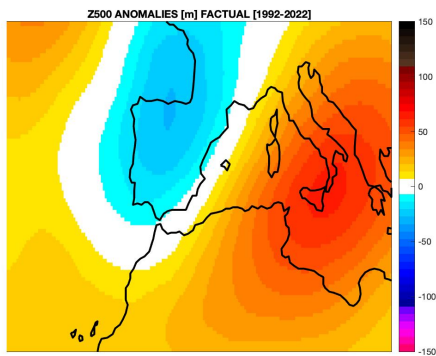
To assess if the differences between the two sets of circulation analogs (Fig. 4.3d) are statistically significant, we perform a bootstrap test as in Faranda *et al.* (2022) [25]. The bootstrap test is performed as follows: first we put together the 30 analogs from the factual climate and the 30 analogs from the counterfactual climate and we randomly extract two sets of 30 analogs. We average and subtract the two sets, creating the corresponding difference maps. We repeat this procedure 1000 times. For every grid point, we obtain a distribution of 1000 distances and we extract the mean and the standard deviation. We then consider the true difference map between factual and counterfactual climates and we mark as significant grid points where differences are more than 1.5 standard deviations above or below the mean of the bootstrap sample.



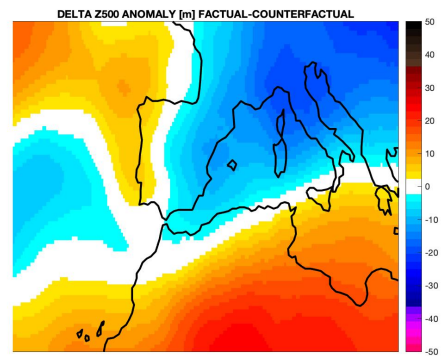
(a) Z500 anomalies for the event.



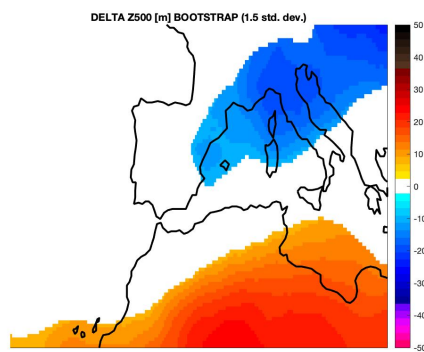
(b) Average of Z500 anomalies for counterfactual world.



(c) Average of Z500 anomalies for the 30 analogs of the factual world.

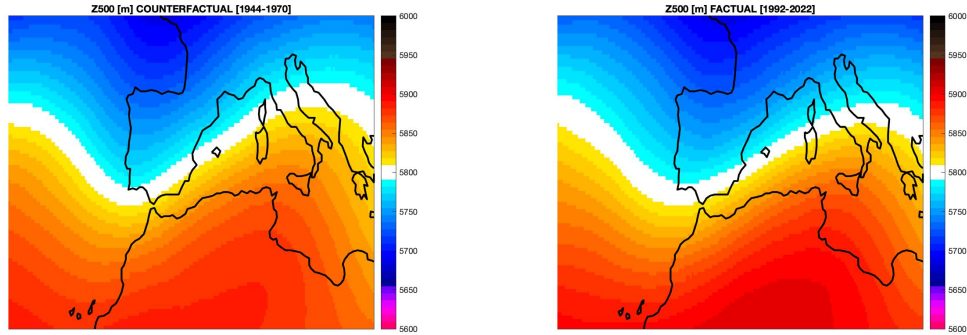


(d) Delta Z500 anomalies between factual and counterfactual periods.



(e) Areas (coloured) where the differences shown in (d) are statistically significant following a bootstrap test.

Figure 4.3: Analysis of circulation analogs in the factual and counterfactual worlds.



(a) Counterfactual world.

(b) Factual world.

Figure 4.4: Shifts in Z500 patterns between the two periods. The average of Z500 for September and October was weighted on the total number of analogs in each month and added to 4.3b and 4.3c.

The result of the bootstrap test is shown in Fig. 4.3e. We observe significant shifts in the spatial pattern of the analogs, meaning that we can identify a dynamical change of the circulation in the factual climate with respect to the counterfactual. Specifically, we see that the meridional gradient of Z500 is strengthened over the Mediterranean area. Such circulation change supports stronger southwesterly flows over the Mediterranean that can advect more humidity from the Atlantic Ocean and from western Mediterranean. Therefore, Central Italy appears to be a more favourable location for HPEs in the factual climate.

4.4 Precipitation and thermodynamic environment

Here we extend our analysis to precipitation and some other variables related to the thermodynamic environment of the identified circulation analogs:

1. precipitation, accumulated during 24 hours after 0000 UTC
2. PW at 0000 UTC
3. CAPE at 0000 UTC

As already done, we look at composites of these variables over the circulation analogs for both the counterfactual and factual climates. We further show differences between

the two worlds to assess significant shifts. We analyse PW and CAPE in addition to precipitation because, as we saw in Section 3.3.3, they are key variables of the thermodynamic environment in which the HPE developed. Moreover, atmospheric models simulate these variables better than precipitation and are therefore more reliable. Models are poor at reproducing processes of rainfall formation [82], and this results for example in the persistent underestimation of heavy rain [80].

4.4.1 Precipitation

In Fig. 4.5 we show the analysis of precipitation associated with the analogs in factual and counterfactual climates. We can appreciate a shift in the precipitation pattern. Specifically, an increase up to 6 mm/day is recorded over Italy, while the most significant increases occur over north-eastern Spain and the Istrian peninsula (Fig. 4.5d). However, the result of the bootstrap test indicates that shifts over Italy are not statistically significant, with the exception of certain areas of central Italy (Fig. 4.5e). Central Italy is not highlighted as an area with a marked increase in precipitation associated with the circulation of the event. This can be because, in the set of analogs, some show a precipitation pattern similar to that of the Marche flood, but others are quite different (Fig. 4.6).

We now want to see whether taking fewer and better analogs shows a significant shift in central Italy. That is, we want to understand if in the case of precipitation, it is better to be more stringent in the search for circulation analogues. We then perform the same analysis by taking the best 37 analogs (underlined in Tab. 4.1), corresponding to the smallest 0.5% of Euclidean distance from the map defining the event. Within this smaller set of analogs, we decide to represent the factual and counterfactual worlds keeping the same periods as in the previous analysis. Therefore, we take the 17 analogs between 1944 and 1970 to represent the counterfactual world and the 13 analogs between 1992 and 2022 to represent the factual.

The average precipitation in the two periods and their difference is shown in Fig. 4.7: in this case, we better identify an area in central Italy with increased precipitation, up to 9 mm/day. The bootstrap test carried out on the smaller set of analogs does not, however, identify Italy as an area of significant change (Fig. 4.7d). We must bear in mind that taking a smaller number of analogues leads to a decrease in significance and

we must take the statistical test carefully.

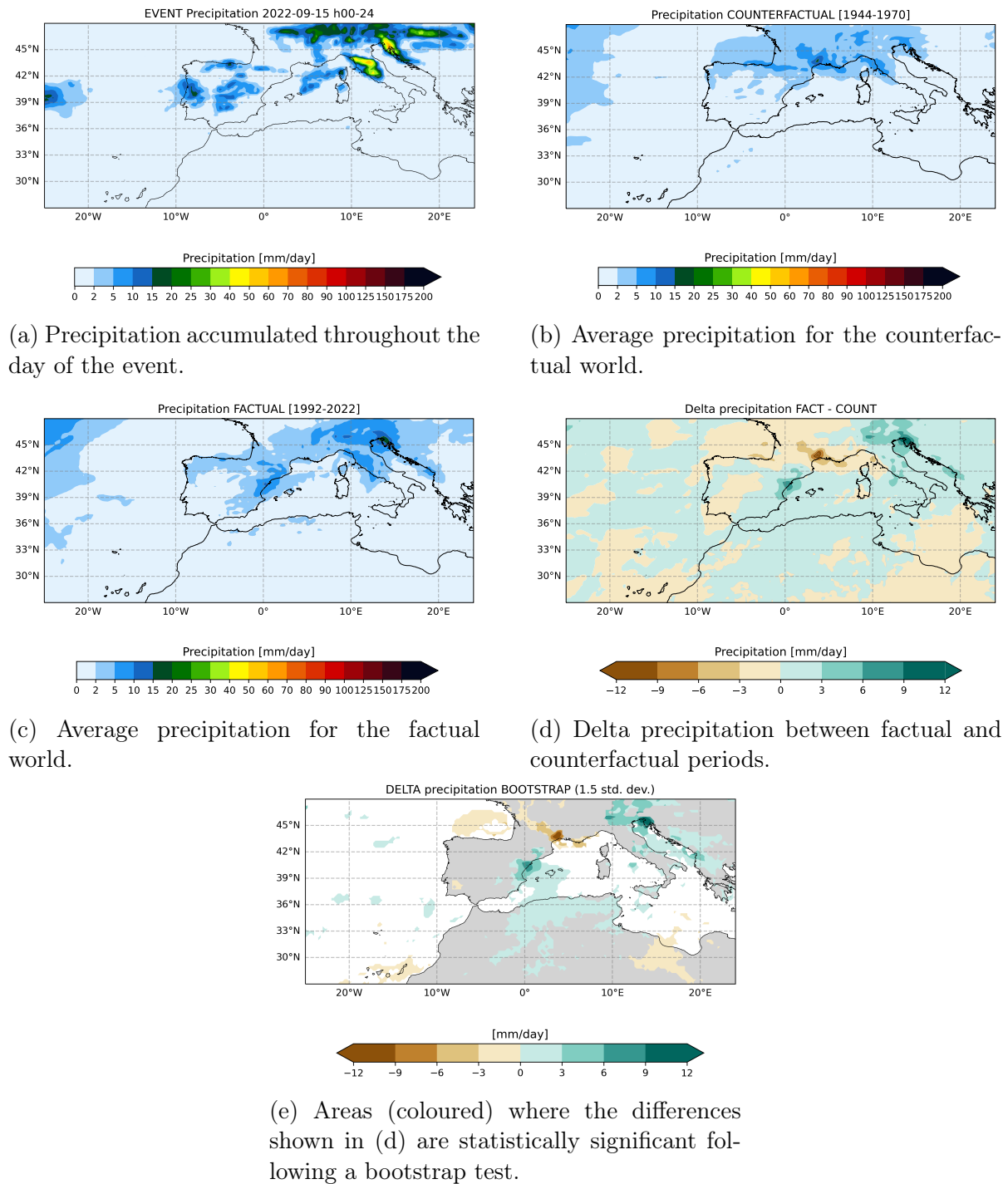
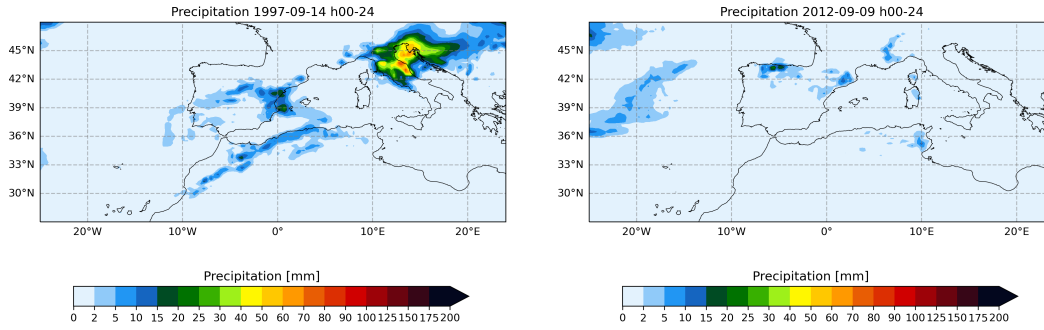


Figure 4.5: Analysis of precipitation in the factual and counterfactual worlds.



(a) Analog occurred on 14 September 1997. (b) Analog occurred on 9 September 2012.

Figure 4.6: Examples of the precipitation associated with the analogs: the pattern in (a) is similar to the one of the event, the one in (b) does not exhibit precipitation in central Italy.

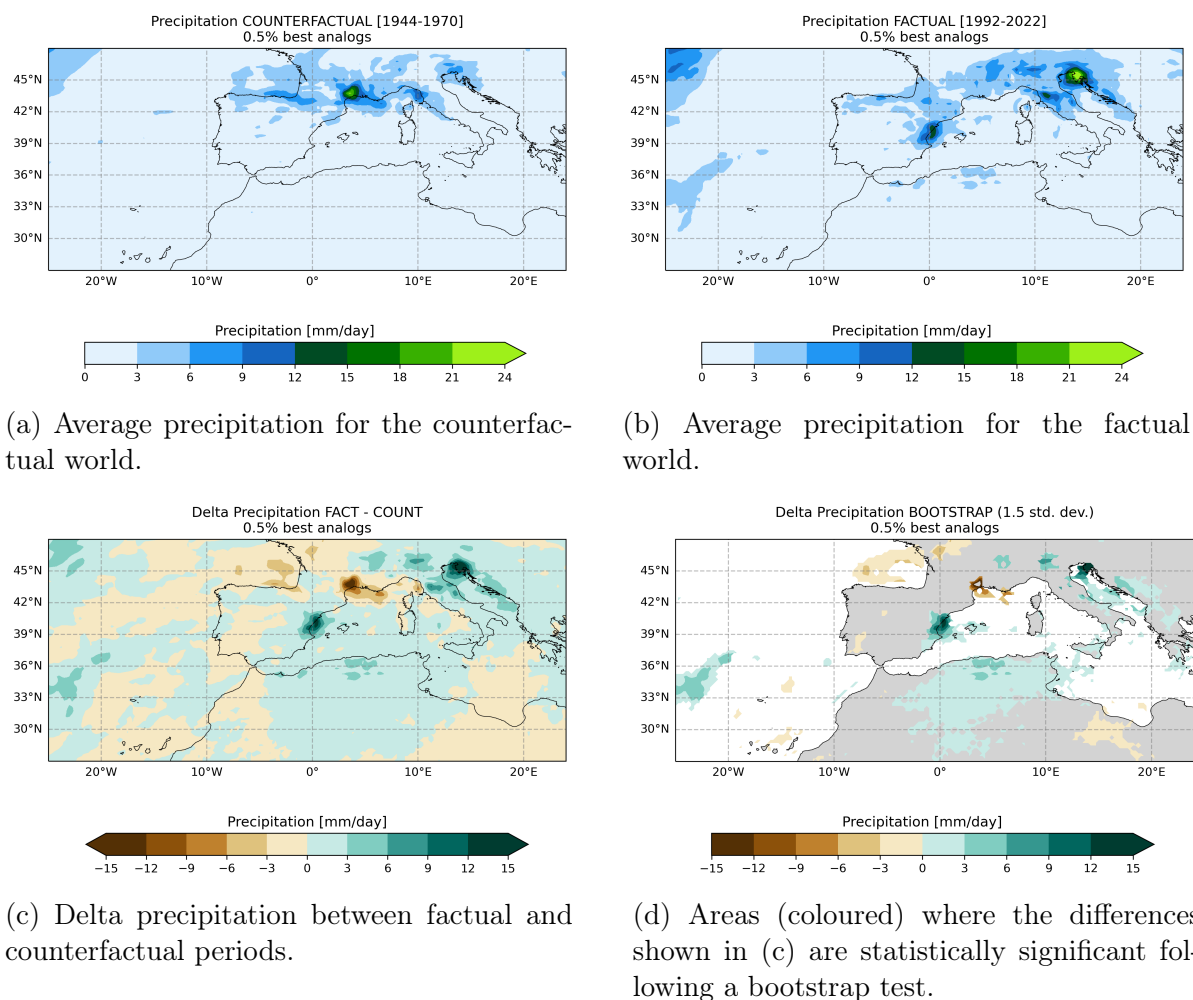
Moreover, we are basing our analysis on ERA5, which, as we saw in Section 3.2, does not capture the details of the event.

We can conclude that both precipitation analyses indicate a general increase in precipitation over the western Mediterranean and Italy, although this is not clearly delineated in the statistical test.

4.4.2 Precipitable Water and CAPE

PW and CAPE are two important indicators for intense, extreme convective events [19, 51, 48]. Specifically, high values of PW indicate a large amount of available moisture and, high values of CAPE, a great potential for strong updrafts in convective storms. Indeed, the Marche HPE was characterized by particularly high values of both PW and CAPE (Section 3.3.3). Overall, large scale atmospheric models and global climate models tend to simulate those two variables better than they do for precipitation. In order to investigate the relationship between large scale circulation and severe convective events, it is therefore sensible to evaluate if circulation states similar to that of the event also feature high values PW and CAPE. Furthermore, we also want to examine if significant changes in these two variables exists between the factual and counterfactual climates, thus highlighting a potential role of the anthropogenic global warming in setting more intense events.

We start by comparing PW and CAPE statistical distributions for all autumn days



(a) Average precipitation for the counterfactual world.

(b) Average precipitation for the factual world.

(c) Delta precipitation between factual and counterfactual periods.

(d) Areas (coloured) where the differences shown in (c) are statistically significant following a bootstrap test.

Figure 4.7: Analysis of precipitation in the factual and counterfactual worlds within the 37 best analogues.

(September - November) from 1940 to 2022 with that estimated during analog days (Fig. 4.8). We surface average them over the domain with boundaries 2°E - 16°E, 33°N - 45°N (square in Fig. 4.8a), which is the region where we find the highest values of PW and CAPE on the day of the event. Comparison between all days and analog days during September-November clearly shows an upward shift of the distributions of PW and CAPE towards higher values. This implies that flow-analogs of the Marche HPE are associated with PW and CAPE values higher than the average for autumn days. That demonstrates the relationship between large scale flow and convective events over Central Italy and it has interesting implications for predicting similar events days in

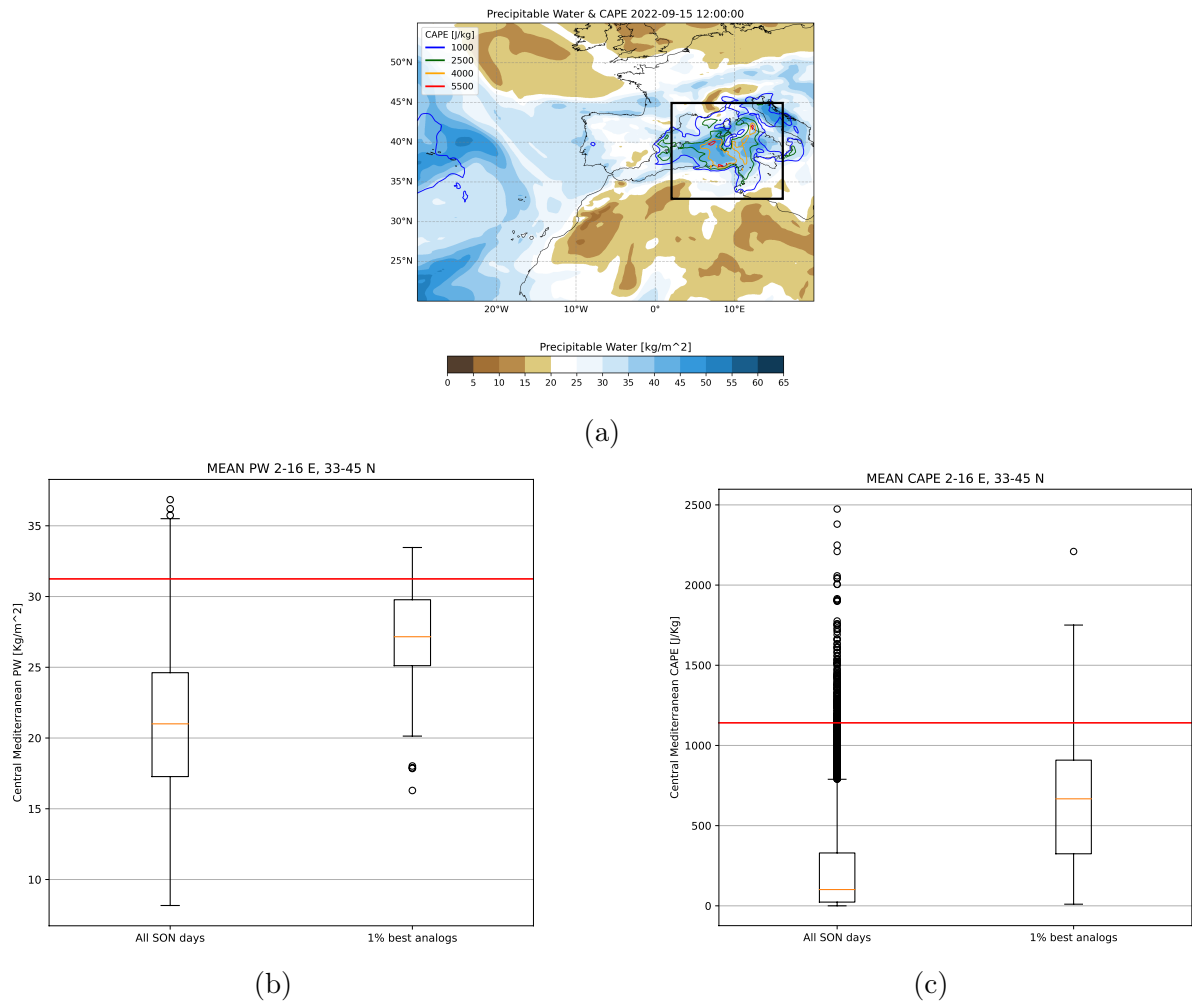


Figure 4.8: Box and whisker plots of mean (b) PW and (c) mean CAPE over the black rectangle domain (in (a): 2°E - 16°E, 33°N - 45°N) for all autumn days (September-November) from 1940 to 2022 and for the 1% best analogs. The box extends from the first quartile to the third quartile of the data, with a line at the median. The whiskers extend from the box by 1.5 times the interquartile range. Circles represent fliers points. The long red horizontal line represents the observed value for the Marche HPE.

advance.

We then analyze PW and CAPE associated with the analogs in factual and counterfactual climates (Fig. 4.9). Fig. 4.9d shows the differences between the two periods and highlights a substantial increase in both quantities. Specifically, PW shows an increase of more than 2 Kg m⁻² over the Mediterranean, with a band heading towards central

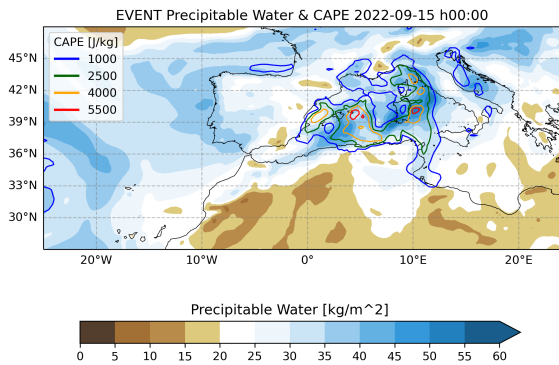
Italy where the increase is up to 6 Kg m^{-2} . This core band, together with Italy and much of the Mediterranean, is statistically significant, as we can see from the result of the bootstrap test in Fig. 4.9e. Differences in CAPE are greater than 300 J Kg^{-1} virtually all over the Mediterranean and reach 1200 J Kg^{-1} between Tunisia and Sicily. Over almost the entire area of Italy and the central Mediterranean, the increase in CAPE is statistically significant (Fig. 4.9f).

Considering that typical CAPE values in thunderstorm environments over the Mediterranean region are typically between 1000 and 2000 J Kg^{-1} [13, 50], these differences appear to be very substantial. These results indicate that PW and CAPE associated with the circulation state of the Marche flood are substantially grown in the factual climate compared to the counterfactual climate, resulting in a more favourable environment for severe convective storms in the present climate during large scale circulation conditions analog to those of the Marche event. This increase is consistent with the impact of global warming on PW and CAPE. As far as PW is concerned, we expect PW to increase with ACC, as a warmer atmosphere can hold more water vapour following the Clausius-Clapeyron law (see 1.2). Increases in CAPE with global warming are also expected worldwide and projected by climate models. This is due to increased low-level specific humidity that results in more latent heating and buoyancy for air parcels above the level of free convection [9].

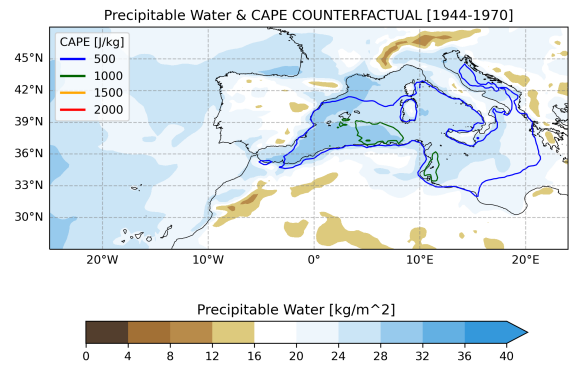
4.5 Summary and results of the analog based analysis

In summary, our analog based analysis of the Marche HPE has highlighted several important results. First, we found that the frequency of occurrence of atmospheric circulation patterns similar to that of the event has not increased with time since the 1940s. Such kinds of circulations - which are characteristics of late summer/early fall - are found in all decades without any significant trend. We then studied the differences of the Z500 pattern between factual and counterfactual climates to highlight dynamical changes in the circulation state. We found that the Z500 meridional gradient over the Mediterranean area is strengthened, resulting in a stronger southwesterly flow able to advect more moisture. Afterwards, we focused on precipitation and we found a general increase in this variable in the factual climate over the western Mediterranean and Italy. Such results must be handled with care because, as we discussed before, ERA5 is not able to

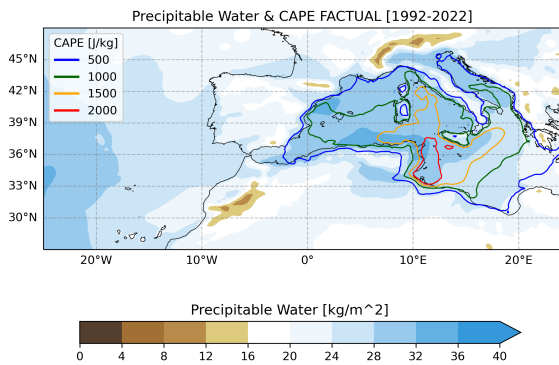
realistically capture the details of the precipitation associated with the event. This is why we decide to add the analysis of PW and CAPE, that refer to the thermodynamic environment and are more reliably simulated by large scale atmospheric models. We found that both PW and CAPE significantly increase in the factual climate over the Mediterranean Sea. These changes, along with the changes in the shape of the low-high pressure pair, suggest that moist convection and severe rainstorms have become more intense over Central Italy in the last decades during late summer/early autumn synoptic conditions as those observed during the Marche HPE.



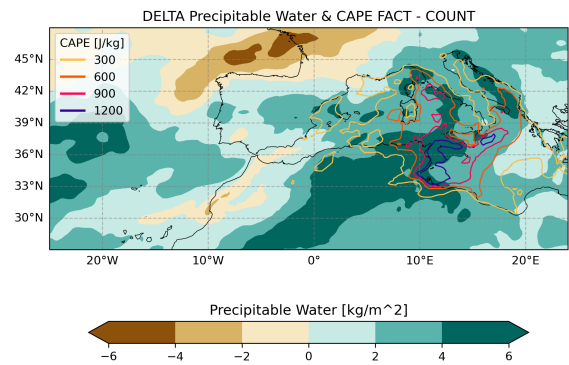
(a) PW and CAPE at 0000 UTC on the day of the event.



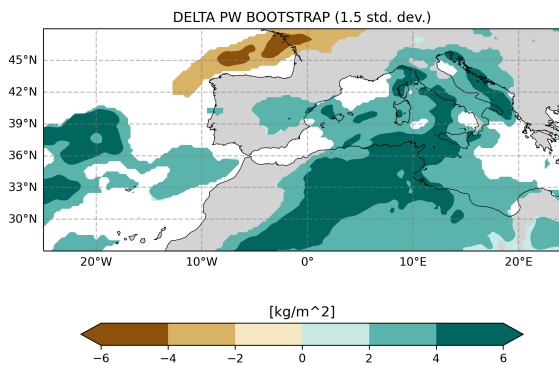
(b) Average PW and CAPE for the counterfactual world.



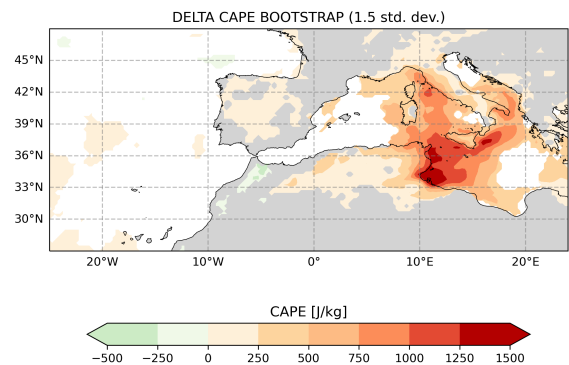
(c) Average PW and CAPE for the factual world.



(d) Delta PW and CAPE between factual and counterfactual periods.



(e) Areas (coloured) where the PW differences shown in (d) are statistically significant following a bootstrap test.



(f) Areas (coloured) where the CAPE differences shown in (d) are statistically significant following a bootstrap test.

Figure 4.9: Analysis of PW and CAPE in the factual and counterfactual worlds. Note that figure (b) and (c) do not have the same color code as (a), because the event has much higher PW and CAPE values.

Chapter 5

Conclusions and final remarks

In the present study, we examined the atmospheric circulation pattern leading to the 15th September 2022 Marche HPE, which caused the death of thirteen people and over two billion euros in damages. The event had an intensity unprecedented in the observational records: over most of northern Marche, precipitation recorded by the regional rain gauge network was between 70 and 150 mm in only 9 hours, with peaks exceeding 375 mm. Such values are well above the average accumulated precipitation for the entire month of September in the Marche region, that ranges between 60 and 100 mm. The Italian Civil Protection Department estimated that the probability of occurrence of an event of such intensity is 0.1% in any one year, which highlights the rarity of the HPE.

In the first part of the work, we performed a detailed analysis of the event. We assessed the capability of the ERA5 reanalyses to capture the HPE comparing it with the IMERG observational dataset. We found that ERA5 identifies an intense rainfall event in Central Italy but underestimates the maximum precipitation. Furthermore, it does not precisely localize it over the Marche region and misses several details of the precipitation pattern. The reasons why ERA5 does not capture the event in detail are, for example, errors in the representation of convection - which is parameterized in large scale atmospheric models - and of orography, given the still relatively low (~ 30 km) spatial resolution [4]. In the study of the large scale drivers of the event, we identified the moist southwesterly flux associated with the cyclonic circulation over Iberia as the key dynamic factor that provided moisture to the convective system. This flux persisted over central Italy for the entire duration of the event, with a vertical extension from the

surface to the mid-troposphere. A secondary contribution of moisture was provided by the superficial southerly flow associated with the shallow anticyclonic circulation centered over the Ionian sea.

The Tyrrhenian Sea is outlined as the critical area in triggering the event: here the interaction between superficial wind components resulted in an area of enhanced surface convergence that initiated and maintained convection. The spatial resolution of ERA5 does not allow us to fully understand why the most affected area was the Marche region and not, for example, on the Tyrrhenian side, which remains and open, interesting question to answer. Small-scale (i.e., $\sim O(1\text{ km})$) factors like orography and soil conditions were likely decisive in this respect. Interestingly, recent research on the response of orographic precipitation extremes to global warming shows that there are higher fractional changes in rainfall extremes on the leeward slope of the mountain as compared to the windward slope [77, 78]. Further analysis and sensitivity studies with higher resolution regional climate models with resolved convection [68] would then be required for a better understanding of the event.

We then analyzed the thermodynamic environment in which the HPE developed. Specifically, we identify PW and CAPE as the key proxy variables for the intense convection over central Italy. PW was very abundant in the western Mediterranean, with values well above the seasonal average. Specifically, it was particularly high (up to 50 Kg m^{-2}) on an elongated structure stretching from northern Morocco to central Italy. CAPE was bigger than 1000 J Kg^{-1} over Italy and the western Mediterranean, thus characterising an unstable atmosphere conducive to the intense convection. It reached the extreme value of 5500 J Kg^{-1} on the Tyrrhenian Sea, in the same region where PW reached its maximum. These conditions, added to marked positive SST anomalies (up to 4.5°C), ensured a favorable environment for the development of a mesoscale convective system over central Italy.

Enlarging the domain of the analysis over the whole Northern Hemisphere, we found that the deformation of the low - high pressure pair responsible of the sustained southwesterly moisture flux into Central Italy was determined by the arrival of a planetary Rossby wave train. This is relevant for the predictability of the event, as often high impact weather events over Europe are triggered by Rossby wave packets [88].

The second part of the study was devoted to the investigation of the role of anthropogenic climate change in the Marche HPE. We used the method of the circulation

analogues for extreme events attribution and we identified the best 75 flow-analogues of the event circulation. In other words, we selected the most similar 75 atmospheric circulation patterns to the one of the event within autumn months (Sept-Nov) in the western Mediterranean domain. We found that such circulation pattern was typical of late summer/ early fall and that it has not become more likely in recent times. A clear tendency to have very large values of CAPE and PW over Italy when the large scale circulation over the western Mediterranean is analogous to that observed on September 15 2022 was documented, thus demonstrating how the large scale conditions are precondition the occurrence of HPE over Central Italy. We then chose to take the earliest 30 analogues to define the counterfactual climate and the 30 most recent analogues to define the factual. This means that the counterfactual is represented by the historical period 1944-1970, while the factual by the recent period 1992-2022. We looked at composites of the key atmospheric variables of the event over the circulation analogues for both the counterfactual and factual climates, and we assessed whether there have been significant shifts. With regard to the spatial pattern of Z500, a significant strengthening of the meridional gradient over the Mediterranean was found in the factual climate relative to the counterfactual climate. Such dynamical change strengthens the southwesterly flow towards central Italy and its capability to advect moisture. The precipitation fields associated with flow-analogues exhibit great variability and only in certain cases are representative of HPEs over central Italy. We observe a general increase in precipitation (up to 6 mm/-day) over Italy in the factual world. However, this result should be taken with caution because of the limitation of ERA5 in representing precipitation. A direct comparison of PW and CAPE for the two time periods revealed a significant increase in both over the central and western Mediterranean basin during analogue days. This is in line with the increase in PW and CAPE we expect as a thermodynamical consequence - namely the larger capacity of the atmosphere to hold water vapour as a consequence of the Clausius-Clapeyron relationship - of global warming (Section 1.2).

In summary, the analogues methodology applied to the Marche HPE highlighted significant dynamic and thermodynamic changes favouring the occurrence of HPEs in central Italy in the factual climate with respect to the counterfactual. Such results are a first step toward an attribution study of the event. To complete the attribution to ACC, the methodology requires an assessment of whether and to what extent the inter-decadal variability (associated, for example, with the El Niño-Southern Oscillation or the Atlantic

Multidecadal Variability) can explain the shifts in the analogs characteristics. This can be achieved by following the procedure outlined in Faranda *et al.* (2022) [25], who exploit time series of indices characterising the two phenomena. Future developments of this work could include further sensitivity tests of the analog methodology applied to our case study in order to verify the robustness of the results here discussed. For example, it would be interesting to define the event in terms of SLP instead of Z500 to check if there are significant differences in the results. Another thing to do would be to extend the analysis to all-year months rather than just late summer/early fall and look for analogs throughout the year and not just in the autumn months. Finally, it would be worth detecting flow-analogs within another reanalysis datasets. This would allow us to have a longer time extension - as an example, the NOAA-CIRES-DOE Twentieth Century Reanalysis, version 3, spans an almost two century-long time period (1836 to 2015) [79] - and thus to have a better and cleaner definition of counterfactual and factual climate. A longer time period would also allow for a more numerous set of analogs, and thus for the possibility to use lower percentiles (and so, more similar analogs) and hence to have analogs more similar to the observed state. Finally, the use of different reanalysis products would be important to test the sensitivity of the results to different datasets.

Acknowledgements

I wish to thank Dr. Salvatore Pascale for advising and supporting me in this work. I also thank him for the essential help he gave me in the application to the MedCyclones Cost Action that allowed me to visit LSCE in Paris, France. This Master's thesis work has been a wonderful experience and has encouraged me to pursue the study of extreme events in a PhD programme.

I want to acknowledge Dr. Davide Faranda for welcoming me to LSCE and for guiding me through the analogs methodology. I also thank him for providing me with his code to search circulation analogs, which was fundamental in investigating the impact of climate change on the Marche flood. I look forward to working with you in the ESTIMR team.

Finally, I would like to thank Dr. Paolo Ruggieri for helping me with the choice of my Master's thesis work and for introducing me to Python coding for climate data analysis.

Bibliography

- [1] Agenzia Giornalistica Italia. L'alluvione nelle marche ha fatto due miliardi di danni. 2022-09-20. URL: <https://www.agi.it/cronaca/news/2022-09-20/alluvione-marche-due-miliardi-danni-18141731/>.
- [2] ASSAM - servizio agrometeo regionale. URL: <http://www.meteo.marche.it/cartetematiche.aspx>.
- [3] F. Boccanera, F. Iocca, M. Lazzeri, S. Sofia, V. Giordano, F. Sini, G. Speranza, and M. Tedeschini. Rapporto di evento preliminare: Maltempo 15, 16 e 17 settembre 2022. 2022-09-22. URL: <https://www.regione.marche.it/Regione-Utile/Protezione-Civile/Progetti-e-Pubblicazioni/Rapporti-di-evento>.
- [4] M. G. Bosilovich, J. Chen, F. R. Robertson, and R. F. Adler. Evaluation of Global Precipitation in Reanalyses. Journal of Applied Meteorology and Climatology, 47(9):2279–2299, 2008. doi:<https://doi.org/10.1175/2008JAMC1921.1>.
- [5] J. Brunner, S. Ackerman, A. Bachmeier, and R. Rabin. A quantitative analysis of the enhanced-v feature in relation to severe weather. Weather and Forecasting - WEATHER FORECAST, 22, 2007. doi:[10.1175/WAF1022.1](https://doi.org/10.1175/WAF1022.1).
- [6] J. Cattiaux, R. Vautard, C. Cassou, P. Yiou, V. Masson-Delmotte, and F. Codron. Winter 2010 in europe: A cold extreme in a warming climate. Geophysical Research Letters, 37(20), 2010. doi:<https://doi.org/10.1029/2010GL044613>.
- [7] C. F. Chappell. Quasi-Stationary Convective Events, pages 289–310. American Meteorological Society, Boston, MA, 1986. doi:[10.1007/978-1-935704-20-1_13](https://doi.org/10.1007/978-1-935704-20-1_13).
- [8] D. Chen, M. Rojas, B. Samset, K. Cobb, A. Diongue Niang, P. Edwards, S. Emori, S. Faria, E. Hawkins, P. Hope, P. Huybrechts, M. Meinshausen, S. Mustafa, G.-K. Plattner, and A.-M. Tréguier. Framing, Context, and Methods, page 147–286. Cambridge University Press, Cambridge, United Kingdom and New York, NY, USA, 2021. doi:[10.1017/9781009157896.003](https://doi.org/10.1017/9781009157896.003).

- [9] J. Chen, A. Dai, Y. Zhang, and K. L. Rasmussen. Changes in convective available potential energy and convective inhibition under global warming. *Journal of Climate*, 33(6):2025 – 2050, 2020. doi:<https://doi.org/10.1175/JCLI-D-19-0461.1>.
- [10] N. Christidis, G. S. Jones, and P. A. Stott. Dramatically increasing chance of extremely hot summers since the 2003 european heatwave. *Nature Climate Change*, 5:46–50, 2015. doi:[10.1038/nclimate2468](https://doi.org/10.1038/nclimate2468).
- [11] G. P. Compo, J. S. Whitaker, P. D. Sardeshmukh, N. Matsui, R. J. Allan, X. Yin, B. E. Gleason, R. S. Vose, G. Rutledge, P. Bessemoulin, S. Brönnimann, M. Brunet, R. I. Crouthamel, A. N. Grant, P. Y. Groisman, P. D. Jones, M. C. Kruk, A. C. Kruger, G. J. Marshall, M. Maugeri, H. Y. Mok, Nordli, T. F. Ross, R. M. Trigo, X. L. Wang, S. D. Woodruff, and S. J. Worley. The Twentieth Century Reanalysis Project. *Quarterly Journal of the Royal Meteorological Society*, 137(654):1–28, 2011. doi:<https://doi.org/10.1002/qj.776>.
- [12] Copernicus Climate Change Service (C3S) Climate Data Store (CDS). [ERA5 hourly data on pressure levels from 1940 to present](https://cds.clm.copernicus.com/cds/#?dataset=era5-hourly-1940-present). doi:[10.24381/cds.bd0915c6](https://doi.org/10.24381/cds.bd0915c6).
- [13] Copernicus Climate Change Service (C3S) Climate Data Store (CDS). [ERA5 hourly data on single levels from 1940 to present](https://cds.clm.copernicus.com/cds/#?dataset=era5-hourly-single-levels-1940-present). doi:[10.24381/cds.adbb2d47](https://doi.org/10.24381/cds.adbb2d47).
- [14] Copernicus Climate Change Service, Climate Data Store. [Complete UERRA regional reanalysis for Europe from 1961 to 2019](https://cds.clm.copernicus.com/cds/#?dataset=era5-land-1961-2019). doi:[10.24381/cds.dd7c6d66](https://doi.org/10.24381/cds.dd7c6d66).
- [15] Corriere della Sera. L’alluvione vista dall’alto: le campagne attorno a senigallia sono un mare di fango. URL: <https://video.corriere.it/cronaca/alluvione-vista-alto-campagne-attorno-senigallia-sono-mare-fango/43a0eb74-35a6-11ed-a61e-565e99394797>.
- [16] S. Davolio, S. D. Fera, S. Laviola, M. M. Miglietta, and V. Levizzani. Heavy precipitation over italy from the mediterranean storm “vaia” in october 2018: Assessing the role of an atmospheric river. *Monthly Weather Review*, 148(9):3571 – 3588, 2020. doi:<https://doi.org/10.1175/MWR-D-20-0021.1>.
- [17] S. Davolio, M. Vercellino, M. M. Miglietta, L. Drago Pitura, S. Laviola, and V. Levizzani. The influence of an atmospheric river on a heavy precipitation event over the western alps. *Weather and Climate Extremes*, 39:100542, 2023. doi:<https://doi.org/10.1016/j.wace.2022.100542>.
- [18] R. Dole, M. Hoerling, J. Perlwitz, J. Eischeid, P. Pegion, T. Zhang, X.-W. Quan, T. Xu, and D. Murray. Was there a basis for anticipating the 2010 russian heat wave? *Geophysical Research Letters*, 38(6), 2011. doi:<https://doi.org/10.1029/2010GL046582>.

- [19] W. Dong, Y. Lin, J. Wright, Y. Xie, X. Yin, and J. Guo. Precipitable water and CAPE dependence of rainfall intensities in China. *Clim. Dyn.*, 52:3357–3368, 2019. doi:10.1007/s00382-018-4327-8.
- [20] ECMWF. Climate data store. URL: <https://cds.climate.copernicus.eu#!/home>.
- [21] ECMWF Reanalysis v5 (ERA5). URL: <https://www.ecmwf.int/en/forecasts/dataset/ecmwf-reanalysis-v5>.
- [22] EUMETSAT - European Organisation for the Exploitation of Meteorological Satellites. High rate seviri level 1.5 image data. URL: <https://navigator.eumetsat.int/product/EO:EUM:DAT:MSG:HRSEVIRI>.
- [23] European Commission and Joint Research Centre, A. Toreti, D. Bavera, J. Acosta Navarro, A. Jager, C. Di Ciollo, W. Maetens, D. Magni, D. Masante, M. Mazzeschi, J. Spinoni, S. Niemeyer, C. Cammalleri, and A. Hrast Essenfelder. Drought in Europe : August 2022 : GDO analytical report. Publications Office of the European Union, 2022. doi:doi/10.2760/264241.
- [24] European Commission and Joint Research Centre, A. Toreti, D. Bavera, C. Cammalleri, A. Jager, C. Di Ciollo, W. Maetens, D. Magni, D. Masante, M. Mazzeschi, N. McCormick, J. Spinoni, S. Niemeyer, G. Manfron, L. Seguini, M. Berg, M. De Felice, F. Avanzi, G. Naumann, L. Rossi, and S. Gabellani. Drought in northern Italy March 2022 : GDO analytical report. Publications Office of the European Union, 2022. doi:doi/10.2760/781876.
- [25] D. Faranda, S. Bourdin, M. Ginesta, M. Krouma, R. Noyelle, F. Pons, P. Yiou, and G. Messori. A climate-change attribution retrospective of some impactful weather extremes of 2021. *Weather and Climate Dynamics*, 3(4):1311–1340, 2022. doi:10.5194/wcd-3-1311-2022.
- [26] D. Faranda, S. Pascale, and B. Bulut. Persistent anticyclonic conditions and climate change exacerbated the exceptional 2022 european-mediterranean drought. *Environmental Research Letters*, 18(3):034030, 2023. doi:10.1088/1748-9326/acbc37.
- [27] T. T. Fujita. Overshooting thunderheads observed from ATS and Learjet. Jan 1974. URL: <https://ntrs.nasa.gov/api/citations/19740018973/downloads/19740018973.pdf>.
- [28] A. Giordani, I. M. L. Cerenzia, T. Paccagnella, and S. Di Sabatino. SPHERA, a new convection-permitting regional reanalysis over Italy: Improving the description of

- heavy rainfall. Quarterly Journal of the Royal Meteorological Society, 149(752):781–808, 2023. doi:[10.1002/qj.4428](https://doi.org/10.1002/qj.4428).
- [29] F. Grazzini, G. C. Craig, C. Keil, G. Antolini, and V. Pavan. Extreme precipitation events over northern italy. part i: A systematic classification with machine-learning techniques. Quarterly Journal of the Royal Meteorological Society, 146(726):69–85, 2020. doi:<https://doi.org/10.1002/qj.3635>.
- [30] F. Grazzini, G. Fragkoulidis, F. Teubler, V. Wirth, and G. C. Craig. Extreme precipitation events over northern italy. part ii: Dynamical precursors. Quarterly Journal of the Royal Meteorological Society, 147(735):1237–1257, 2021. doi:<https://doi.org/10.1002/qj.3969>.
- [31] D. L. Hartmann. Appendix b the clausius-clapeyron relation. In Global Physical Climatology, volume 56 of International Geophysics, pages 350–351. Academic Press, 1994. doi:[https://doi.org/10.1016/S0074-6142\(08\)60571-9](https://doi.org/10.1016/S0074-6142(08)60571-9).
- [32] M. Hauser, L. Gudmundsson, R. Orth, A. Jézéquel, K. Haustein, R. Vautard, G. J. Van Oldenborgh, L. Wilcox, and S. Seneviratne. Methods and model dependency of extreme event attribution: The 2015 european drought: 2015 european drought. Earth’s Future, 5, 2017. doi:[10.1002/2017EF000612](https://doi.org/10.1002/2017EF000612).
- [33] I. Held and B. Soden. Robust responses of the hydrological cycle to global warming. Journal of Climate, 19(21):5686–5699, 2006. doi:[10.1175/JCLI3990.1](https://doi.org/10.1175/JCLI3990.1).
- [34] H. Hersbach. Era5 reanalysis now available from 1940. URL: <https://www.ecmwf.int/en/newsletter/175/news/era5-reanalysis-now-available-1940>.
- [35] H. Hersbach, B. Bell, P. Berrisford, S. Hirahara, A. Horányi, J. Muñoz-Sabater, J. Nicolas, C. Peubey, R. Radu, D. Schepers, A. Simmons, C. Soci, S. Abdalla, X. Abellan, G. Balsamo, P. Bechtold, G. Biavati, J. Bidlot, M. Bonavita, G. De Chiara, P. Dahlgren, D. Dee, M. Diamantakis, R. Dragani, J. Flemming, R. Forbes, M. Fuentes, A. Geer, L. Haimberger, S. Healy, R. J. Hogan, E. Hólm, M. Janisková, S. Keeley, P. Laloyaux, P. Lopez, C. Lupu, G. Radnoti, P. de Rosnay, I. Rozum, F. Vamborg, S. Villaume, and J.-N. Thépaut. The era5 global reanalysis. Quarterly Journal of the Royal Meteorological Society, 146(730):1999–2049, 2020. doi:<https://doi.org/10.1002/qj.3803>.
- [36] J. R. Holton and G. J. Hakim. Chapter 7 - baroclinic development. In J. R. Holton and G. J. Hakim, editors, An Introduction to Dynamic Meteorology (Fifth Edition), pages 213–254. Academic Press, Boston, fifth edition edition, 2013. doi:<https://doi.org/10.1016/B978-0-12-384866-6.00007-6>.
- [37] E. Hovmöller. The trough-and-ridge diagram. Tellus, 1(2):62–66, 1949.

- [38] Il Gazzettino. Marche, l'alluvione vista dal satellite: le immagini dei detriti nel mare adriatico. 2022-09-18. URL: https://www.ilgazzettino.it/italia/cronaca_nera/alluvione_marche_immagini_satellite-6935627.html?refresh_ce.
- [39] IMERG - Integrated Multi-satellitE Retrievals for GPM. URL: <https://gpm.nasa.gov/data/IMERG>.
- [40] IPCC. Summary for policymakers. 2023. URL: https://report.ipcc.ch/ar6syр/pdf/IPCC_AR6_SYR_SPM.pdf.
- [41] IPCC. Annex VII: Glossary [Matthews, J.B.R., V. Möller, R. van Diemen, J.S. Fuglestvedt, V. Masson-Delmotte, C. Méndez, S. Semenov, A. Reisinger (eds.)], page 2215–2256. Cambridge University Press, Cambridge, United Kingdom and New York, NY, USA, 2021. doi:10.1017/9781009157896.022.
- [42] IPCC. Summary for Policymakers, pages 3–32. Cambridge University Press, Cambridge, United Kingdom and New York, NY, USA, 2021. doi:10.1017/9781009157896.001.
- [43] F. Isotta, C. Frei, V. Weilguni, M. Perčec Tadić, P. Lassègues, B. Rudolf, V. Pavan, C. Cacciamani, G. Antolini, S. M. Ratto, M. Munari, S. Micheletti, V. Bonati, C. Lussana, C. Ronchi, E. Panettieri, G. Marigo, and G. Vertačnik. The climate of daily precipitation in the alps: development and analysis of a high-resolution grid dataset from pan-alpine rain-gauge data. International Journal of Climatology, 34(5):1657–1675, 2014. doi:<https://doi.org/10.1002/joc.3794>.
- [44] A. Jansa, A. Genoves, M. A. Picornell, J. Campins, R. Riosalido, and O. Carretero. Western mediterranean cyclones and heavy rain. part 2: Statistical approach. Meteorological Applications, 8(1):43–56, 2001. doi:<https://doi.org/10.1017/S1350482701001049>.
- [45] A. Jézéquel, J. Cattiaux, P. Naveau, S. Radanovics, A. Ribes, R. Vautard, M. Vrac, and P. Yiou. Trends of atmospheric circulation during singular hot days in europe. Environmental Research Letters, 13(5):054007, 2018. doi:10.1088/1748-9326/aab5da.
- [46] A. Jézéquel, P. Yiou, and S. Radanovics. Role of circulation in european heatwaves using flow analogues. Climate Dynamics, 50, 2018. doi:10.1007/s00382-017-3667-0.
- [47] E. Kalnay. Atmospheric Modeling, Data Assimilation and Predictability. Cambridge University Press, 2002. doi:10.1017/CB09780511802270.

- [48] S. Kim, A. Sharma, C. Wasko, and R. Nathan. Linking Total Precipitable Water to Precipitation Extremes Globally. Earth's Future, 10(2):e2021EF002473, 2022.
- [49] D. A. Lavers, A. Simmons, F. Vamborg, and M. J. Rodwell. An evaluation of era5 precipitation for climate monitoring. Quarterly Journal of the Royal Meteorological Society, 148(748):3152–3165, 2022. doi:<https://doi.org/10.1002/qj.4351>.
- [50] K.-O. Lee, C. Flamant, V. Ducrocq, F. Duffourg, N. Fourrié, and S. Davolio. Convective initiation and maintenance processes of two back-building mesoscale convective systems leading to heavy precipitation events in southern italy during hymex iop 13. Quarterly Journal of the Royal Meteorological Society, 142(700):2623–2635, 2016. doi:<https://doi.org/10.1002/qj.2851>.
- [51] C. Lepore, D. Veneziano, and A. Molini. Temperature and CAPE dependence of rainfall extremes in the eastern United States. Geophysical Research Letters, 42:74–83, 2015.
- [52] D. Mccann. The enhanced-v: A satellite observable severe storm signature. Monthly Weather Review, 111:887–894, 1983. doi:10.1175/1520-0493(1983)111<0887:TEVASO>2.0.CO;2.
- [53] W. L. McMurdie and R. A. Houze. 8 - weather systems. In J. M. Wallace and P. V. Hobbs, editors, Atmospheric Science (Second Edition), pages 313–373. Academic Press, San Diego, second edition edition, 2006. doi:<https://doi.org/10.1016/B978-0-12-732951-2.50013-2>.
- [54] S. Melani, F. Pasi, B. Gozzini, and A. Ortolani. A four year (2007–2010) analysis of long-lasting deep convective systems in the mediterranean basin. Atmospheric Research, 123:151–166, 2013. doi:<https://doi.org/10.1016/j.atmosres.2012.09.006>.
- [55] Met Office. The heatwave of 2003. URL: <https://www.metoffice.gov.uk/weather/learn-about/weather/case-studies/heatwave>.
- [56] Met Office. The Russian heatwave of summer 2010. URL: <https://www.metoffice.gov.uk/weather/learn-about/weather/case-studies/russian-heatwave>.
- [57] Meteoweb. Allerta meteo, nel mar jonio si è formato il medicane: l'uragano mediterraneo si chiama “apollo”, grande incertezza sulla traiettoria. URL: <https://www.meteoweb.eu/2021/10/allerta-meteo-nel-mar-jonio-si-e-formato-il-medicane-uragano-mediterraneo-apollo/1734097/>.
- [58] M. M. Miglietta and S. Davolio. Dynamical forcings in heavy precipitation events over italy: lessons from the hymex sop1 campaign. Hydrology and Earth System Sciences, 26(3):627–646, 2022. doi:10.5194/hess-26-627-2022.

- [59] NASA. Imerg late run precipitation. URL: https://disc.gsfc.nasa.gov/datasets/GPM_3IMERGHHL_06/summary?keywords=%22IMERG%20late%22.
- [60] National Academies of Sciences, Engineering, and Medicine. Attribution of Extreme Weather Events in the Context of Climate Change. The National Academies Press, Washington, DC, 2016. doi:10.17226/21852.
- [61] P. A. O’Gorman. Precipitation Extremes Under Climate Change. Curr. Clim. Change Rep., 1:49–59, 2015. doi:10.1007/s40641-015-0009-3.
- [62] F. Otto. Extreme events: The art of attribution. Nature Climate Change, 6:342–343, 2016. doi:10.1038/nclimate2971.
- [63] F. Otto, P. Wolski, F. Lehner, C. Tebaldi, G. J. Van Oldenborgh, S. Hogesteeger, R. Singh, P. Holden, N. Fuckar, R. Odoulami, and M. New. Anthropogenic influence on the drivers of the Western Cape drought 2015-2017. Environmental Research Letters, 13(12):124010, 2018. doi:10.1088/1748-9326/aae9f9.
- [64] F. E. Otto. Attribution of weather and climate events. Annual Review of Environment and Resources, 42(1):627–646, 2017. doi:10.1146/annurev-environ-102016-060847.
- [65] S. Pascale, S. Kapnick, T. Delworth, and W. Cooke. Increasing risk of another Cape Town "Day Zero" drought in the 21st century. Proc Natl Acad Sci U S A., 117(47):29495–29503, 2020. doi:10.1073/pnas.2009144117.
- [66] S. Pascale, S. Kapnick, T. Delworth, H. Hidalgo, and W. Cooke. Natural variability vs forced signal in the 2015–2019 Central American drought. Climatic Change, 168:16, 2011. doi:10.1007/s10584-021-03228-4.
- [67] S. Y. Philip, S. F. Kew, G. J. van Oldenborgh, F. S. Anslow, S. I. Seneviratne, R. Vautard, D. Coumou, K. L. Ebi, J. Arrighi, R. Singh, M. van Aalst, C. Pereira Marghidan, M. Wehner, W. Yang, S. Li, D. L. Schumacher, M. Hauser, R. Bonnet, L. N. Luu, F. Lehner, N. Gillett, J. S. Tradosky, G. A. Vecchi, C. Rodell, R. B. Stull, R. Howard, and F. E. L. Otto. Rapid attribution analysis of the extraordinary heat wave on the pacific coast of the us and canada in june 2021. Earth System Dynamics, 13(4):1689–1713, 2022. doi:10.5194/esd-13-1689-2022.
- [68] A. Prein, W. Langhans, G. Fosser, A. Ferrone, N. Ban, K. Goergen, M. Keller, M. Tölle, O. Gutjahr, F. Feser, E. Brisson, S. Kollet, J. Schmidli, N. Lipzig, and R. Leung. A review on regional convection-permitting climate modeling: demonstrations, prospects, and challenges. 53(2):323–361, 2015. doi:10.1002/2014RG000475.

- [69] S. Rahmstorf and D. Coumou. Increase of extreme events in a warming world. *Proceedings of the National Academy of Sciences*, 108(44):17905–17909, 2011. doi:10.1073/pnas.1101766108.
- [70] Rai News. Le immagini di cantiano sommersa dall'acqua: "caduta la pioggia di un anno". 2022-09-16. URL: <https://www.rainews.it/video/2022/09/le-immagini-di-cantiano-sommersa-dallacqua-caduta-la-pioggia-di-un-anno-3f94ba98-c40a-44c7-96e5-a7eece410070.html>.
- [71] S. Russo, J. Sillmann, and E. M. Fischer. Top ten european heatwaves since 1950 and their occurrence in the coming decades. *Environmental Research Letters*, 10(12):124003, 2015. doi:10.1088/1748-9326/10/12/124003.
- [72] P. Salvati, C. Bianchi, M. Rossi, and F. Guzzetti. Societal landslide and flood risk in italy. *Natural Hazards and Earth System Sciences*, 10(3):465–483, 2010. doi:10.5194/nhess-10-465-2010.
- [73] N. Schaller, A. Kay, R. Lamb, N. Massey, G. J. Van Oldenborgh, F. Otto, S. Sparrow, R. Vautard, P. Yiou, I. Ashpole, A. Bowery, S. Crooks, K. Haustein, C. Huntingford, W. Ingram, R. Jones, T. Legg, J. Miller, J. Skeggs, and M. Allen. Human influence on climate in the 2014 southern england winter floods and their impacts. *Nature Climate Change*, 6:627–634, 2016. doi:10.1038/nclimate2927.
- [74] R. Seager, N. Naik, and G. A. Vecchi. Thermodynamic and Dynamic Mechanisms for Large-Scale Changes in the Hydrological Cycle in Response to Global Warming. *J. Climate*, 23:4651–4668, 2010. doi:10.1175/2010JCLI3655.1.
- [75] S. Seneviratne, X. Zhang, M. Adnan, W. Badi, C. Dereczynski, A. Di Luca, S. Ghosh, I. Iskandar, J. Kossin, S. Lewis, F. Otto, I. Pinto, M. Satoh, S. Vicente-Serrano, M. Wehner, and B. Zhou. *Weather and Climate Extreme Events in a Changing Climate*, page 1513–1766. Cambridge University Press, Cambridge, United Kingdom and New York, NY, USA, 2021. doi:10.1017/9781009157896.013.
- [76] T. Shepherd. Atmospheric circulation as a source of uncertainty in climate change projections. *Nature Geoscience*, 7:703–708, 2014. doi:10.1038/NGEO2253.
- [77] X. Shi and D. R. Durran. Estimating the Response of Extreme Precipitation over Midlatitude Mountains to Global Warming. *Journal of Climate*, 28(10):4246–4262, 2015. doi:10.1175/JCLI-D-15-0576.1.
- [78] N. Siler and G. Roe. How will orographic precipitation respond to surface warming? *Geophysical Research Letters*, 41:2606–2613, 2014. doi:10.1002/2013GL059095.

- [79] L. C. Slivinski, G. P. Compo, J. S. Whitaker, P. D. Sardeshmukh, B. S. Giese, C. McColl, R. Allan, X. Yin, R. Vose, H. Titchner, J. Kennedy, L. J. Spencer, L. Ashcroft, S. Brönnimann, M. Brunet, D. Camuffo, R. Cornes, T. A. Cram, R. Crouthamel, F. Domínguez-Castro, J. E. Freeman, J. Gergis, E. Hawkins, P. D. Jones, S. Jourdain, A. Kaplan, H. Kubota, F. L. Blancq, T.-C. Lee, A. Lorrey, J. Luterbacher, M. Maugeri, C. J. Mock, G. K. Moore, R. Przybylak, C. Pudmenzky, C. Reason, V. C. Slonosky, C. A. Smith, B. Tinz, B. Trewin, M. A. Valente, X. L. Wang, C. Wilkinson, K. Wood, and P. Wyszyński. Towards a more reliable historical reanalysis: Improvements for version 3 of the twentieth century reanalysis system. *Quarterly Journal of the Royal Meteorological Society*, 145(724):2876–2908, 2019. doi:<https://doi.org/10.1002/qj.3598>.
- [80] G. L. Stephens, T. L’Ecuyer, R. Forbes, A. Gettelmen, J.-C. Golaz, A. Bodas-Salcedo, K. Suzuki, P. Gabriel, and J. Haynes. Dreary state of precipitation in global models. *Journal of Geophysical Research: Atmospheres*, 115(D24), 2010. doi:<https://doi.org/10.1029/2010JD014532>.
- [81] P. Stott, D. Stone, and M. Allen. Human contribution to the european heatwave of 2003. *Nature*, 432:610–4, 2005. doi:[10.1038/nature03089](https://doi.org/10.1038/nature03089).
- [82] J. Tan, L. Oreopoulos, C. Jakob, and D. Jin. Evaluating rainfall errors in global climate models through cloud regimes. *Climate Dynamics*, 50:3301–3314, 2018. doi:[10.1007/s00382-017-3806-7](https://doi.org/10.1007/s00382-017-3806-7).
- [83] K. Trenberth, J. Fasullo, and T. Shepherd. Attribution of climate extreme events. *Nature Climate Change*, 5:725–730, 2015. doi:[10.1038/nclimate2657](https://doi.org/10.1038/nclimate2657).
- [84] K. van der Wiel, S. B. Kapnick, G. J. van Oldenborgh, K. Whan, S. Philip, G. A. Vecchi, R. K. Singh, J. Arrighi, and H. Cullen. Rapid attribution of the august 2016 flood-inducing extreme precipitation in south louisiana to climate change. *Hydrology and Earth System Sciences*, 21(2):897–921, 2017. doi:[10.5194/hess-21-897-2017](https://doi.org/10.5194/hess-21-897-2017).
- [85] K. Van der Wiel, N. Wanders, F. Selten, and M. Bierkens. Added value of large ensemble simulations for assessing extreme river discharge in a 2 C warmer world. *Geophysical Research Letters*, 46:2093–2102, 2019. doi:[10.1029/2019GL081967](https://doi.org/10.1029/2019GL081967).
- [86] R. Vautard and P. Yiou. Control of recent european surface climate change by atmospheric flow. *Geophysical Research Letters*, 36, 2009. doi:[10.1029/2009GL040480](https://doi.org/10.1029/2009GL040480).
- [87] R. Vautard, P. Yiou, F. Otto, P. Stott, N. Christidis, G. J. van Oldenborgh, and N. Schaller. Attribution of human-induced dynamical and thermodynamical contributions in extreme weather events. *Environmental Research Letters*, 11(11):114009, 2016. doi:[10.1088/1748-9326/11/11/114009](https://doi.org/10.1088/1748-9326/11/11/114009).

- [88] V. Wirth, M. Riemer, E. K. M. Chang, and O. Martius. Rossby wave packets on the midlatitude waveguide - a review. Monthly Weather Review, 146(7):1965–2001, 2018. doi:<https://doi.org/10.1175/MWR-D-16-0483.1>.
- [89] P. Yiou, A. Jézéquel, P. Naveau, F. E. L. Otto, R. Vautard, and M. Vrac. A statistical framework for conditional extreme event attribution. Advances in Statistical Climatology, Meteorology and Oceanography, 3(1):17–31, 2017. doi:10.5194/ascmo-3-17-2017.
- [90] P. Yiou, R. Vautard, P. Naveau, and C. Cassou. Inconsistency between atmospheric dynamics and temperatures during the exceptional 2006/2007 fall/winter and recent warming in europe. Geophysical Research Letters, 34(21), 2007. doi:<https://doi.org/10.1029/2007GL031981>.
- [91] Y. Zhu and R. E. Newell. A Proposed Algorithm for Moisture Fluxes from Atmospheric Rivers. Monthly Weather Review, 126(3):725–735, 1998. doi:10.1175/1520-0493(1998)126<0725:APAFMF>2.0.CO;2.
- [92] J. Zscheischler, S. Westra, B. Hurk, S. Seneviratne, P. Ward, A. Pitman, A. AghaKouchak, D. Bresch, M. Leonard, T. Wahl, and X. Zhang. Future climate risk from compound events. Nature Climate Change, 8, 2018. doi:10.1038/s41558-018-0156-3.